

44-77- TIX
197836
118

**ACOUSTIC RADIATION DAMPING
OF FLAT RECTANGULAR PLATES
SUBJECTED TO SUBSONIC FLOWS**

by

Karen Heitman Lyle

**Department of Mechanical Engineering
Duke University**

Date: November 1, 1993

Approved:

Earl H. Dowell
Earl H. Dowell, Supervisor

Wmald B. Bliss
James D. Light
Loen W. Flock

**Dissertation submitted in partial fulfillment of
the requirements for the degree of Doctor
of Philosophy in the Department of
Mechanical Engineering in the Graduate School
of Duke University
1993**

(NASA-TM-109382) ACOUSTIC
RADIATION DAMPING OF FLAT
RECTANGULAR PLATES SUBJECTED TO
SUBSONIC FLOWS (Duke Univ.) 118 p

N94-20211

Unclas

G3/71 0197836

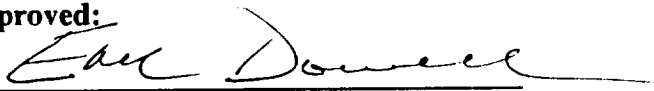
ABSTRACT
(Mechanical Engineering)
ACOUSTIC RADIATION DAMPING
OF FLAT RECTANGULAR PLATES
SUBJECTED TO SUBSONIC FLOWS

by

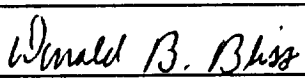
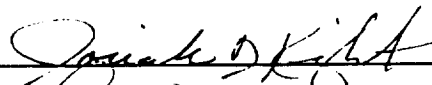

Karen Heitman Lyle
Department of Mechanical Engineering
Duke University

Date: November 1, 1993

Approved:



Earl H. Dowell, Supervisor

An abstract of a dissertation submitted in partial
fulfillment of the requirements for the degree
of Doctor of Philosophy in the Department of
Mechanical Engineering in the Graduate School of
Duke University

1993

ABSTRACT

The acoustic radiation damping for various isotropic and laminated composite plates and semi-infinite strips subjected to a uniform, subsonic and steady flow has been predicted. The predictions are based on the linear vibration of a flat plate. The fluid loading is characterized as the perturbation pressure derived from the linearized Bernoulli and continuity equations. Parameters varied in the analysis include Mach number, mode number and plate size, aspect ratio and mass. The predictions are compared with existing theoretical results and experimental data. The analytical results show that the fluid loading can significantly affect realistic plate responses. Generally, graphite/epoxy and carbon/carbon plates have higher acoustic radiation damping values than similar aluminum plates, except near plate divergence conditions resulting from aeroelastic instability. Universal curves are presented where the acoustic radiation damping normalized by the mass ratio is a linear function of the reduced frequency. A separate curve is required for each Mach number and plate aspect ratio. In addition, acoustic radiation damping values can be greater than or equal to the structural component of the modal critical damping ratio (assumed as 0.01) for the higher subsonic Mach numbers. New experimental data were acquired for comparison with the analytical results.

ACKNOWLEDGMENTS

The author would like to express her gratitude to her advisor, Dr. Earl H. Dowell, for his guidance throughout the research work. In addition, she would like to thank Dr. Donald Bliss, Dr. Josiah Knight, Dr. Loren Nolte, and Dr. Senol Utku, who served on the advisory committee.

The author would also like to thank Dr. Clemans A. Powell, Dr. Kevin P. Shepherd, Dr. Feldon D. Barlett and Mr. Danny R. Hoad for their support of the graduate study leave and the research project.

Finally, the author would like to thank her husband, Jerry, and her parents for their constant encouragement.

TABLE OF CONTENTS

ABSTRACT	iii
ACKNOWLEDGMENTS	iv
LIST OF FIGURES	viii
LIST OF TABLES	xii
NOMENCLATURE	xiii
CHAPTER 1 INTRODUCTION	1
CHAPTER 2 THEORY	3
2.1 General Derivation	3
2.1.1 Finite Plate	3
2.1.2 Semi-infinite Strip	9
2.2 Mode Function Representation	11
2.2.1 Finite Plate	11
2.2.2 Semi-infinite Strip	11
2.3 Frequency Response Solution Techniques	12
2.3.1 Half Power Method	12
2.3.2 Complex Frequency	12

2.4	Perturbation Approximation for Small Mass Ratio	13
2.5	Solutions for Special Cases	14
2.5.1	Incompressible Flow	14
2.5.2	No Flow	14
2.5.3	Piston Theory	15
CHAPTER 3	THEORETICAL RESULTS	18
3.1	Numerical Integral Evaluations	18
3.2	Damping Calculations	20
3.2.1	Semi-infinite Strip	21
3.2.2	Finite Plate	23
CHAPTER 4	EXPERIMENT	51
4.1	Description of Test Setup	51
4.2	A priori estimation of test conditions	53
4.2.1	Boundary Layer Thickness	54
4.2.2	PZT excitation	54
4.2.3	Flow induced vibrations	56
4.3	Ground vibration tests	57
4.3.1	Test Plate 1	57
4.3.2	Test Plate 2	58
4.4	Flow Tests	61

CHAPTER 5	CONCLUDING REMARKS	86
BIBLIOGRAPHY	90
APPENDIX A	BEAM FUNCTION APPROXIMATION	94
APPENDIX B	EXPERIMENTAL DECAY PLOTS	96
APPENDIX C	BIOGRAPHY	103

LIST OF FIGURES

Figure 2.1	Analytical models	17
Figure 3.1	Effect of reduced frequency and mode number on C_1	31
Figure 3.2	Effect of reduced frequency and mode number on $k^2 C_2$. . .	32
Figure 3.3	Effect of Mach number on first mode C_1	33
Figure 3.4	Effect of aspect ratio number on first mode C_1	34
Figure 3.5	Comparison of total and 2-point prediction methods at M=0.8 for (a) mode 1 and (b) mode 10 with Mode 10 variation of (c) C_1 and (d) C_2	35
Figure 3.6	Effect of mass ratio and mode number on (a) frequency ratio and (b) damping ratio	36
Figure 3.7	Effect of Mach number, edge conditions and flow on (a) frequency ratio and (b) damping ratio.	37
Figure 3.8	Effect of Mach number and chord on (a) frequency ratio and (b) damping ratio.	38
Figure 3.9	Effect of Mach number and plate mass on (a) frequency ratio and (b) damping ratio.	39
Figure 3.10	Effect of Mach number and plate thickness on (a) frequency ratio and (b) damping ratio.	40
Figure 3.11	Effect of Mach number and mode number on (a) frequency ratio and (b) damping ratio.	41
Figure 3.12	Comparison of Wilby and Lyle acoustic radiation damping ratios.	42

Figure 3.13	Comparison of Chyu and Lyle acoustic radiation damping ratios.	43
Figure 3.14	Effect of aspect ratio on acoustic radiation damping.	44
Figure 3.15	Effect of Mach number on (a) frequency ratio and (b) damping ratio for graphite/epoxy plates with outside fiber aligned with flow, 0°.	45
Figure 3.16	Effect of Mach number on (a) frequency ratio and (b) damping ratio for graphite/epoxy plates with outside fiber perpendicular to flow, 90°.	46
Figure 3.17	Effect of Mach number on (a) frequency ratio and (b) damping ratio for carbon/carbon plates with outside fiber aligned with flow, 0°.	47
Figure 3.18	Effect of Mach number on (a) frequency ratio and (b) damping ratio for carbon/carbon plates with outside fiber perpendicular to flow, 90°.	48
Figure 3.19	Damping ratio normalized by mass ratio as a function of $k_1 = \sqrt{\frac{\Omega_{m, in-vacuum}}{1 - \mu C_2^{mm}(k_{res}, M, l)}} \sqrt{\frac{D_{11}}{\rho h a^2 c_0^2}}$ for a/b=0.66667.	49
Figure 3.20	Damping ratio normalized by mass ratio as a function of $k_2 = \sqrt{\frac{D_{11}}{\rho h a^2 c_0^2}}$ for a/b=0.66667.	50
Figure 4.1	(a) Photograph and (b) schematic of Quiet Flow Facility.	68
Figure 4.2	Variation of total pressure ratio at (a) 0.508m and (b) 0.762m from nozzle.	69
Figure 4.3	Photograph of model in-situ.	70

Figure 4.4	Sketch of model.	71
Figure 4.5	Drawing of test plate in fore and aft airfoils.	72
Figure 4.6	Detailed drawing of clamping mechanism: (a) fore airfoil; and (b) aft airfoil.	73
Figure 4.7	Photograph of plate in-situ.	74
Figure 4.8	Transducer locations.	75
Figure 4.9	Sample transfer function for Plate 1 calculated from accelerometer response due an impact hammer excitation. .	76
Figure 4.10	Scatter of (a) modal frequencies and (b) damping ratios for Test Plates 1 and 2 without PZTs or strain gages installed.	77
Figure 4.11	Scatter of Plate 2 no-flow damping ratios with PZTs and strain gages installed.	78
Figure 4.12	Variation of fore and aft airfoil pressure differential as a function of Mach number.	79
Figure 4.13	Power spectral density of strain gage at $M=0.6$ with and without the accelerometer installed.	80
Figure 4.14	Repeatability of the accelerometer power spectral density at $M=0.6$	81
Figure 4.15	First mode power spectral density for (a) strain gage and (b) accelerometer.	82
Figure 4.16	Variation of mode 1 (a) frequency ratio and (b) damping ratio as a function of Mach number for various analytical and experimental cases.	83

Figure 4.17	First mode damping ratio relative to the damping at Mach 0.	84
Figure 4.18	Variation of mode 2 (a) frequency ratio and (b) damping ratio as a function of Mach number for various analytical and experimental cases.	85
Figure A1	Comparison of exact (—) and approximate (\square) mode shapes	95
Figure B1	Accelerometer response for PZT excitation at the 1,1 mode.	96
Figure B2	Accelerometer response for acoustic speaker excitation at the 1,2 mode.	97
Figure B3	Accelerometer response for PZT excitation at the 1,2 mode.	98
Figure B4	Accelerometer response for acoustic speaker excitation at the 1,3 mode.	99
Figure B5	Strain gage response for PZT excitation at the 1,3 mode.	100
Figure B6	Strain gage response for PZT excitation at the 1,3 mode.	101
Figure B7	Accelerometer response for PZT excitation at the 1,3 mode.	102

LIST OF TABLES

Table 3.1	Material Properties	29
Table 3.2	Plate Mode(m) to Beam Function Pair (r,s) Correspondence	30
Table 4.1	Plate modal frequencies	66
Table 4.2	No-flow measured damping values	67

NOMENCLATURE

<i>Symbol</i>	<i>Description</i>
a	chord length
A_m	m^{th} modal coefficient
b	span length
B^m	m^{th} eigenvector
c_0	speed of sound
C_1	aerodynamic damping integral
C_2	aerodynamic mass or stiffness integral
$D, D_{11}, D_{12}, D_{22}, D_{16}, D_{26}, D_{66}$	plate bending stiffnesses
E_{11}, E_{22}	Young's modulus
\bar{f}	total force/area on plate
f, F, \hat{F}	mechanical force/area on plate
G	Shear modulus
G_R, G_I	real and imaginary parts of mode shape function
h	plate thickness
j	$\sqrt{-1}$
k	reduced frequency, $\omega a/c_0$
l	chord/span ratio, a/b
m, n	mode numbers
M	mach number
p, P	plate pressure loading
S	plate area, ab
t	time
U	fluid velocity
w, W	plate displacement
W_m, W_n	free vibration mode shapes
x, y, z	coordinate locations
x_0, y_0	normalized coordinate location

α, α_0	x fourier transform variable
β_r	r^{th} beam function coefficient
γ, γ_0	y fourier transform variable
δ	dirac delta function
ζ^m	m^{th} modal viscous critical damping ratio
$\eta, \hat{\eta}$	velocity potential coefficient
μ	mass ratio
ν_{12}	Poisson's ratio
ρ	plate density
ρ_0	fluid density
ϕ, Φ	velocity potential
ψ_m	m^{th} beam function expression
ω, Ω	forcing frequency
ω_m, Ω_m	free vibration frequency

CHAPTER 1 INTRODUCTION

Structural vibration response to broadband random excitation, whether linear or nonlinear, is largest in magnitude near the system natural frequencies. The maximum magnitude is approximately inversely proportional to the system damping. Thus, accurate maximum response predictions require equally accurate damping values. Frequently, these values are derived from empirical methods and 'experience'. Modifications made a posteriori then force agreement between measurements and predictions. For aircraft, the system damping may be separated into two components: structural - primarily resulting from the structural joint motion; and acoustic radiation (also known as aerodynamic) - resulting from the fluid/structure interaction.

Extensive acoustic radiation (or aerodynamic) damping research exists for isotropic panels vibrating in supersonic flow [8, 9, 20, 26] and no flow conditions [14, 16, 19, 22, 24, 28]. Supersonic aerodynamic damping frequently dominates the structural damping. A simplified analysis called piston theory can approximate the high supersonic aerodynamic damping or the very high frequency damping at any Mach number. Very thin panels or membranes and heavy fluid loading account for most of the no flow work. Strawderman [25] studied the effects of fluid loading on plates for turbulent subsonic flows where the free stream velocity is much less than the speed of sound. Abrahams [1] studied the fluid/structure interaction problem in subsonic flow to calculate the onset of flutter or divergence instability. Additional work has been done related to cylindrical structures [15, 23]. For a recent view of the subject see ref. [7].

This dissertation emphasizes the systematic evaluation of the subsonic acoustic radiation damping component to determine its importance relative to the structural component. The next chapter describes the acoustic radiation damping analyses of thin semi-infinite strips and finite plates subjected to a uniform subsonic flow. Varying parameters, such as Mach number or mass, produce the same trends for either the semi-infinite strip or the finite plate. To decrease significantly the computation time, these parameter effects have been evaluated using the semi-infinite strip. The finite plate analysis has been utilized to show the effect of aspect ratio and composite ply lay-up. Numerical damping results, including comparisons with previously published data, follow the theory. Experimental modal frequencies and damping values are then compared to the analytical damping values. Concluding remarks about the research follow these comparisons.

CHAPTER 2 THEORY

2.1 General Derivation

Results for finite plates as well as semi-infinite strips are presented in the dissertation. A full derivation has been given for the finite plate. Only semi-infinite strip expressions that differ from the finite plate expressions are listed. The semi-infinite strip equation numbers will end with an *s*. For example, Eq. (2.1s) is the semi-infinite strip expression corresponding to the finite plate expression given in Eq. (2.1).

2.1.1 Finite Plate

A simple, flat, plate is placed flush in a rigid, infinite baffle, with a subsonic uniform steady flow over the plate, see Figure 2.1(a). Unless otherwise stated, only the fluid effect on the upper surface is modelled in the analysis. Thus the cavity under the plate or strip is ignored. The static pressure in the cavity is assumed to be the same as that on the upper surface so that no static deformation of the plate exists. The analytical model for the statically deformed plate or strip case requires a nonlinear analysis, which is not pursued here. Realistically, air in the cavity has little effect on the frequency ratio. However, the damping is under predicted by the amount for the air on the lower surface corresponding approximately to a flow at $M=0$.

The differential equation for a thin, symmetrically laminated, composite plate in linear vibration is [13]:

$$\begin{aligned} D_{11} \frac{\partial^4 w}{\partial x^4} + 2(D_{12} + 2D_{66}) \frac{\partial^4 w}{\partial x^2 \partial y^2} + D_{22} \frac{\partial^4 w}{\partial y^4} \\ + 4D_{16} \frac{\partial^4 w}{\partial x^3 \partial y} + 4D_{26} \frac{\partial^4 w}{\partial x \partial y^3} + \rho h \frac{\partial^2 w}{\partial t^2} = \bar{f}. \end{aligned} \quad (2.1)$$

The force, \bar{f} , is divided into two components: the fluid pressure at $z = 0$, $p|_{z=0}$; and the mechanical force per unit area, f .

The perturbation pressure model, derived from the linearized Bernoulli and continuity equations for isentropic, inviscid, nonconducting, irrotational flow with no body forces, is related to the velocity potential by [3, 8, 9]:

$$p = -\rho_0 \left(\frac{\partial}{\partial t} + U_0 \frac{\partial}{\partial x} \right) \phi, \quad (2.2)$$

where the differential equation for the velocity potential field is:

$$\nabla^2 \phi - \frac{1}{c_0^2} \left(\frac{\partial}{\partial t} + U_0 \frac{\partial}{\partial x} \right)^2 \phi = 0. \quad (2.3)$$

The boundary condition on ϕ is:

$$\left. \frac{\partial \phi}{\partial z} \right|_{z=0} = \left(\frac{\partial}{\partial t} + U_0 \frac{\partial}{\partial x} \right) w. \quad (2.4)$$

In addition, ϕ must be finite for $z \rightarrow \infty$ and waves induced by the plate motion must radiate from the plate.

Assuming sinusoidal motion, i.e., $w(x, y, t) = W(x, y)e^{j\omega t}$, $p(x, y, z, t) = P(x, y, z)e^{j\omega t}$, $\phi(x, y, z, t) = \Phi(x, y, z)e^{j\omega t}$, $f(x, y, t) = F(x, y)e^{j\omega t}$ then Eqs. (2.1–2.4) become

$$\begin{aligned} D_{11} \frac{\partial^4 W}{\partial x^4} + 2(D_{12} + 2D_{66}) \frac{\partial^4 W}{\partial x^2 \partial y^2} + D_{22} \frac{\partial^4 W}{\partial y^4} \\ + 4D_{16} \frac{\partial^4 W}{\partial x^3 \partial y} + 4D_{26} \frac{\partial^4 W}{\partial x \partial y^3} - \rho h \omega^2 W + P|_{z=0} = F, \end{aligned} \quad (2.1a)$$

$$P = -\rho_0 \left(j\omega + U_0 \frac{\partial}{\partial x} \right) \Phi, \quad (2.2a)$$

$$\nabla^2 \Phi - \frac{1}{c_0^2} \left(j\omega + \frac{\partial}{\partial x} \right)^2 \Phi = 0, \quad (2.3a)$$

and

$$\frac{\partial \Phi}{\partial z} \Big|_{z=0} = \left(j\omega + U_0 \frac{\partial}{\partial x} \right) W. \quad (2.4a)$$

Solving for the velocity potential by first taking the Fourier Transform of Eq. (2.3a), where the Fourier Transform pair for 2-dimensions is given by [11, 8]:

$$\Phi^*(\alpha, \gamma, z) = \int_{-\infty}^{\infty} \int_{-\infty}^{\infty} \Phi(x, y, z) e^{-j(\alpha x + \gamma y)} dx dy \quad (2.5a)$$

and

$$\Phi(x, y, z) = \frac{1}{4\pi^2} \int_{-\infty}^{\infty} \int_{-\infty}^{\infty} \Phi^*(\alpha, \gamma, z) e^{j(\alpha x + \gamma y)} d\alpha d\gamma, \quad (2.5b)$$

then Eq. (2.3a) becomes:

$$\left[(j\alpha)^2 \left(1 - \left(\frac{U_0}{c_0} \right)^2 \right) - 2j\omega U_0 j\alpha / c_0^2 + (j\gamma)^2 \right] \Phi^* + \frac{d^2 \Phi^*}{dz^2} + \frac{\omega^2}{c_0^2} \Phi^* = 0. \quad (2.6)$$

Rearranging terms:

$$\frac{d^2 \Phi^*}{dz^2} = \left[\alpha^2 (1 - M^2) - 2\omega U_0 \alpha / c_0^2 + \gamma^2 - \frac{\omega^2}{c_0^2} \right] \Phi^*. \quad (2.7)$$

Now for $\eta^2 = \alpha^2 (1 - M^2) - 2\omega U_0 \alpha / c_0^2 + \gamma^2 - \omega^2 / c_0^2$, the solution to Eq. (2.3a) can have two forms depending on the sign of η^2 . If $\eta^2 > 0$,

$$\Phi_1^* = A e^{\eta z} + B e^{-\eta z}, \quad (2.8a)$$

and if $\eta^2 < 0$ then,

$$\Phi_2^* = C e^{j\tilde{\eta} z} + D e^{-j\tilde{\eta} z}, \quad (2.8b)$$

where $\tilde{\eta}^2 = -\eta^2$. Evaluating the coefficients in Eq. (2.8) requires four conditions. In Eq. (2.8a), Φ_1^* must be bounded as $z \rightarrow \infty$, so that $A \equiv 0$. In Eq. (2.8b), the waves must be outgoing. Thus, by including the time dependence, $e^{j\omega t}$, in the velocity potential, then $C \equiv 0$.

Applying the boundary condition at $z=0$, to Eq. (2.8), with the Fourier Transform, Eq. (2.5), to solve for B and D , then the velocity potential for, $\eta^2 > 0$ is:

$$\Phi_1^* = \frac{-j(\omega + U_0\alpha)W^*}{\eta} e^{-\eta z}, \quad (2.9a)$$

and for $\eta^2 < 0$ is:

$$\Phi_2^* = \frac{-j(\omega + U_0\alpha)W^*}{j\tilde{\eta}} e^{-j\tilde{\eta}z}. \quad (2.9b)$$

Eq. (2.9) is substituted for the velocity potential in the Fourier Transform version of Eq. (2.2a) at $z=0$, to yield:

$$P_1^*|_{z=0} = \frac{-\rho_0(\omega + U_0\alpha)^2 W^*}{\eta} \quad (2.10a)$$

and

$$P_2^*|_{z=0} = \frac{-\rho_0(\omega + U_0\alpha)^2 W^*}{j\tilde{\eta}}. \quad (2.10b)$$

The single difference in form between the above two expressions is that η in Eq. (2.10a) has been replaced by $j\tilde{\eta}$ in Eq. (2.10b). The remaining equations are written using η with the understanding when $\eta^2 < 0$, then η should be replaced with $j\tilde{\eta}$.

Solving for the pressure on the plate using the inverse Fourier Transform, then Eq. (2.10a) becomes:

$$P|_{z=0} = \frac{-\rho_0}{4\pi^2} \int_{-\infty}^{\infty} \int_{-\infty}^{\infty} \frac{(\omega + U_0\alpha)^2 W^* e^{-j(\alpha x + \gamma y)}}{\eta} dx dy. \quad (2.11)$$

Now expressing the plate deflection by an in-vacuo modal expansion:

$$W = \sum_{n=1}^N A_n W_n \quad (2.12)$$

where,

$$\left[D_{11} \frac{\partial^4}{\partial x^4} + 2(D_{12} + 2D_{66}) \frac{\partial^4}{\partial x^2 \partial y^2} + D_{22} \frac{\partial^4}{\partial y^4} + 4D_{16} \frac{\partial^4}{\partial x^3 \partial y} + 4D_{26} \frac{\partial^4}{\partial x \partial y^3} - \rho h \omega^2 \right] W_n = \rho h \omega_n^2 W_n. \quad (2.13)$$

Then Eq. (2.1) may be rewritten as:

$$\sum_{n=1}^N [\rho h \omega_n^2 - \rho h \omega^2] A_n W_n + P|_{z=0} = F. \quad (2.14)$$

Applying Galerkin's method, i.e. integrating Eq. (2.14) by

$$\int_S W_m (\dots\dots) dS \quad (2.15)$$

and utilizing the orthogonality of W_m and W_n , then

$$\rho h (\omega_n^2 - \omega^2) A_m + \frac{\int_S P|_{z=0} W_m dS}{\int_S W_m W_m dS} = \frac{\int_S F W_m dS}{\int_S W_m W_m dS}, \quad (2.16)$$

where, S is the plate area, ab . A uniform plate mass is assumed here; however, a non-uniform mass distribution could be handled with little additional difficulty.

Interchanging the order of integrations and summation simplifies the evaluation of the second term numerator, so that:

$$\int_S P|_{z=0} W_m dS = \sum_{n=1}^N A_n \left\{ \frac{-\rho_0}{4\pi^2} \int_{-\infty}^{\infty} \int_{-\infty}^{\infty} \frac{(\omega + U_0 \alpha)^2}{\eta} \left[\int_0^a \int_0^b W_n e^{-j(\alpha x + \gamma y)} dx dy \right] \left[\int_0^a \int_0^b W_m e^{j(\alpha x + \gamma y)} dx dy \right] d\alpha d\gamma \right\}. \quad (2.17)$$

If W_n is expressed as the summation of classical modes (such as products of beam functions) then the integrations over the plate area have a closed-form solution. By interchanging the integrations and summation only one numerical integration is required.

Eq. (2.16) expressed in nondimensional parameters is:

$$\left[\Omega_m^2 - \Omega^2\right]\{A\} + \mu\Omega^2 \left[jC_1^{mn}(k, M, l) + C_2^{mn}(k, M, l)\right]\{A\} = \hat{F}. \quad (2.18)$$

The acoustic-radiation damping is represented by $\mu\Omega^2 C_1$ and the effective mass or stiffness by $\mu\Omega^2 C_2$.

Substitution of Eq. (2.17) into Eq. (2.16) and comparing to Eq. (2.18) gives

$$\begin{aligned} jC_1^{mn}(k, M, l) + C_2^{mn}(k, M, l) &= \frac{1}{4\pi^2} \int_{-\infty}^{\infty} \int_{-\infty}^{\infty} \left(1 + \frac{M\alpha_0}{k}\right)^2 \\ &\times \frac{[G_R^{mn}(\alpha_0, \gamma_0) + jG_I^{mn}(\alpha_0, \gamma_0)]d\alpha_0 d\gamma_0}{\sqrt{\alpha_0^2(1 - M^2) + l^2\gamma_0^2 - 2kM\alpha_0 - k^2}}, \end{aligned} \quad (2.19)$$

where $\alpha_0 = \alpha a$ and $\gamma_0 = \gamma b$. Solving for C_1 and C_2 independently, then the damping term is:

$$\begin{aligned} C_1^{mn}(k, M, l) &= \frac{1}{4\pi^2} \left[\int \int_{A_1} \frac{\left(1 + \frac{M\alpha_0}{k}\right)^2 G_R^{mn}(\alpha_0, \gamma_0) d\alpha_0 d\gamma_0}{\sqrt{-\alpha_0^2(1 - M^2) - l^2\gamma_0^2 + 2kM\alpha_0 + k^2}} \right. \\ &\quad \left. - \int \int_{A_2} \frac{\left(1 + \frac{M\alpha_0}{k}\right)^2 G_I^{mn}(\alpha_0, \gamma_0) d\alpha_0 d\gamma_0}{\sqrt{\alpha_0^2(1 - M^2) + l^2\gamma_0^2 - 2kM\alpha_0 - k^2}} \right], \end{aligned} \quad (2.20)$$

and the effective mass or stiffness is:

$$\begin{aligned} C_2^{mn}(k, M, l) &= \frac{1}{4\pi^2} \left[\int \int_{A_1} \frac{-\left(1 + \frac{M\alpha_0}{k}\right)^2 G_I^{mn}(\alpha_0, \gamma_0) d\alpha_0 d\gamma_0}{\sqrt{-\alpha_0^2(1 - M^2) - l^2\gamma_0^2 + 2kM\alpha_0 + k^2}} \right. \\ &\quad \left. - \int \int_{A_2} \frac{\left(1 + \frac{M\alpha_0}{k}\right)^2 G_R^{mn}(\alpha_0, \gamma_0) d\alpha_0 d\gamma_0}{\sqrt{\alpha_0^2(1 - M^2) + l^2\gamma_0^2 - 2kM\alpha_0 - k^2}} \right], \end{aligned} \quad (2.21)$$

where:

$$G_R^{mn} + jG_I^{mn} = \left[\int_0^1 \int_0^1 W_n e^{-j(\alpha_0 x_0 + \gamma_0 y_0)} dx_0 dy_0 \right] \left[\int_0^1 \int_0^1 W_m e^{j(\alpha_0 x_0 + \gamma_0 y_0)} dx_0 dy_0 \right],$$

A_1 is the area inside the ellipse $\alpha_0^2(1 - M^2) + l^2\gamma_0^2 - 2kM\alpha_0 - k^2 = 0$, and A_2 is the area outside the ellipse.

2.1.2 Semi-infinite Strip

The semi-infinite strip is shown in Figure 2.1(b) for flow on one side. The differential equation for a semi-infinite strip vibrating in an infinite baffle is:

$$D \frac{\partial^4 w}{\partial x^4} + \rho h \frac{\partial^2 w}{\partial t^2} = \bar{f}. \quad (2.1s)$$

Utilizing the linearized Bernoulli and continuity expressions, Eqs. (2.2a, 2.3a); the boundary conditions given by Eq. (2.4a); and assuming sinusoidal motion, then:

$$P|_{z=0} = \frac{-\rho_0}{2\pi} \int_{-\infty}^{\infty} \frac{(\omega + U_0\alpha)^2 W^* e^{-j\alpha x}}{\eta} d\alpha, \quad (2.11s)$$

where: $\eta^2 = \alpha^2(1 - M_0^2) - \frac{2\omega U_0\alpha}{c_0^2} - \frac{\omega^2}{c_0^2}$.

Again, expressing the strip deflection by an in-vacuo modal expansion and utilizing the orthogonality of W_m and W_n , then the result is given by Eq. (2.16), where S is the strip length, a . Interchanging the order of integration and summation, then the second term numerator is given by:

$$\int_S P|_{z=0} W_m dS = \sum_{n=1}^N A_n \left\{ \frac{-\rho_0}{2\pi} \int_{-\infty}^{\infty} \frac{(\omega + U_0\alpha)^2}{\eta} \left[\int_0^a W_n e^{-j\alpha x} dx \right] \left[\int_0^a W_m e^{j\alpha x} dx \right] d\alpha \right\}. \quad (2.17s)$$

The resulting nondimensional form of Eq. (2.16) is:

$$[\Omega_m^2 - \Omega^2] \{A\} + \mu\Omega^2 [jC_1^{mn}(k, M) + C_2^{mn}(k, M)] \{A\} = \hat{F}. \quad (2.18s)$$

Substitution of Eq. (2.17s) into Eq. (2.16) and comparing to (2.18s) gives:

$$jC_1^{mn} + C_2^{mn} = \frac{1}{2\pi} \int_{-\infty}^{\infty} \left\{ \frac{\left(1 + \frac{M_0\alpha_0}{k}\right)^2 (G_R^{mn}(\alpha_0) + jG_I^{mn}(\alpha_0))}{\sqrt{\alpha_0^2(1 - M_0^2) - 2kM_0\alpha_0 - k^2}} \right\} d\alpha_0. \quad (2.19s)$$

Solving for C_1 and C_2 independently, then:

$$C_1^{mn}(k, M_0) = \frac{1}{2\pi} \int_{A_1} \frac{\left(1 + \frac{M_0\alpha_0}{k}\right)^2 G_R^{mn}(\alpha_0) d\alpha_0}{\sqrt{-\alpha_0^2(1 - M_0^2) - 2kM_0\alpha_0 + k^2}} - \frac{1}{2\pi} \int_{A_2} \frac{\left(1 + \frac{M_0\alpha_0}{k}\right)^2 G_I^{mn}(\alpha_0) d\alpha_0}{\sqrt{\alpha_0^2(1 - M_0^2) + 2kM_0\alpha_0 - k^2}}, \quad (2.20s)$$

$$C_2^{mn}(k, M_0) = \frac{1}{2\pi} \int_{A_1} \frac{-\left(1 + \frac{M_0\alpha_0}{k}\right)^2 G_I^{mn}(\alpha_0) d\alpha_0}{\sqrt{-\alpha_0^2(1 - M_0^2) - 2kM_0\alpha_0 + k^2}} - \frac{1}{2\pi} \int_{A_2} \frac{\left(1 + \frac{M_0\alpha_0}{k}\right)^2 G_R^{mn}(\alpha_0) d\alpha_0}{\sqrt{\alpha_0^2(1 - M_0^2) + 2kM_0\alpha_0 - k^2}}, \quad (2.21s)$$

where:

$$G_R^{mn} + jG_I^{mn} = \left[\int_0^1 W_n e^{-j\alpha_0 x_0} dx_0 \right] \left[\int_0^1 W_m e^{j\alpha_0 x_0} dx_0 \right],$$

A_1 is the region where $\alpha_0^2(1 - M_0^2) - 2kM_0\alpha_0 - k^2 < 0$, and A_2 is where $\alpha_0^2(1 - M_0^2) - 2kM_0\alpha_0 - k^2 > 0$. For symmetric fluid loading on both sides, see Figure 2.1(c), the integrals in Eqs. (2.20s) and (2.21s) would be doubled.

2.2 Mode Function Representation

2.2.1 Finite Plate

The normalized mode shapes ($x_0 = x/a$ and $y_0 = y/b$) for clamped isotropic plates are represented as follows:

$$W_m = \sum_{r=1}^R \sum_{s=1}^S B_{rs}^m \psi_r(x_0) \psi_s(y_0),$$

$$W_n = \sum_{p=1}^P \sum_{q=1}^Q B_{pq}^n \psi_p(x_0) \psi_q(y_0) \quad (2.22)$$

where the normalized clamped beam functions, ψ , may be approximated by (see Appendix A):

$$\psi_r(z) = \sin \beta_r z - \cos \beta_r z - (-1)^r e^{\beta_r(z-1)} + e^{-\beta_r z} \quad (2.23)$$

and B_{rs}^m and B_{pq}^n are eigenvectors of the beam modes, rs and pq , associated with the m^{th} and n^{th} plate modes, respectively. The approximation, Eq. (2.23), eliminates the calculation of hyperbolic functions which can lead to inaccuracies, particularly for higher modes.

2.2.2 Semi-infinite Strip

The normalized mode shapes for the semi-infinite strip are given by:

$$W_m = \psi_m(x_0), \quad W_n = \psi_n(x_0), \quad (2.22s)$$

The clamped mode shapes are given by Eq. (2.23), while the pinned mode shapes are $\psi_r(z) = \sin(r\pi z)$.

2.3 Frequency Response Solution Techniques

2.3.1 Half Power Method

The ‘half-power bandwidth’ method is the approach frequently chosen in estimating small critical damping ratios. The amplitude over force ratio is plotted versus frequency, where the mechanical force is non zero. Ω_a and Ω_b are the frequencies at which this ratio is $\frac{1}{\sqrt{2}}$ of the maximum value found at the resonance frequency, Ω_R . The relationship between these frequencies and the critical damping ratio is [21]

$$\zeta^m \equiv \frac{\Omega_I^m}{\Omega_R^m} \approx \frac{\Omega_b - \Omega_a}{2\Omega_R^m} \quad (2.24)$$

assuming that $\Omega_I^m \ll \Omega_R^m$. Ω_R^m and Ω_I^m are the real and imaginary parts, respectively, of the resonant frequency.

2.3.2 Complex Frequency

The above method is an approximation to solving directly for the complex frequency. In general the modal frequencies are calculated by setting the determinant of Eq. (2.18) or (2.18s) to zero for $\hat{F} \equiv 0$. The determinant in this case is complex so that the real and imaginary parts must both be zero. Let, $\Omega^m = \Omega_R^m + j\Omega_I^m$ be one of the complex modal frequencies at which the determinant is zero. Then the critical damping ratio is defined as:

$$\zeta^m \equiv \frac{\Omega_I^m}{\Omega_R^m}. \quad (2.25)$$

Although this is the most direct method, it is also computationally time-consuming. For each test panel the complex determinant, composed of complex C_1 and C_2 integrals, must be evaluated many times.

2.4 Perturbation Approximation for Small Mass Ratio

Initially, the damping values may be calculated relatively conveniently using a perturbation technique. Not only will these results give preliminary damping values, but they also provide starting values for solution by frequency response methods.

The frequency will be perturbed about $\mu = 0$ and only include up to first order terms. For air loading μ is usually small. The m^{th} modal frequency may be expressed as:

$$\Omega_R^m + j\Omega_I^m = \overline{\Omega_0^m} + \mu\overline{\Omega_1^m}. \quad (2.26)$$

Substitute Eq. (2.26) into Eq. (2.18) or (2.18s) and set the determinant of the equation to zero, for $\hat{F} \equiv 0$. This is done for each order of μ . The zero order terms are:

$$\overline{\Omega_0^m} = \Omega_m, \quad (2.27)$$

or the zeroth order terms are simply the nondimensional undamped in-vacuo modal frequencies, Ω_m . Solving for the first order terms then gives:

$$\overline{\Omega_1^m} = \frac{\Omega_m}{2} [jC_1^{mm}(k_m, M, l) + C_2^{mm}(k_m, M, l)]. \quad (2.28)$$

Substituting Eqs. (2.27) and (2.28) into (2.26) and maintaining the first order approximation yields the critical damping ratio:

$$\zeta^m = \frac{\Omega_I^m}{\Omega_R^m} = \frac{\mu C_1^{mm}(k_m, M, l)}{2}. \quad (2.29)$$

This result is valid for the semi-infinite strip and the finite plate. In addition, the multimode analysis for the first order perturbation is only dependent on a single in-vacuo mode.

2.5 Solutions for Special Cases

First, three limiting cases of the flow analysis are considered. They provide physical insight and check the more complicated numerical calculations.

2.5.1 Incompressible Flow

For the incompressible flow case, where $c_0 \rightarrow \infty$, then Eq. (2.3a) reduces to:

$$\nabla^2 \Phi = 0, \quad (2.30)$$

the well-known Laplace's equation. The expressions relating the velocity potential to the perturbation pressure and plate displacement, Eqs. (2.2a) and (2.4a), respectively, remain unchanged. Using Fourier Transforms the pressure on the plate has the same general form as Eq. (2.17). However, $\eta = \sqrt{\alpha^2 + \gamma^2}$ is real since the square root argument is non-negative. In addition, Eq. (2.17) will contain only real terms. Thus $k = 0$ (since $c_0 \rightarrow \infty$) and $C_1 = 0$.

2.5.2 No Flow

For small reduced frequencies ($k \ll 1$) and $M = 0$, it can be shown that for an isotropic, clamped, finite plate:

$$C_1^{mm}(k, M = 0, l) = \frac{k}{2\pi l} \left[p_1^2 p_2^2 + \frac{p_3^2 p_4^2 k^4}{15l^2} + \frac{p_2^2 p_3^2 k^2}{3} + \frac{p_1^2 p_4^2 k^2}{l^2} \right], \quad (2.31)$$

where

$$\begin{aligned} p_1 &= \frac{-\cos \beta_r + 2 - \sin \beta_r - (-1)^r}{\beta_r}, \\ p_2 &= \frac{-\cos \beta_s + 2 - \sin \beta_s - (-1)^s}{\beta_s}, \\ p_3 &= \frac{1 + (-1)^r (-\beta_r + 1)}{\beta_r^2}, \\ p_4 &= \frac{1 + (-1)^s (-\beta_s + 1)}{\beta_s^2}. \end{aligned}$$

This assumes that the plate mode is a simple product of two beam modes, i.e., $W_m(x, y) = \psi_r(x)\psi_s(y)$. Eq. (2.31) is dependent on k and goes to zero as $k \rightarrow 0$ as predicted for the incompressible flow case.

2.5.3 Piston Theory

The third limiting case, commonly referred to as piston theory, is applicable in subsonic flows for $k \gg 1$ and for higher supersonic flows at all reduced frequencies. The pressure on the plate is [9]:

$$P|_{z=0} = \rho_0 c_0 \left(j\omega W + U_0 \frac{\partial W}{\partial x} \right). \quad (2.32)$$

Or physically, the pressure is related to that in a tube where the piston velocity is given in parenthesis and $\rho_0 c_0$ is the acoustic impedance. Substitution of Eq. (2.32) into Eq. (2.14) yields:

$$\sum_{n=1}^N A_n \left[W_n (\rho h \omega_n^2 - \rho h \omega^2 + j\omega \rho_0 c_0) + \rho_0 c_0 U_0 \frac{\partial W_n}{\partial x} \right] = 0. \quad (2.33)$$

for no mechanical forcing function. Integrating Eq. (2.33) using Eq. (2.15) then the frequency equation in nondimensional terms becomes:

$$A_m \left[(\Omega_m^2 - \Omega^2) + j \frac{\mu \Omega^2}{k} \right] + \mu \Omega^2 \sum_n \frac{A_n g_{mn} M}{k^2} = 0. \quad (2.34)$$

Comparison of Eqs. (2.34) and (2.18) gives:

$$C_1^{mn} = \begin{cases} \frac{1}{k} & \text{for } m = n \\ 0 & \text{for } m \neq n \end{cases} \quad (2.35)$$

$$C_2^{mn} = \frac{g_{mn} M}{k^2} \quad (2.36)$$

where:

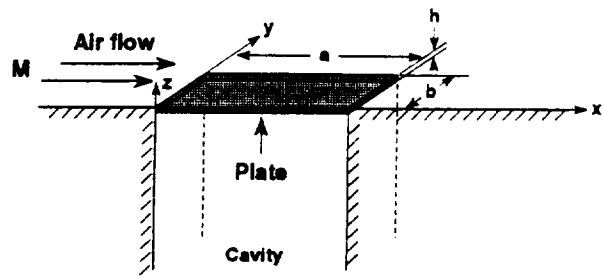
$$g_{mn} = \int_0^1 \int_0^1 \frac{\partial W_n}{\partial x_0} W_m dx_0 dy_0.$$

Eq. (2.35) shows no dependence on aspect ratio, l , or mode number pair, pq , except through their indirect appearance in k . Eqs. (2.35) and (2.36) are valid for any edge condition as long as the mode shapes are orthogonal. Finally, this result also holds for either the semi-infinite strip or the finite plate.

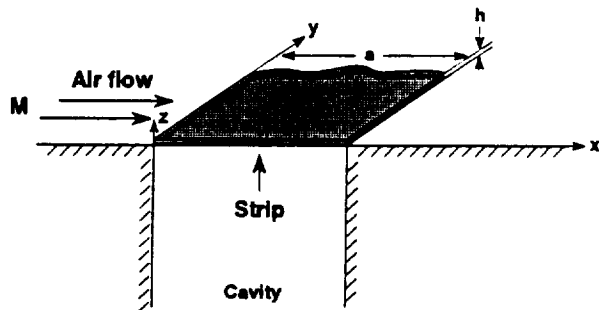
For an isotropic, clamped, finite plate:

$$g_{mn} = \left[\frac{4\beta_r^2 \beta_s^2}{\beta_r^4 - \beta_s^4} \right] [1 - (-1)^{p+r}] \delta(q-s) \quad \text{if} \quad r \neq s \quad (2.37)$$

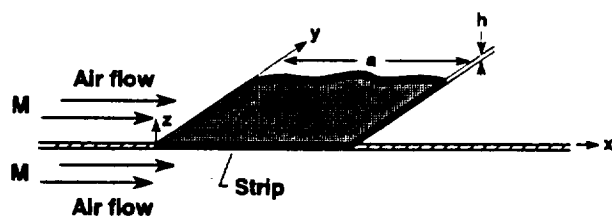
Thus where the plate modes are modelled by pairs of beam functions, i.e, $m=r,s$ and $n=p,q$, then C_2^{mn} is only nonzero when $q = s$, $(p + r)$ is odd and $r \neq s$.



(a) Finite plate



(b) Semi-infinite strip, flow on one-side



(c) Semi-infinite strip, flow on two-sides

Figure 2.1. Analytical models

CHAPTER 3 THEORETICAL RESULTS

The following figures contain results for various aluminum and composite plates. Sample modal frequencies and damping values along with C_1 and C_2 integral evaluations are presented below. An IMSL [12] integration subroutine, based on a Gauss-Konrod quadrature algorithm, evaluated the integrals in Eqs. (2.18) and (2.18s). Table 3.1 contains the material properties used in the computations. Table 3.2 contains the beam function pairs that approximate the plate mode given in the first column. For example, plate mode 3 resembles a plate with the first beam function in the x-direction (flow) and the third beam function in the y-direction (span). Although the plate mode resembles a specific pair of beam functions, the true plate mode deflection is a summation of these beam function pairs, see Eq. (2.22). For the semi-infinite strip, the mode shapes are the beam functions, see Eq. (2.22s).

3.1 Numerical Integral Evaluations

Specific numerical integral evaluations for C_1^{mn} and C_2^{mn} will only be presented for the finite plate. The semi-infinite strip analysis showed similar trends. In addition, the semi-infinite strip analysis agrees with the appropriate limiting case results.

The effective damping term (C_1^{mm}) vs. k values for the first six in-vacuo plate modes (m) of a square plate are presented in Figure 3.1. The in-vacuo modes do not allow for beam modal interaction. Thus for $m=3$, only the beam function pair 1,3 is included in the analysis. These integral values represent an isotropic plate subjected to flow at $M = 0.8$. The plate material properties and speed of sound appear in k . Only diagonal terms for C_1^{mn} and C_2^{mn} (i.e. $m=n$) are presented since they are

dominant. Note that for a particular plate, mode 10 ($k = 3.0$) could have a higher C_1 value and thus greater perturbation damping than mode 1 ($k = 0.9$), recall Eq. (2.25).

These numerical integration results are also compared with the limiting cases. First, as $k \rightarrow 0$, then $C_1^{mm} \rightarrow 0$ as expected from the incompressible flow analysis, section 2.5.1. For the no flow special case, discussed in section 2.5.2, let $k = 0.4$ and $l = 1.0$. Then, $C_1^{11}(M = 0) = 0.03155$ using Eq. (2.31) of that section while the numerical integration of the general case gives $C_1^{11}(M = 0) = 0.03067$ using Eq. (2.20). Thus the two results agree to within 3%. In addition, as k becomes large the curves converge to those results predicted by piston theory, $C_1^{mm} = \frac{1}{k}$, Eq. (2.35).

For the effective mass or stiffness terms, selected off-diagonal $k^2 C_2^{mn}$ vs. k values are plotted in Figure 3.2 for comparison with piston theory. These values represent an isotropic square plate subject to $M = 0.8$ flow. As k becomes large $k^2 C_2^{mn}$ values approach the asymptotes predicted by piston theory, Eq. (2.36). Piston theory predicts $k^2 C_2^{16} = -2.67$, while the numerical integration gives -2.76, Eq. (2.21). The magnitude of these asymptotes is dependent on M , unlike C_1 .

Figure 3.3 shows C_1^{11} vs. k for a square plate at various Mach numbers. C_1^{mm} at a specific frequency generally increases with increasing Mach number, as would be expected. In addition, the k value at which the maximum occurs decreases with increasing Mach number. The curves converge as k becomes large as predicted by piston theory.

Figure 3.4 shows C_1^{11} vs. k at $M = 0.8$ at various a/b ratios. As this ratio decreases then the maximum possible C_1 value increases. Unlike the trend with Mach number, as this ratio decreases, the k value at which the maximum occurs is

approximately constant. Note that as k becomes large the curves converge as would again be expected from piston theory. In addition, as $k \rightarrow 0$ then $C_1^{mm} \rightarrow 0$ as predicted by the incompressible flow case, section 2.5.1.

3.2 Damping Calculations

The panel damping values were calculated at various modal frequencies using the half-power technique as described in section 2.3.1. For comparison purposes, the structural critical damping ratio may be assumed to be approximately 0.01 for all modes and all Mach numbers for lightweight structures such as aircraft fuselage sidewalls. Unless otherwise noted the displacement frequency response curves were calculated for a plate driven by a uniform pressure field over the entire plate or strip, see Eqs. (2.18) and (2.18s). The center of the plate was the response location. In addition, the single (one) mode calculations are based on a simple single product of beam functions. The modal frequencies were determined by locating the maximum of the frequency response curve.

Sample response curves are shown in Figure 3.5. The frequency response was calculated by two methods. For the ‘total’ method, C_1 and C_2 were calculated at each Ω value; while C_1 and C_2 were calculated only near the half-power points and allowed to vary linearly between these two frequencies for the ‘2–point’ method. This 2–point approximation greatly reduces the necessary computation. For this example, an aluminum panel was clamped on four edges and subjected to flow at $M=0.8$. Figure 3.5a corresponds to a single mode analysis of mode 1; while Figure 3.5b corresponds to mode 10. For mode 1 the two methods give nearly identical results, where the damping ratio is 0.010. However, for mode 10 the two methods

give different response curves. The resulting ‘2–point’ damping ratio, 0.100, is nearly 1/3 less than that for the ‘total’ calculation of 0.140. The reason for this discrepancy is evident from Figures 3.5c and d, for C_1 and C_2 , respectively, taken from the ‘total’ computation. Neither C_1 nor C_2 is linearly related to Ω in the frequency range of interest. The results in Figures 3.5b-d represent an extreme, but important case: for large damping values the 2–point approximation may not be sufficiently accurate. C_1 and C_2 were also found to vary rapidly with respect to Ω for very small Ω (plates near divergence).

3.2.1 *Semi-infinite Strip*

Results for the semi-infinite strip are presented in Figures 3.6–3.11. In these calculations the total method was used since damping values as large as 0.20 were calculated. The finite plate analysis shows similar trends, but requires much longer computational times.

Figure 3.6 shows the comparison between Eq. (3.18s) and the data presented by Mixson [19] for a pinned, aluminum strip. The agreement is excellent. In this case the results are for $a=0.762\text{m}$, $h=0.003175\text{m}$ with symmetric no flow conditions. The mass ratio is varied by changing the fluid mass, ρ_0 . The fluid loading has a greater effect on the first mode frequency than on higher mode frequencies. In addition, mode 1 has damping values nearly an order of magnitude greater than the remaining modes. Although the frequency ratios and the mode 1 damping values are well approximated by a single mode, the damping for the higher order modes required more terms. For example, the first three odd modes were required to calculate mode 3. Without flow the even and odd modes do not couple.

Figures 3.7–3.11 present frequency and damping ratios for a number of semi-infinite aluminum strips as a function of Mach number. The fluid for these cases is air at standard atmospheric conditions. Note that for some Mach number the frequency may be reduced to zero by a loss of stiffness due to the aerodynamic flow. In such a case, divergence or aeroelastic buckling occurs, see ref. [9]. The baseline case is the first mode where $a=0.2\text{m}$ and $h=0.001\text{m}$ with fluid flow on one side, i.e., the cavity side effect is ignored.

From Figure 3.7, the plate edge conditions have very little effect on the acoustic radiation damping up to divergence. However, the divergence Mach number for the pinned strip is nearly half that of the clamped strip. In addition, fluid loading on both sides decreases the divergence Mach number about 25 percent while approximately doubling the damping ratio. The figure also shows the comparison between the perturbation approximation (dotted lines) and the half-power technique (solid lines). The perturbation approximation is reasonably accurate until the flow causes the modes to strongly couple or the flow significantly decreases the plate stiffness.

Figure 3.8 shows the effect of chord on frequency ratio and damping ratio as a function of Mach number. Increasing the chord significantly increases the fluid loading effect on both frequency ratio and damping ratio. Doubling the chord (from $a=0.2\text{m}$ to $a=0.4\text{m}$) decreases the divergence Mach number more than factor of two, while the damping ratio is approximately doubled, up to the divergence Mach number.

The effect of plate mass on frequency ratio and damping ratio is shown in Figure 3.9. Changing the plate mass has little effect on the frequency ratio, since

the divergence is stiffness related. However, doubling the strip mass decreases the damping ratio by nearly one-half.

Figure 3.10 shows the effect of plate thickness on frequency ratio and damping ratio as a function of Mach number. The plate thickness has a considerable effect on both the frequency ratio and the damping ratio. Halving the plate thickness results in more than a factor of two decrease in divergence Mach number. However, changing the plate thickness has an approximately inversely proportional relationship on the damping.

Finally, from Figure 3.11, the fluid loading has a much greater effect on the first mode than on the higher modes. In fact, the acoustic radiation damping values for the higher modes are nearly an order of magnitude less than the first mode. The second mode was excited by applying a point force at $x=0.05\text{m}$ with the response calculated at $x=0.15\text{m}$.

3.2.2 Finite Plate

The following figures contain results for various aluminum and laminated composite plates. For these cases the plate is clamped in an infinite baffle with flow on one side. First, calculations based on Eq. (2.18) are compared with existing calculations and data. As for the semi-finite strip, the fluid is air at standard atmospheric conditions.

Wilby [29] measured the total damping for a number of steel panels up to Mach 0.5. The acoustic radiation damping component was measured by subtracting the total damping at Mach 0 from the total damping at Mach 0.5. The structural damping component was assumed constant with Mach number. Figure 3.12 contains the results

for a number of modes of these panels. The damping calculated using Eq. (2.18) at Mach 0 was subtracted from that at Mach 0.5. Although, some of the points show a factor of 3 difference between the present results and Wilby, most of the points are within a factor of 2. The measured mean damping values were reported to have a $\pm 25\%$ variation. In addition, measurement/instrumentation errors could cause overprediction of the experimental values [29].

Chyu [5] used an analysis similar to the perturbation approximation to predict the acoustic radiation damping. A comparison between the perturbation approximation results, Eq. (2.29), and Chyu's are given in Figure 3.13 for a steel plate, $0.0889 \times 0.0889 \times 0.000381\text{m}$, subjected to a Mach 0.3 flow. The agreement between these two analyses is good.

The effect of a/b ratio on acoustic radiation damping is given in Figure 3.14. For these calculations a was kept constant at 0.2m and b was allowed to vary. The thickness is $h=0.001\text{m}$. Thus as b becomes large, then $a/b \rightarrow 0$ and the result is a semi-infinite strip. The semi-infinite strip results have been added next to the left axis of the figure. Increasing the Mach number raises the damping vs. a/b ratio curve, except at the higher ratio values. At large a/b , the convergence of the curves is predicted by piston theory. The square near the right axis corresponds to a no flow semi-infinite strip calculation where the chord is 0.025m . This result has been compared to that for a finite plate where $a=0.2\text{m}$ and $b=0.025\text{m}$ (or $a/b=8$). Finally, note that the acoustic radiation damping at $M=0.6$ is greater than or equal to the assumed structural value, except for the higher a/b ratios.

The frequency ratio and acoustic radiation damping for a number of laminated composite plates are presented in Figures 3.15–3.20. Results for an aluminum plate with the same dimensions has been included for comparison purposes. The plate dimensions are $a=0.2\text{m}$, $b=0.3\text{m}$ and $h=0.001\text{m}$. Previous results showed that the first mode had acoustic radiation damping values approximately an order of magnitude greater than the higher modes. For this reason only the first mode results will be presented. The first mode damping values for isotropic plates were also found to be calculated accurately by a single product of beam functions. Since the laminated composite plates are orthotropic or quasi-isotropic, then the mode shapes are nearly the same as the isotropic case. Thus the results presented here are for a single product of beam functions for the first mode. The results presented in Figures 3.15–3.18 are to emphasize the differences between laminated composite and isotropic plates (such as aluminum).

In Figure 3.15, the graphite/epoxy plates have the same outside fiber direction, which is aligned with the flow, 0° . The $[0,\pm 45,90]_s$ and aluminum plates have nearly the same modal frequency. However, the difference in damping results from the different mass ratios, μ . This is apparent in the perturbation approximation, Eq. (2.29), where the damping is proportional to the mass ratio. Note that all of the damping ratios are significantly larger for the graphite/epoxy plates than the aluminum plate. In addition, all of the graphite/epoxy plates have acoustic radiation damping ratios of approximately the same magnitude.

In Figure 3.16, the frequency and damping ratios are for the baseline aluminum and graphite/epoxy plates where the outside fiber direction is perpendicular to the

flow, 90° . At the lower Mach number, well below divergence, the damping ratios for the graphite/epoxy plates are greater than that for the aluminum. These graphite/epoxy plates diverge at a much lower Mach number than the aluminum plate. This is due to the decreased stiffness of the graphite/epoxy plates in the flow direction.

In Figures 3.17 and 3.18, the composite plates are carbon/carbon. The damping and frequency ratio trends for the carbon/carbon plates are similar to those for the graphite/epoxy plates. The laminates where the outside fiber direction is aligned with the flow, Figure 3.17, show less effect on frequency ratio than the aluminum plate. In addition, the damping for the carbon/carbon plates is much greater than an aluminum plate with the damping for the two carbon/carbon plates approximately equal.

Figure 3.18, where the outside fiber direction is perpendicular to the flow, shows a greater effect on frequency ratio than for the aluminum plate. In addition, the carbon/carbon plate still has a larger damping ratio as compared to the aluminum

Comparisons of Figures 3.15 through 3.18 show the same trends are evident for the graphite/epoxy and carbon/carbon plates. In particular, the outside fiber direction strongly influences the laminated composite acoustic radiation damping and modal frequencies. The material property, graphite/epoxy or carbon/carbon, are less important when the outside fiber direction is aligned with the flow. This results from the fiber Young's modulus (E_{11}) for the two lamina types having approximately equal magnitude. The material properties, in particular the matrix property is more important when the outside fiber direction is perpendicular to the flow. Note that the matrix Young's modulus (E_{22}) for the two lamina types differ by almost a factor of 2. In addition, the composite plates where the outside fiber direction is perpendicular to

the flow diverge at a lower Mach number. The gross difference in acoustic radiation damping and modal frequencies depending on the outside fiber direction implies that laminated composite plates can be tailored to obtain high acoustic radiation damping values and to delay or prevent divergence.

In general, the acoustic radiation damping for laminated composite plates is significantly greater than for the aluminum plates. These comparisons were based on similar thickness plates. Comparisons based on equivalent stiffnesses would require thicker aluminum plates resulting in lower acoustic radiation damping values. Thus the net difference between the aluminum and composite plates would be even larger.

The data in Figures 3.15–3.18 have been compressed to demonstrate the ability to develop compact design curves to predict acoustic radiation (or aerodynamic) damping. The damping ratio normalized by the mass ratio is plotted against a reduced frequency factor, $k_1 = \sqrt{\frac{\Omega_{m, \text{in-vacuo}}}{1 - \mu C_2^{mm}(k_{res}, M, l)}} \sqrt{\frac{D_{11}}{\rho h a^2 c_0^2}}$, in Figure 3.19. The reduced frequency was selected for the abscissa based on the perturbation approximation relationship. It was shown that $C_1^{mm}(k, M, l)$ varies linearly with k for many plates of interest. Note that $C_2^{mm}(k, M, l)$ must be evaluated at the resonant (not the in-vacuo) reduced frequency for the mode of interest (in this case, the first mode). For constant a/b ratio and constant Mach number, the data form a straight line. A least mean square (LMS) algorithm was used to fit a straight line through the data. These results include typical aircraft sidewall panels and plates near divergence. Most of the data are for plates of the same size ($a=0.2\text{m}$, $b=0.3\text{m}$, $h=0.001\text{m}$). Additional data for aluminum plates with $a/b=0.6667$ and $M=0.6$, but varying plate thickness and area have been included for comparison.

To eliminate the need to evaluate the $C_2^{mm}(k, M, l)$ integral, the reduced frequency factor was approximated as $k_2 = \sqrt{\frac{D_{11}}{\rho h a^2 c_0^2}}$, see Figure 3.20. For typical aircraft panels subjected to flows less than or equal Mach 0.6, this approximation was reasonably accurate. However, at $M=0.8$, where the flow can significantly change the plate stiffness of the plates near divergence, the approximation is no longer valid. An LMS algorithm was fit through the points for plates not near divergence.

The results presented in Figures 3.19 and 3.20 indicate that design curves can be constructed to predict the acoustic radiation (or aerodynamic) damping of lightweight structures. For aerospace applications, where aircraft sidewall panels are not designed to operate near divergence, the design curves need not include flow effects on the plate resonant frequency. Thus the computations are greatly simplified due to the elimination of the two-dimensional integral evaluation of C_2 .

Table 3.1. Material Properties

<i>Material</i>	$E_{11} \times 10^9$ (N/m^2)	$E_{22} \times 10^9$ (N/m^2)	ν_{12}	$G \times 10^9$ (N/m^2)	h_{lamina} (m)	ρ_p (kg/m^3)
Aluminum	72.	72.	0.33	27.4	—	2700.
Steel	200.	200.	0.28	83.	—	7700.
Graphite/Epoxy	163.	10.2	0.3	6.48	.000125	1600.
Carbon/Carbon	138.	6.89	0.08	1.03	.00025	1860.
PZT	82.	82.	—	—	.000254	7600.

Table 3.2. Plate Mode(m) to Beam Function Pair (r,s) Correspondence

m	r	s
1	1	1
2	1	2
3	1	3
4	1	4
5	1	5
6	2	1
7	2	2
8	2	3
9	2	4
10	3	1
11	3	2
12	3	3

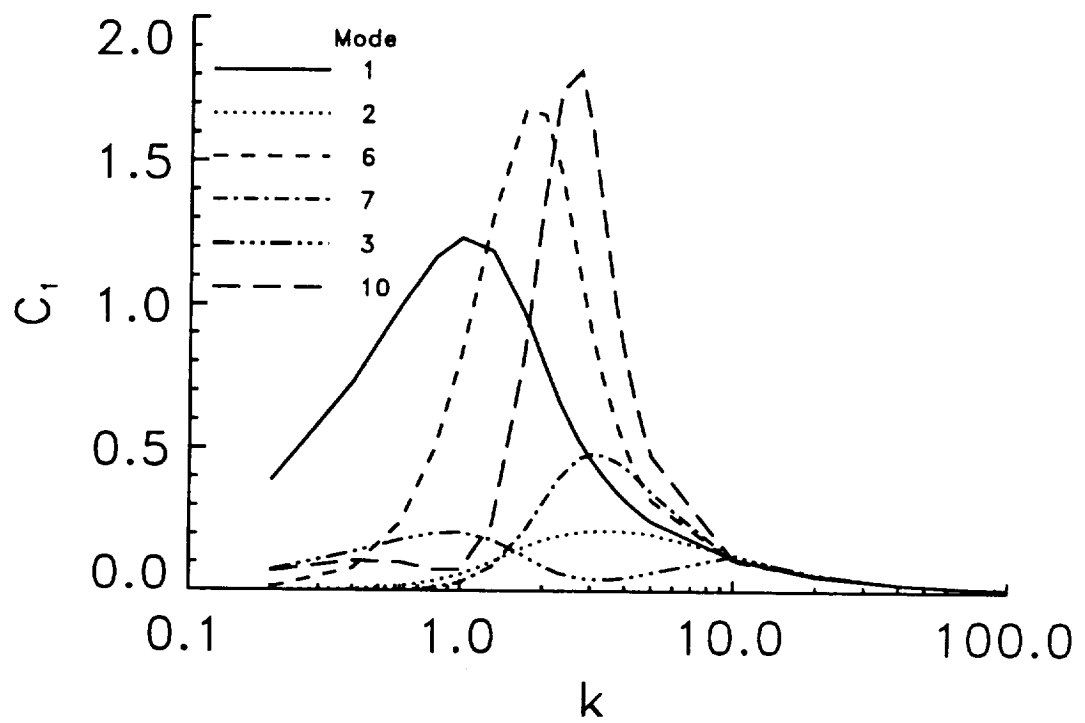


Figure 3.1. Effect of reduced frequency and mode number on C_l .

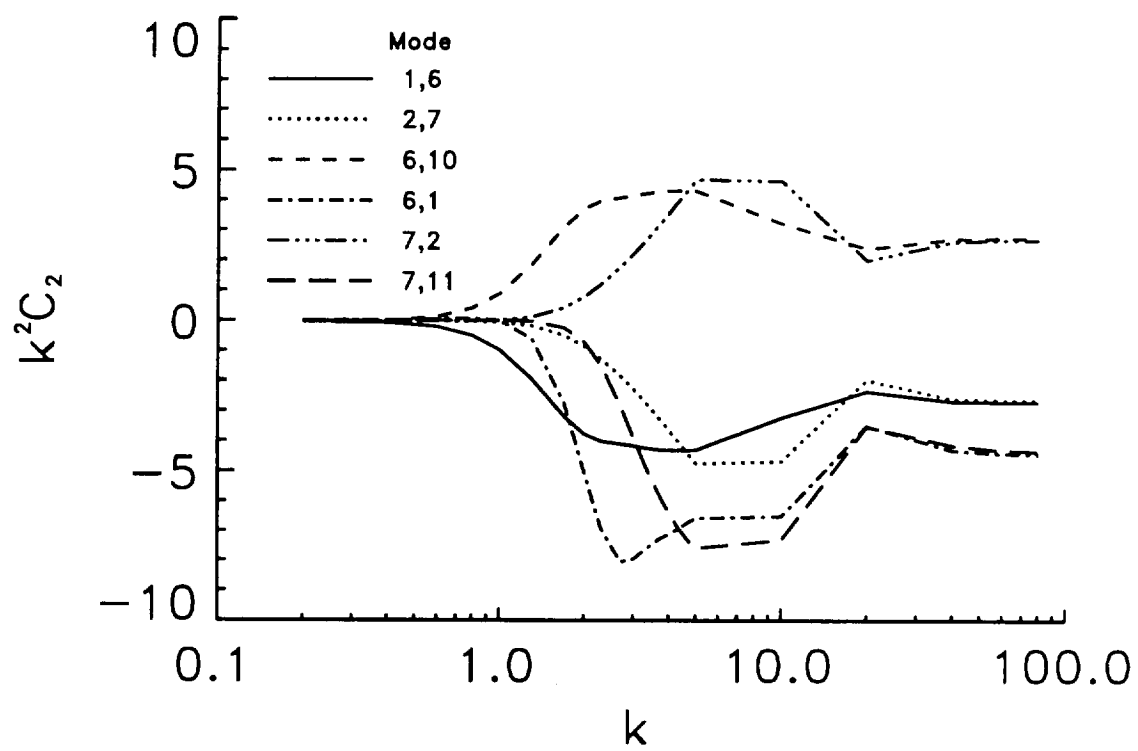


Figure 3.2. Effect of reduced frequency and mode number on $k^2 C_2$.

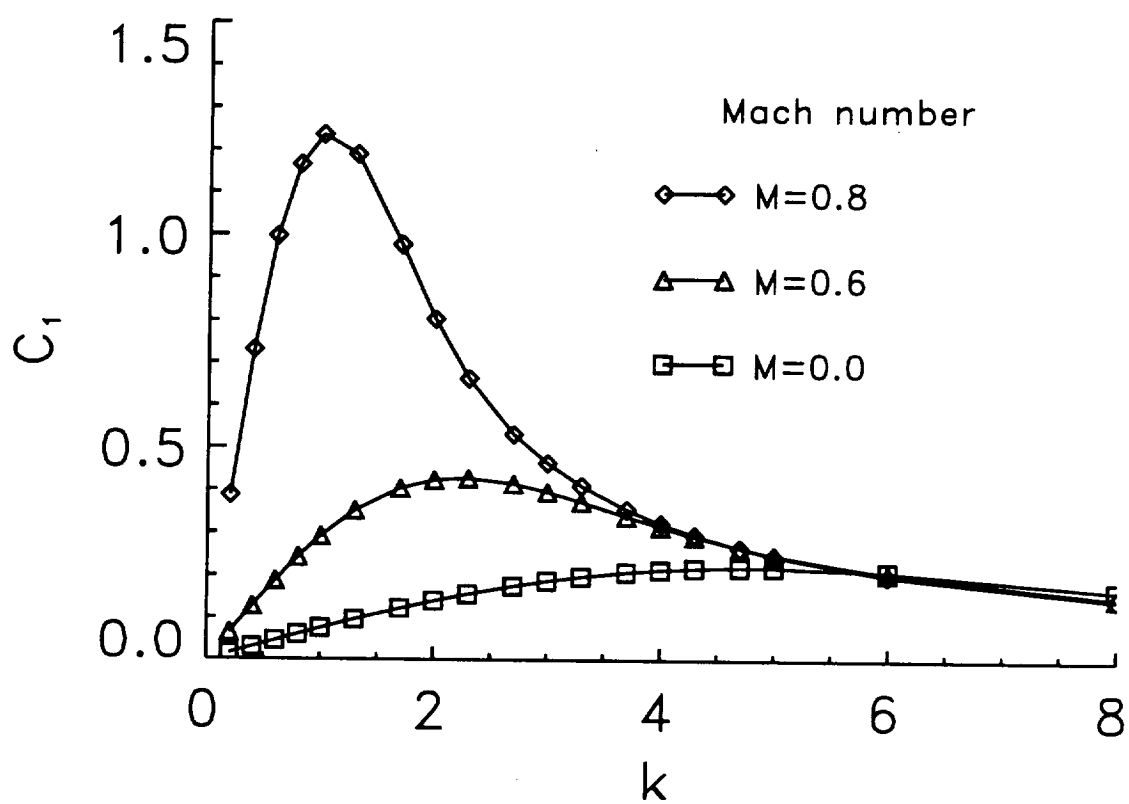


Figure 3.3. Effect of Mach number on first mode C_1 .

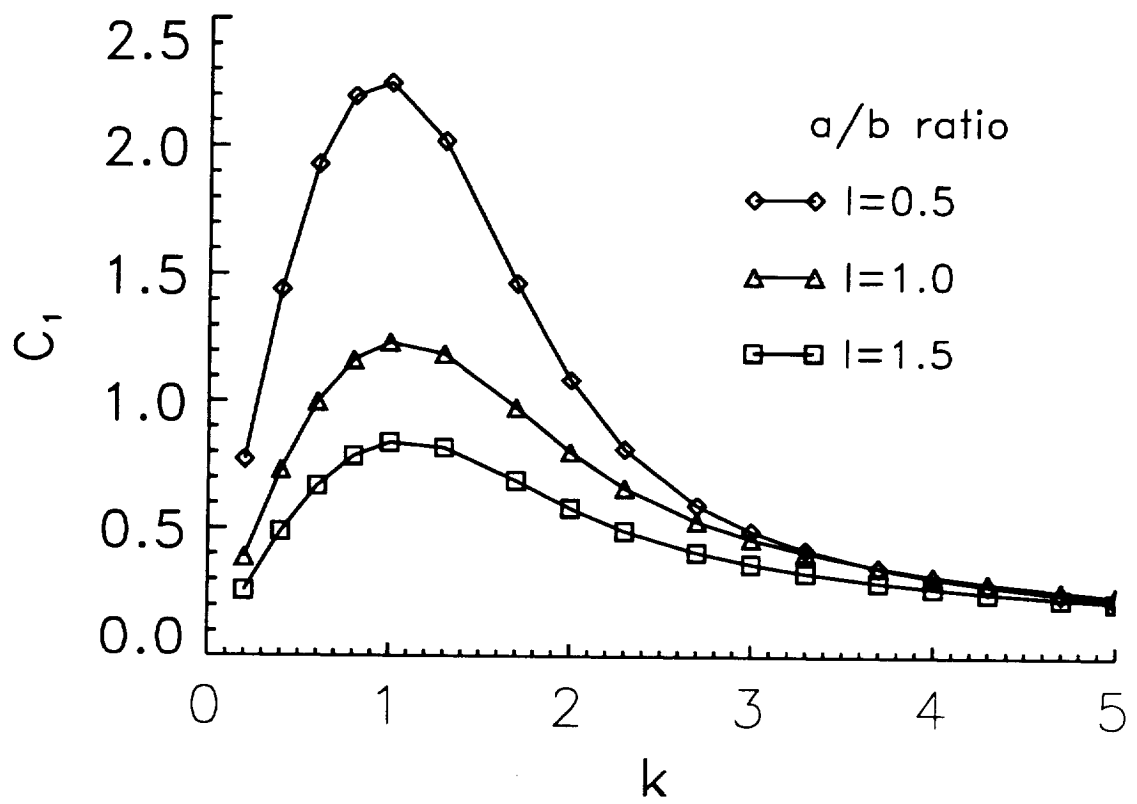


Figure 3.4. Effect of aspect ratio number on first mode C_1 .

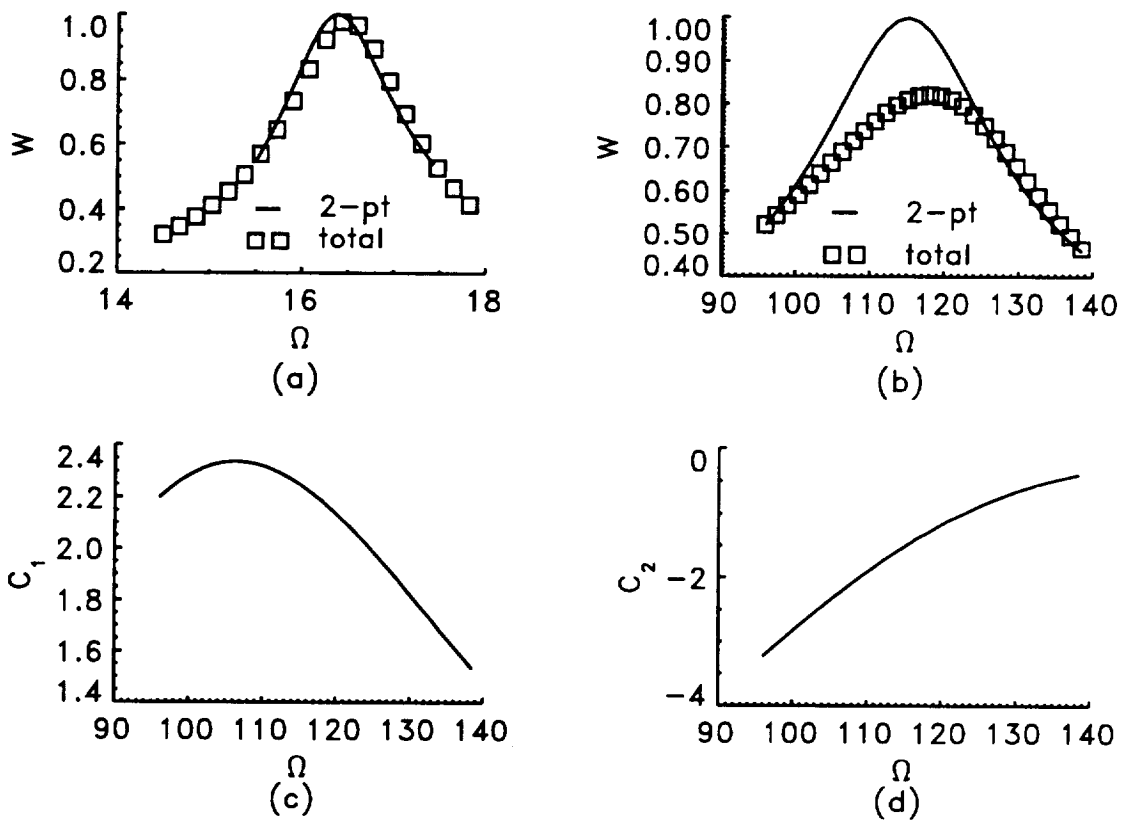
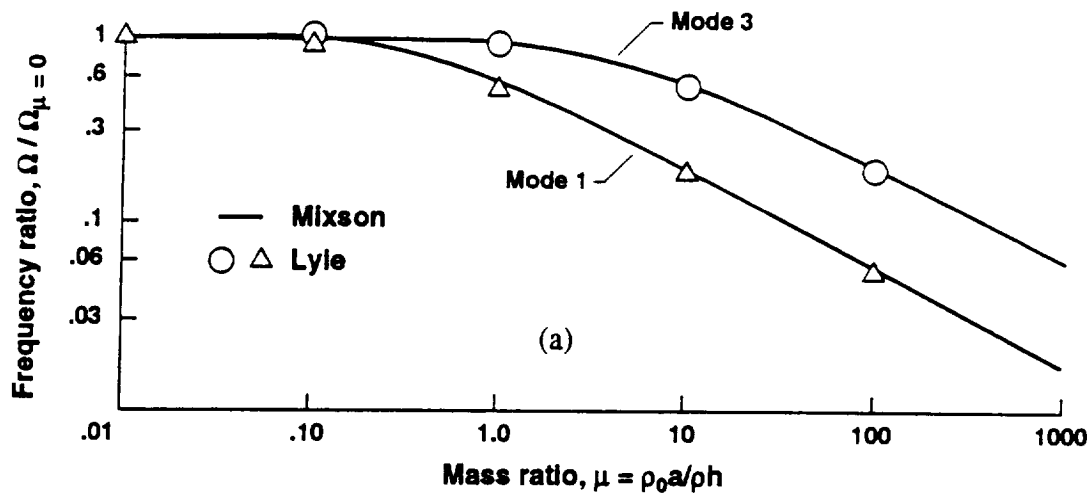
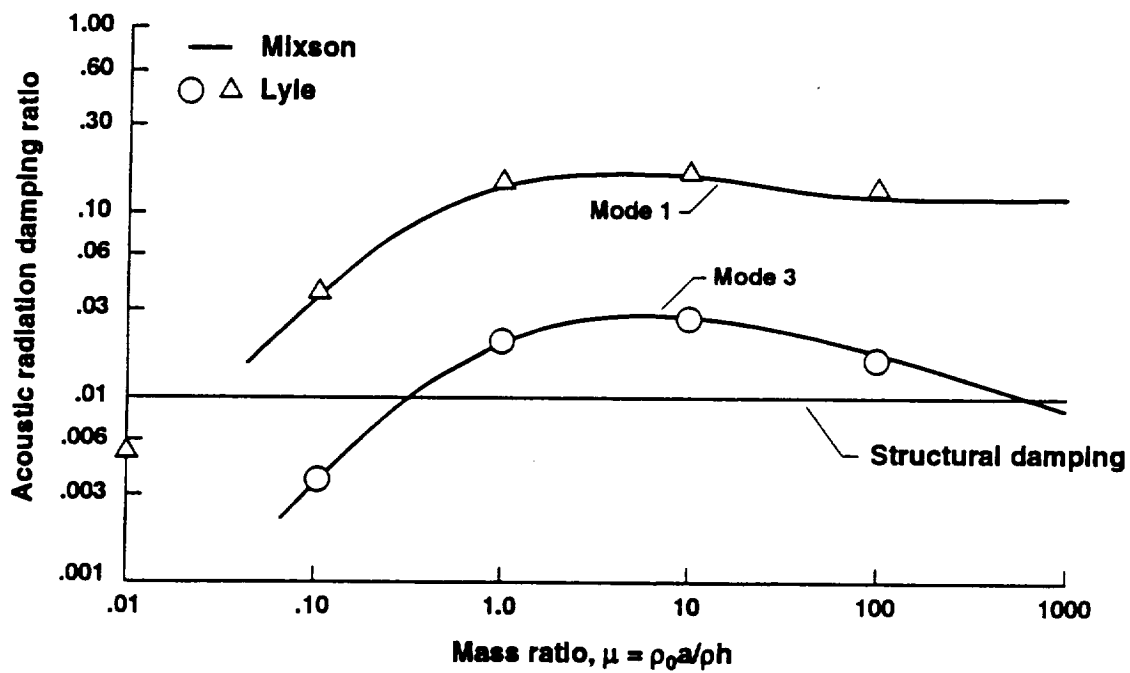


Figure 3.5. Comparison of total and 2-point prediction methods at $M=0.8$ for (a) mode 1 and (b) mode 10 with Mode 10 variation of (c) C_1 and (d) C_2 .



(a)



(b)

Figure 3.6 Effect of mass ratio and mode number on (a) frequency ratio and (b) damping ratio

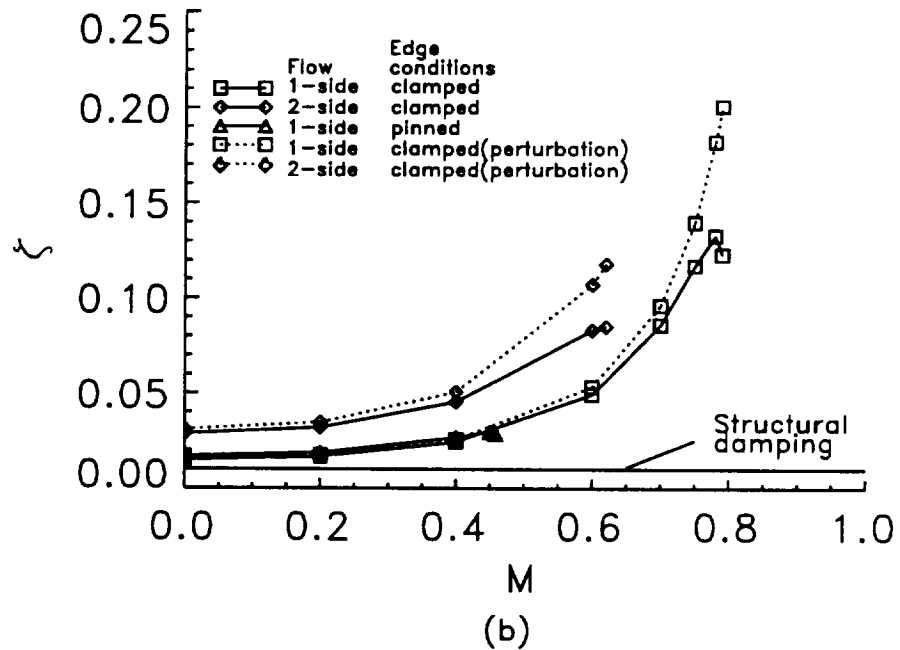
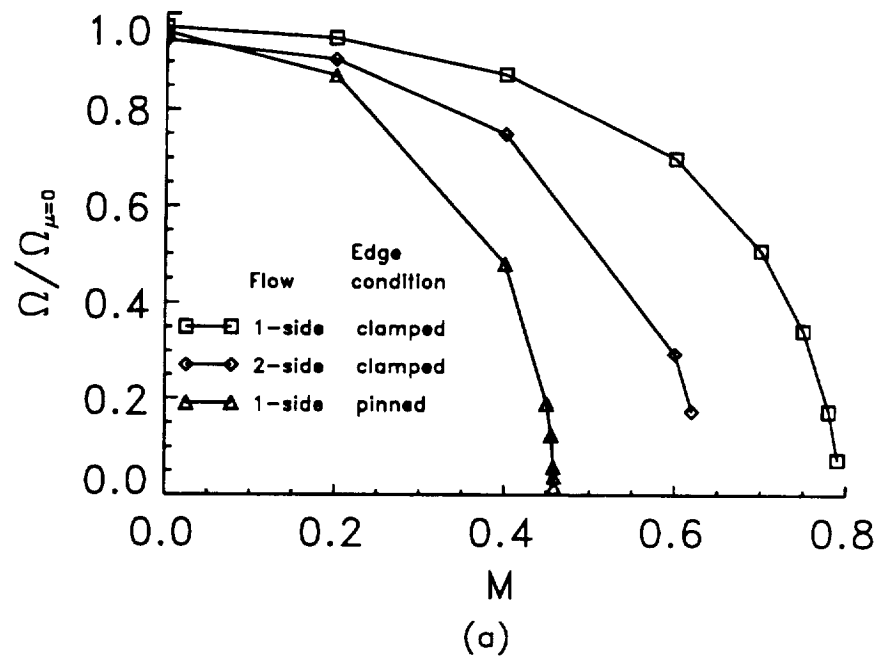


Figure 3.7. Effect of Mach number, edge conditions and flow on (a) frequency ratio and (b) damping ratio.

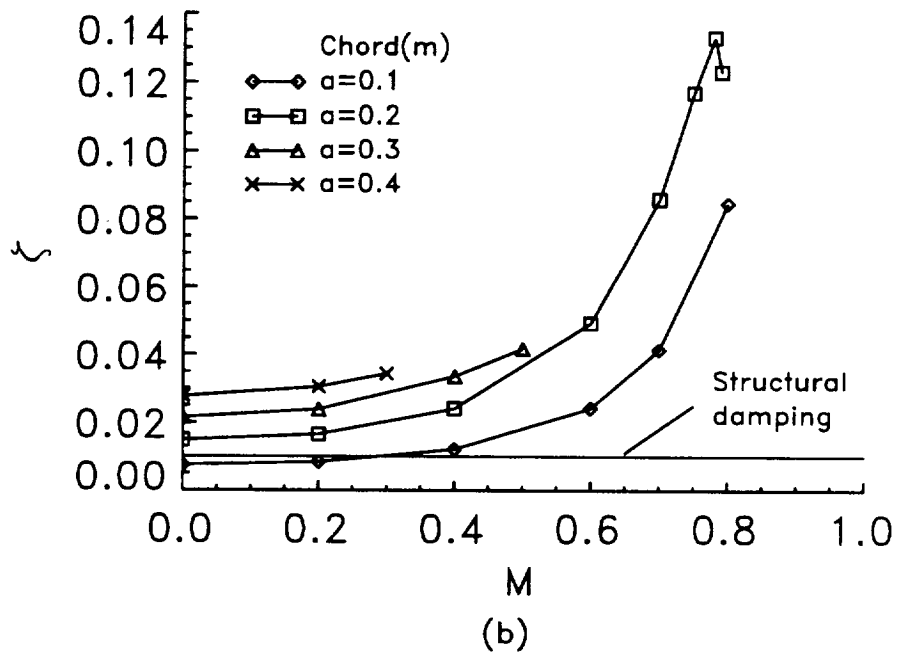
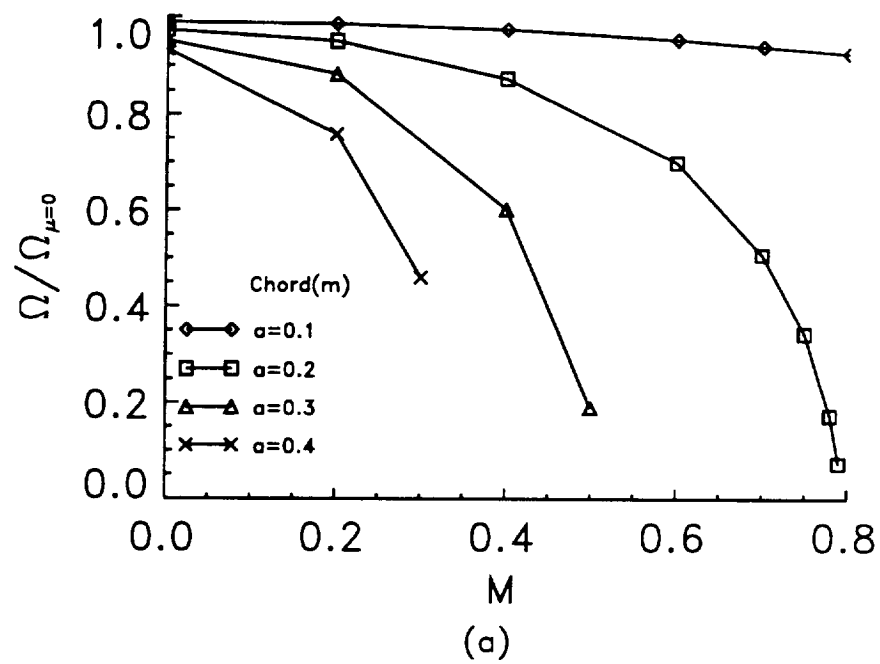


Figure 3.8. Effect of Mach number and chord on (a) frequency ratio and (b) damping ratio.

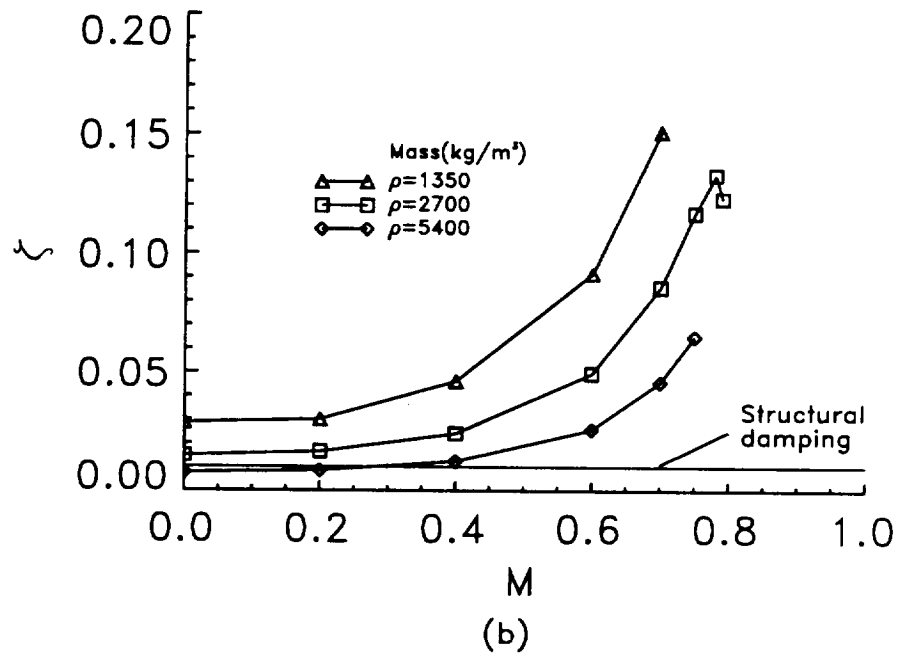
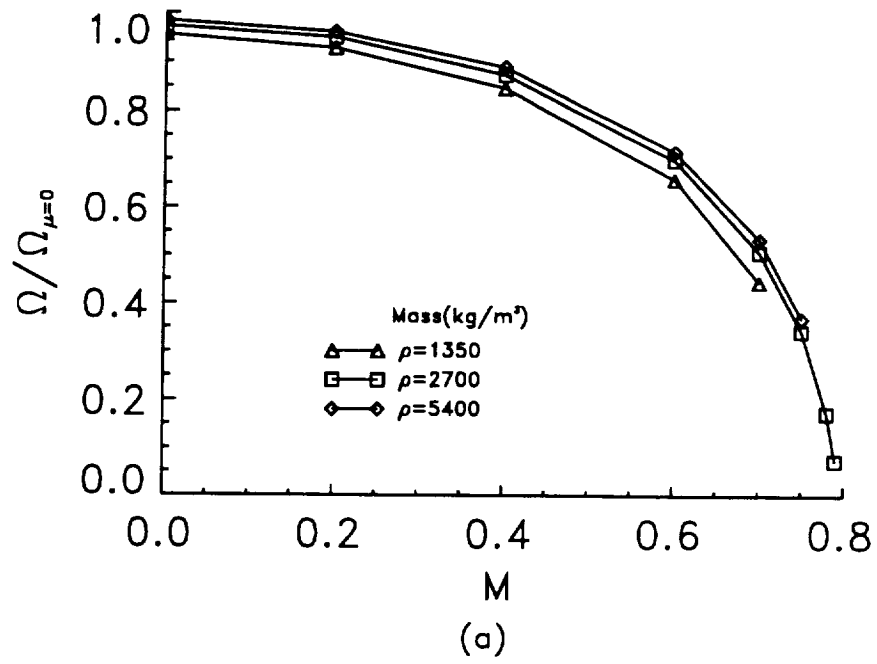


Figure 3.9. Effect of Mach number and plate mass on (a) frequency ratio and (b) damping ratio.

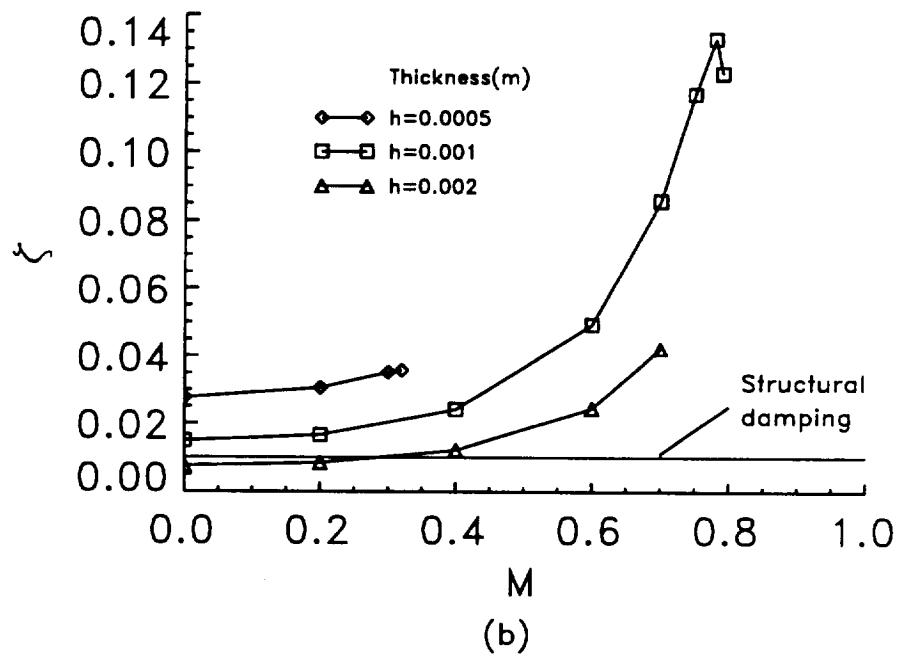
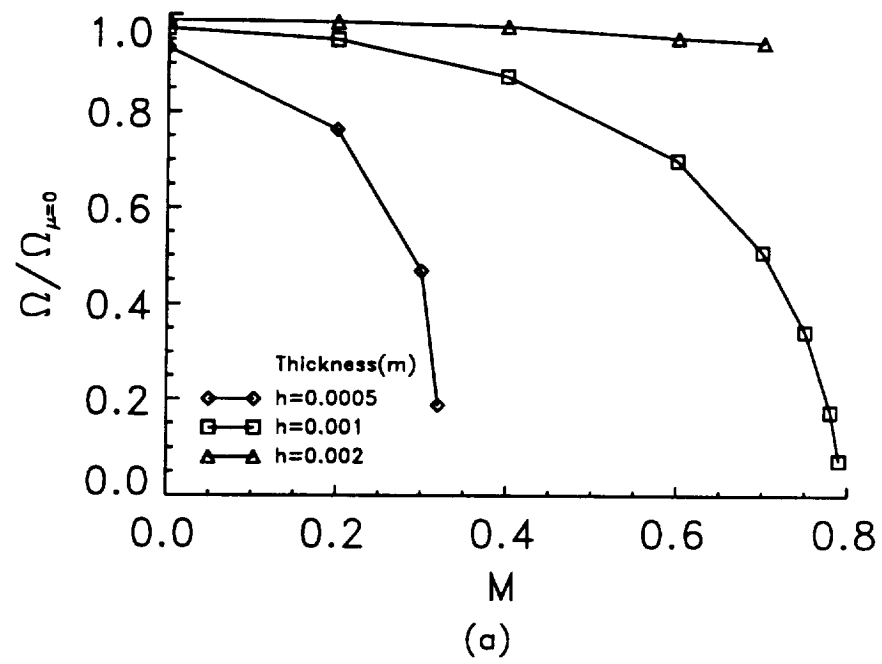


Figure 3.10. Effect of Mach number and plate thickness on (a) frequency ratio and (b) damping ratio.

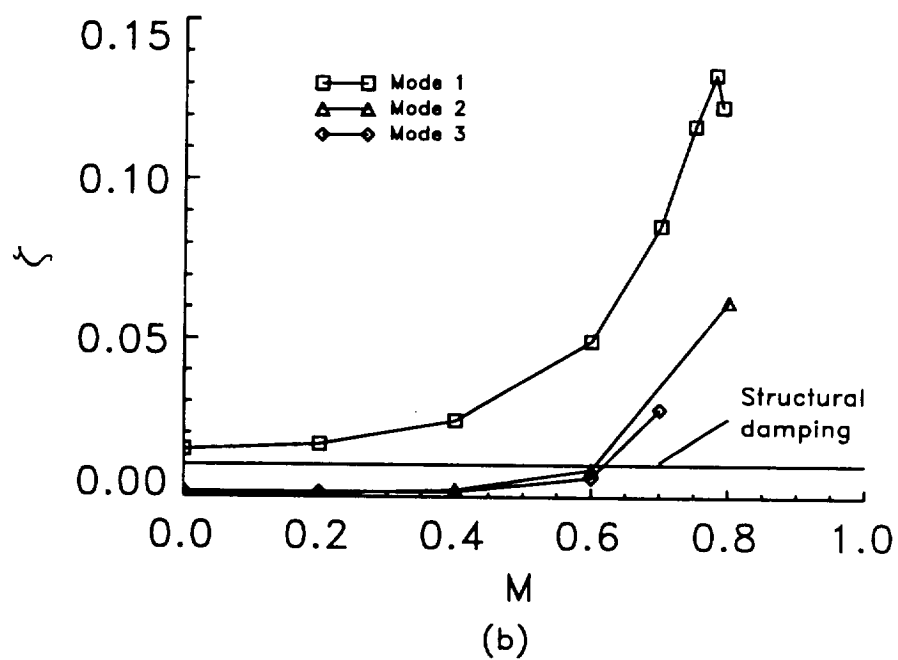
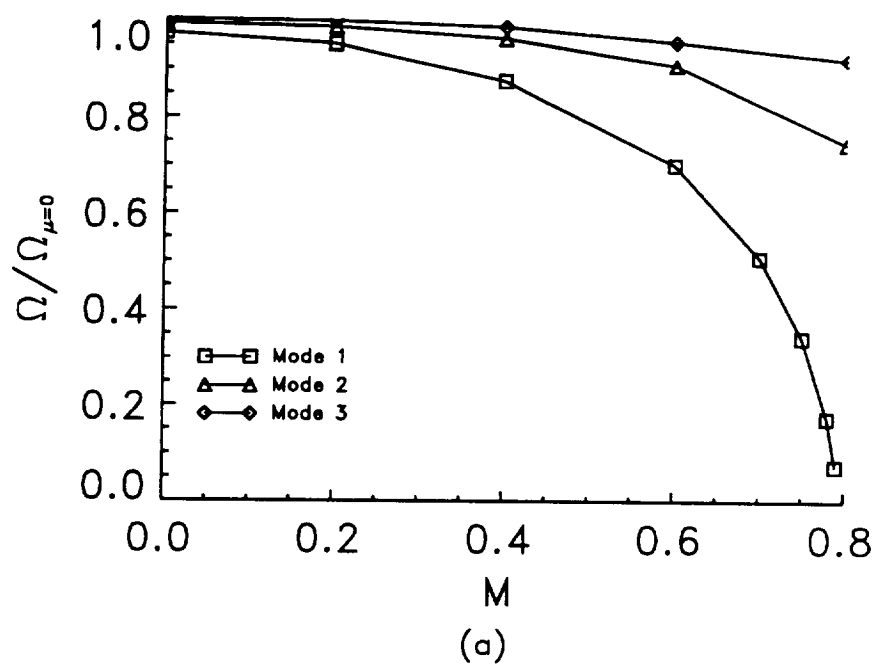


Figure 3.11. Effect of Mach number and mode number on (a) frequency ratio and (b) damping ratio.

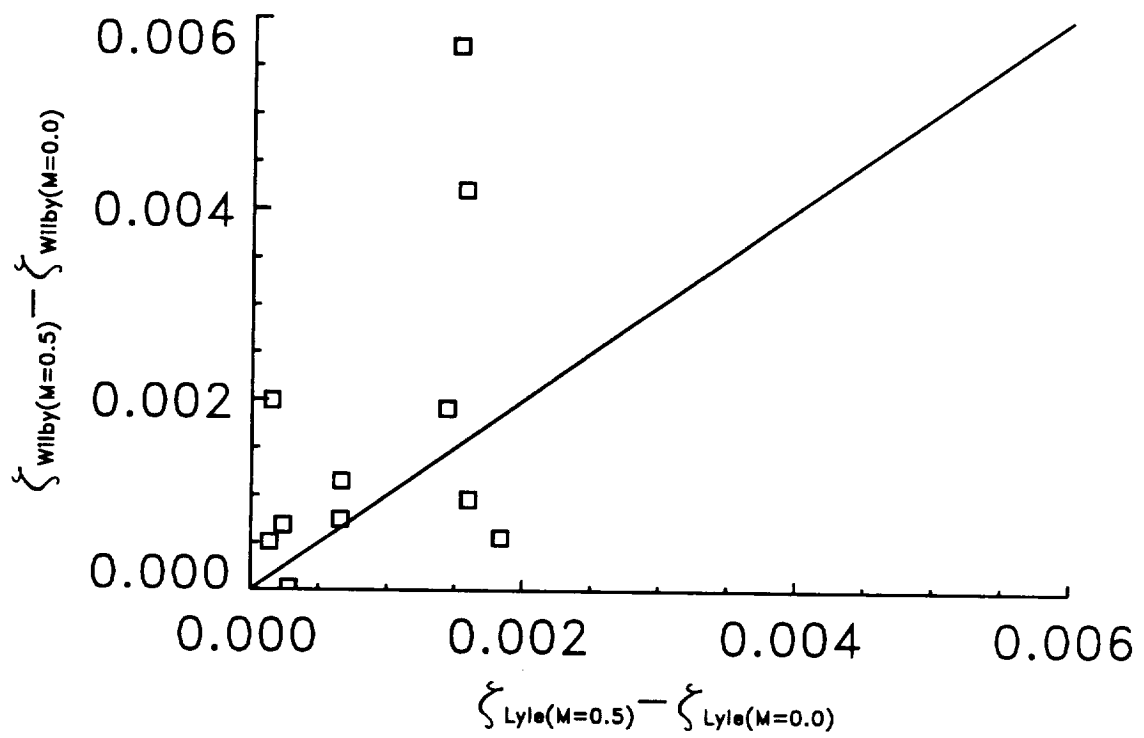


Figure 3.12. Comparison of Wilby and Lyle acoustic radiation damping ratios.

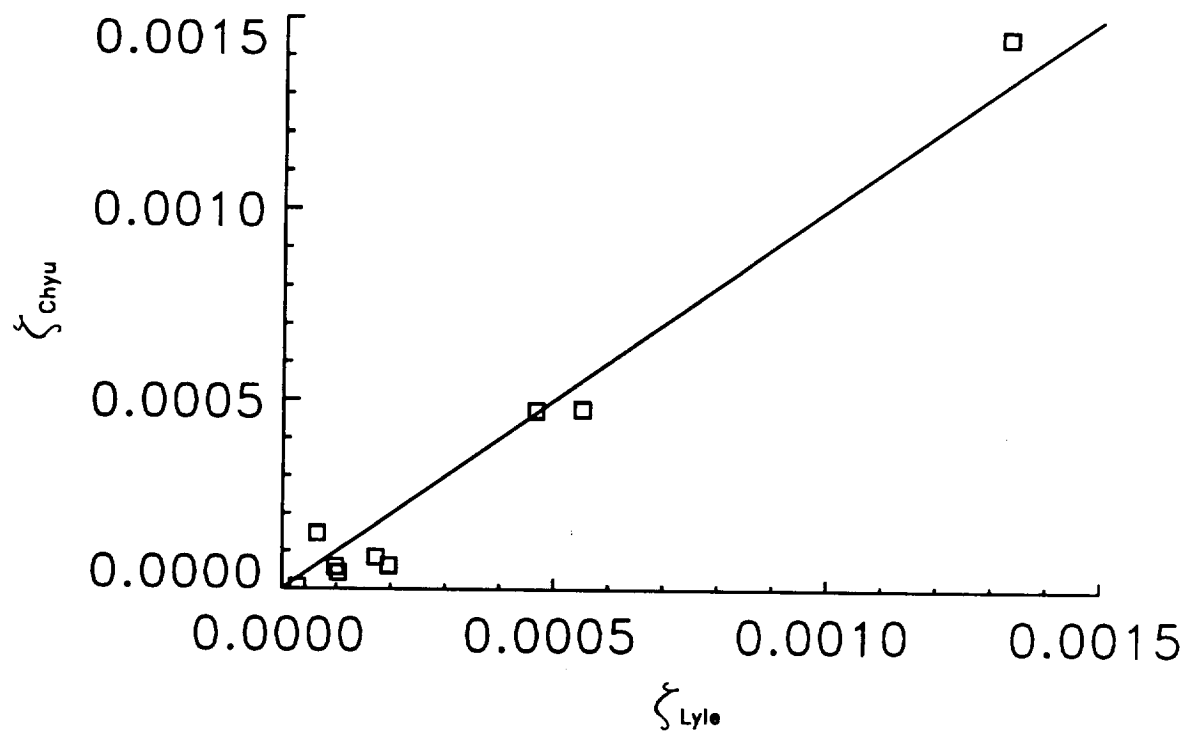


Figure 3.13. Comparison of Chyu and Lyle acoustic radiation damping ratios.

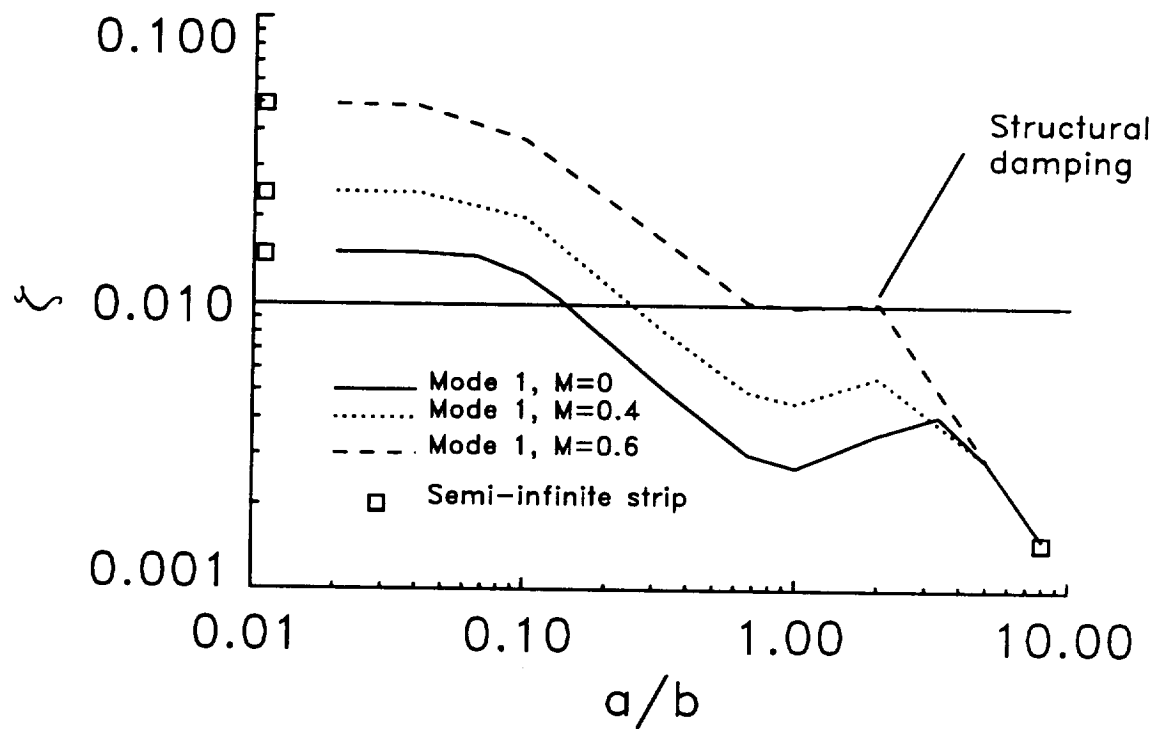


Figure 3.14. Effect of aspect ratio on acoustic radiation damping.

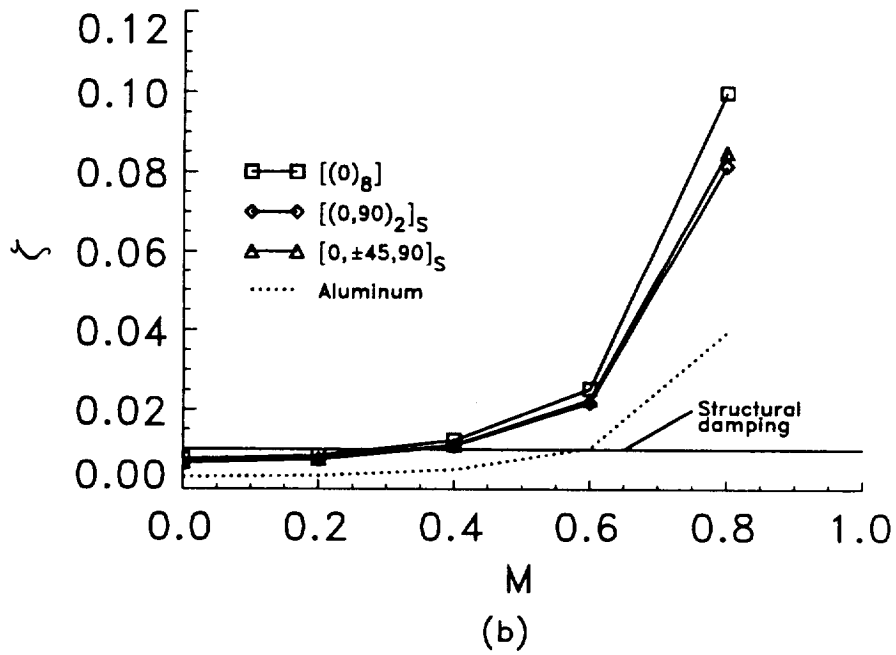
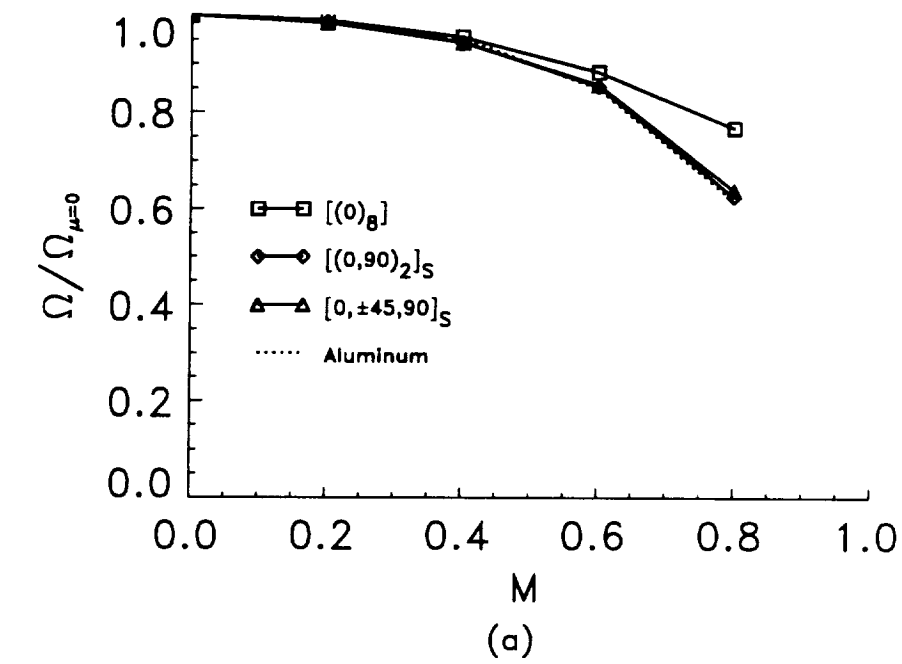


Figure 3.15. Effect of Mach number on (a) frequency ratio and (b) damping ratio for graphite/epoxy plates with outside fiber aligned with flow, 0° .

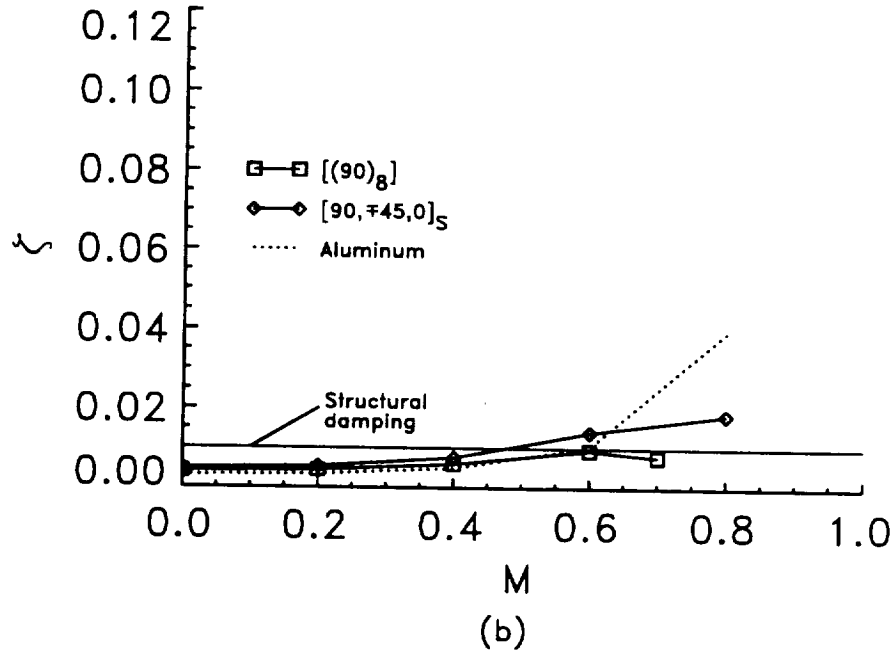
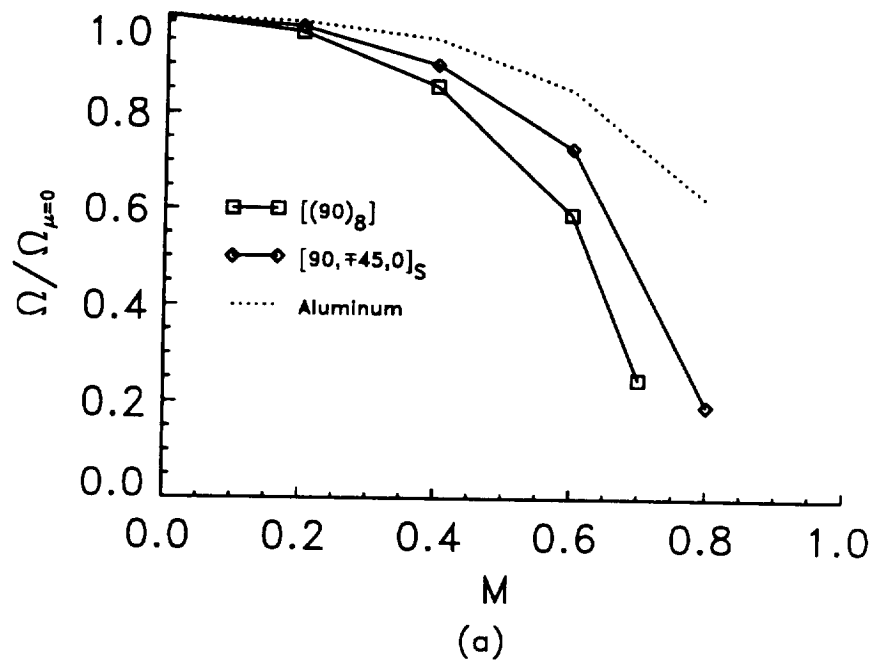


Figure 3.16. Effect of Mach number on (a) frequency ratio and (b) damping ratio for graphite/epoxy plates with outside fiber perpendicular to flow, 90°.

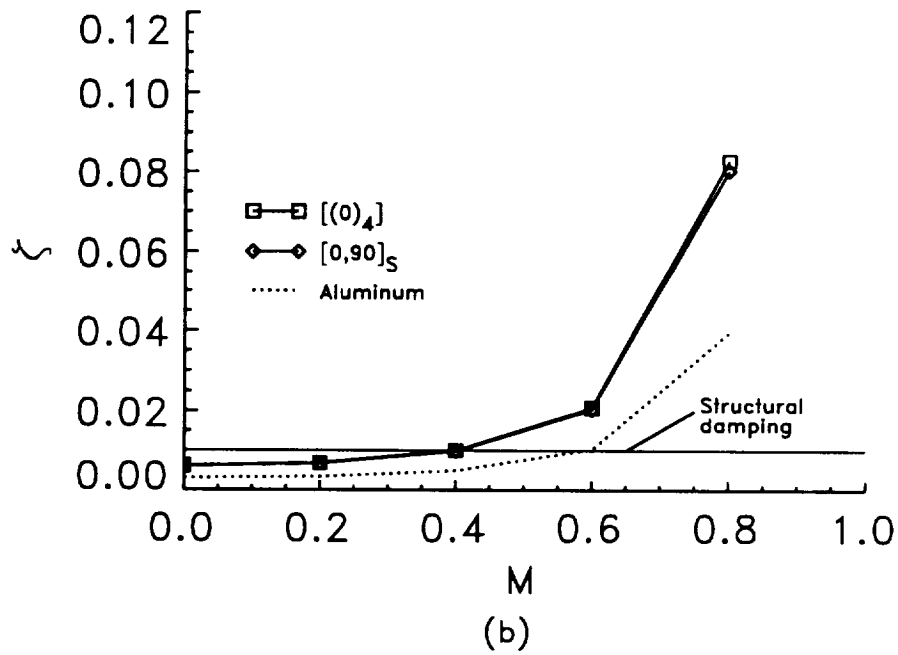
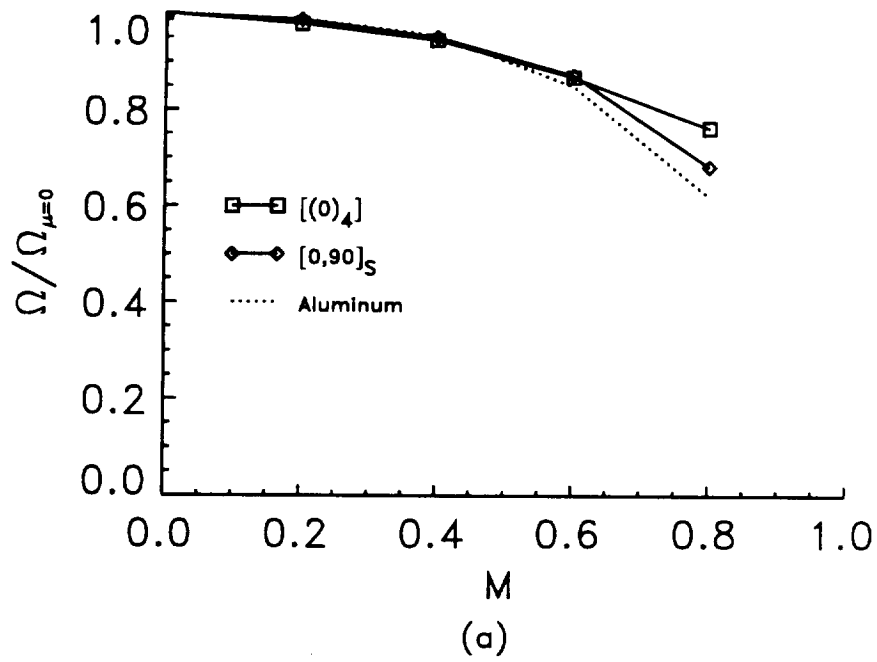


Figure 3.17. Effect of Mach number on (a) frequency ratio and (b) damping ratio for carbon/carbon plates with outside fiber aligned with flow, 0° .

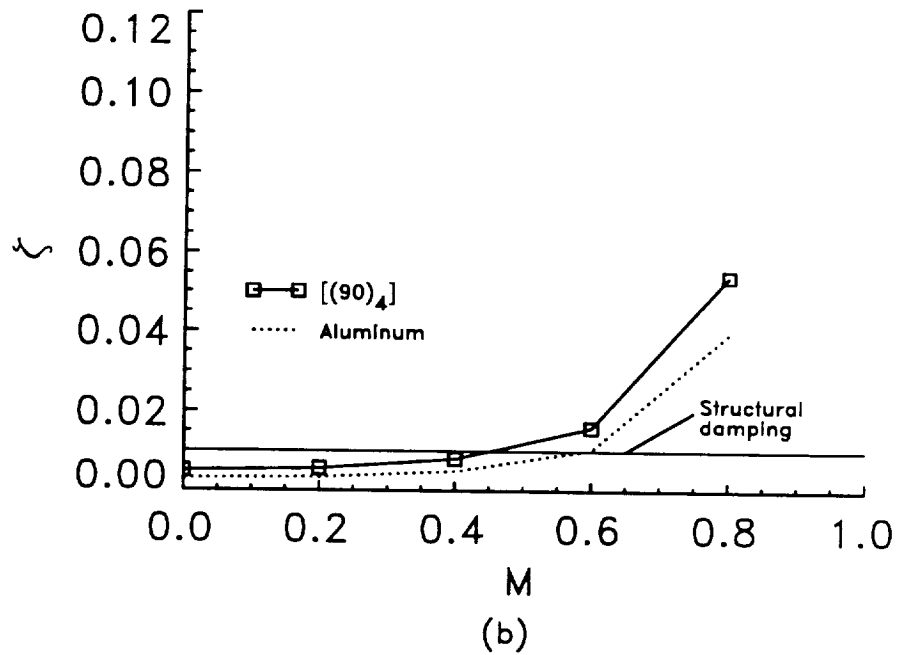
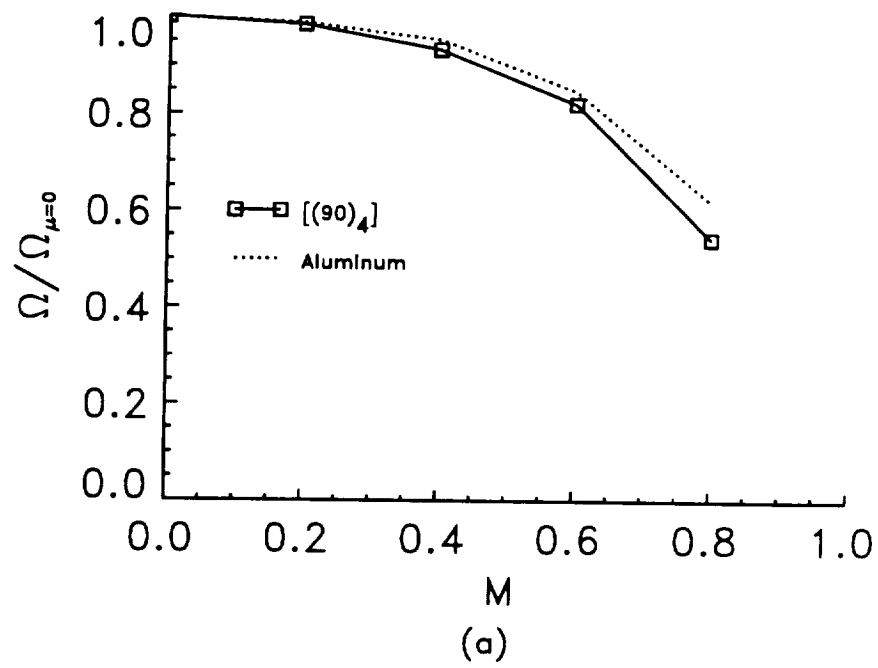


Figure 3.18. Effect of Mach number on (a) frequency ratio and (b) damping ratio for carbon/carbon plates with outside fiber perpendicular to flow, 90° .

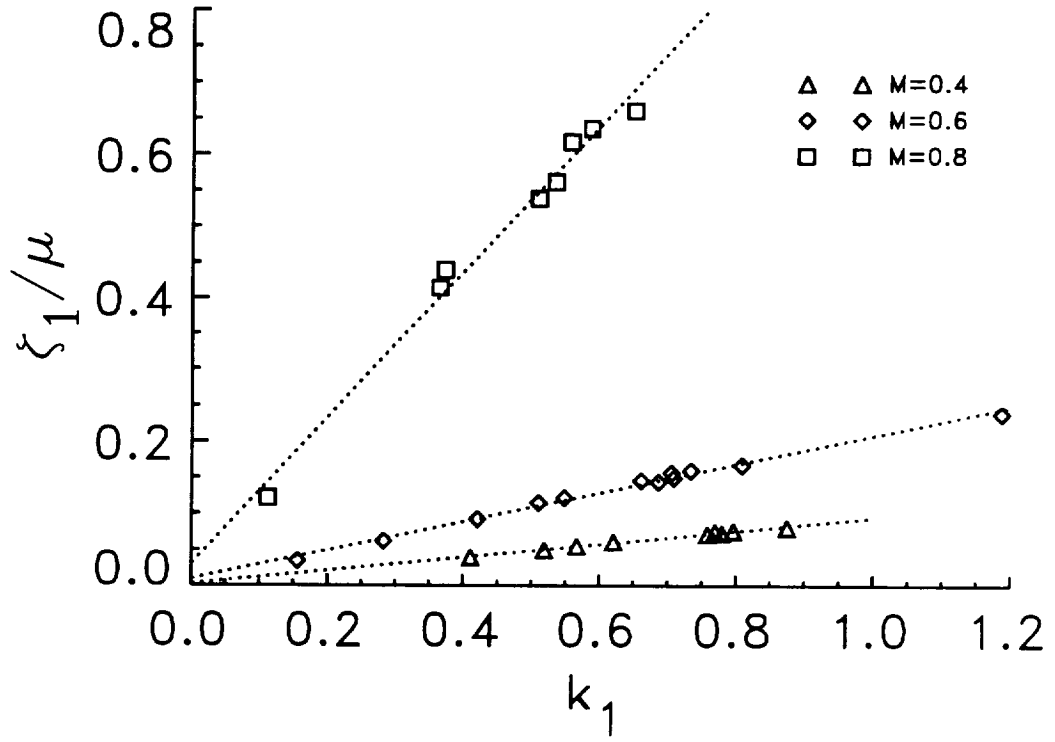


Figure 3.19. Damping ratio normalized by mass ratio as a function of $k_1 = \sqrt{\frac{\Omega_{m, in-vacuum}}{1-\mu C_2^{mm}(k_{res}, M, l)}} \sqrt{\frac{D_{11}}{\rho h a^2 c_0^2}}$ for $a/b=0.66667$.

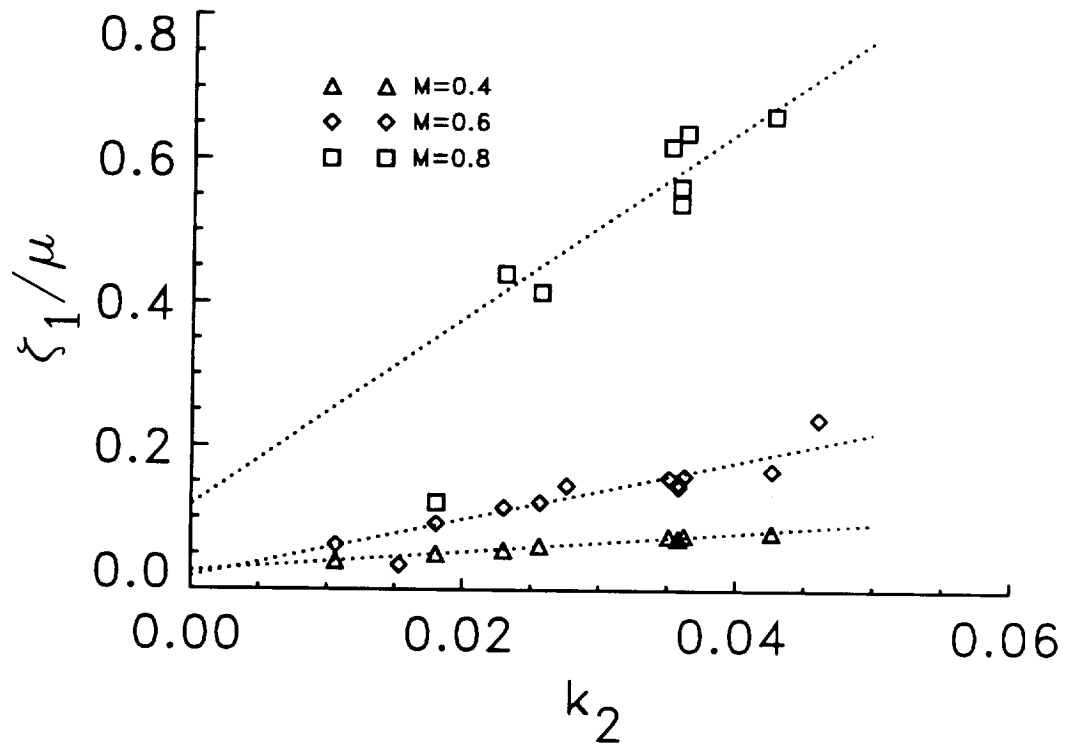


Figure 3.20. Damping ratio normalized by mass ratio as a function of $k_2 = \sqrt{\frac{D_{11}}{\rho h a^2 c_0^2}}$ for $a/b=0.66667$.

CHAPTER 4 EXPERIMENT

Due to the small data set of existing experimental damping values, an exploratory experiment was designed to acquire data for comparison with the analysis. Before designing the test apparatus, a number of facilities at NASA Langley were evaluated for not only the flow capabilities but also scheduling requirements. It was appreciated that such experiments are difficult to perform and that existing data for subsonic flow show substantial scatter [29].

4.1 Description of Test Setup

The test model was designed for installation in the Quiet Flow Facility at NASA Langley Research Center. A photograph with the model installed in the facility and accompanying facility schematic are seen in Figure 4.1. The facility is a 6.1 x 7.3 x 9.2m anechoic chamber with the nozzle centerline located at 3.65m above the floor. Wedges lining the chamber provide an essentially echo-free environment (absorption coefficient of 0.995) down to about 70 Hz.

The facility was operated as an open-loop, blow-down system with three pressurized spheres providing the air source. The airflow exhausts to the atmosphere through the openings in the facility wall and ceiling. This system was capable of maintaining a uniform flow at $M=0.6$ for approximately 5 minutes. At lower Mach numbers, e.g. $M=0.3$, the run-time can be considerably extended. A maximum performance up to Mach 2.1 with a 0.038m nozzle is projected. The nozzle used for these tests was 0.3048m in diameter with a maximum capability of Mach 0.9. The variation of total pressure at various cross-sections parallel to the nozzle face

was previously measured using a traversing microphone system. The horizontal variation at 0.508m and 0.762m have been plotted in Figure 4.2. In addition, the vertical variation at 0.508m for $M=0.6$ has also been included. The results show a very uniform pressure in the jet core. The test plate studied here was approximately 0.584m from the nozzle exit. Even at 0.762m the test plate was well within the jet core, see Figure 4.2. During all test runs the chamber conditions, i.e., temperature, humidity and pressure, were monitored.

A photo of the model in-situ is shown in Figure 4.3. The model dimensions are given in Figure 4.4. To approximate two-dimensional airflow over both sides of the plate, two horizontal baffles were placed near the plate edges. The airfoils above and below the baffles were incorporated to make the flow as symmetric as possible. The plate is placed between nominally identical symmetric fore and aft airfoils, such that the leading edge of the elastic test plate is attached to the trailing edge of the leading airfoil, while the trailing edge of the elastic test plate is attached to the leading edge of the aft airfoil, see Figure 4.5. Pressure taps were symmetrically located in the airfoils to make sure that the plate is aligned with the flow and thus the plate is not exposed to lifting forces (i.e. a static pressure differential). The affect of flow on both sides of the plates doubles the C_l and C_d integrals. This results in approximately doubling the acoustic radiation damping.

Details of the clamping mechanism for the elastic test plate are shown in Figure 4.6. The plate leading edge is secured between the upper and lower airfoil halves with the screws going through the plate. This edge was assumed to have classical pinned conditions. The plate trailing edge is inserted into a slot formed by the leading

edge of the upper and lower halves of the trailing airfoil. This slot was designed to allow the plate to expand or contract freely, without allowing rotation. Thus the plate trailing edge was assumed to have classical clamped conditions. The plate was expected to expand and contract due to temperature changes caused by the airflow.

The plate was instrumented with strain gages and PZT (lead-zirconate-titanate) patches (piezo-electric devices), as seen in Figures 4.7 and 4.8. Two pairs of strain gages were symmetrically bonded near the trailing edge of the plate to measure the y-direction bending strain. Three pairs of PZT patches ($0.0254 \times 0.0127 \times 0.00025\text{m}$) were also symmetrically bonded. The PZT patches can be used to either excite the structure or measure the structural response. In this case the PZTs were intended to excite the bending motion of the plate by driving the three patches on one side of the plate out-of-phase from the patches on the second side. The instrumentation was located near the plate trailing edge to minimize the effect on the flow over the plate as well as near a theoretical clamped edge where bending moments are high. The accelerometer was later attached at the plate center.

4.2 A priori estimation of test conditions

Various parameters were estimated a priori to assess the conditions for the experiment. Among these were the boundary layer thickness, PZT output and the anticipated strain levels. A summary of these calculations for an aluminum semi-infinite strip with clamped-pinned edge conditions follows.

4.2.1 Boundary Layer Thickness

The boundary layer thickness is given by the following empirical formula [2]:

$$\frac{\delta}{x} = \frac{0.37}{(Re_x)^{1/5}} \quad (4.1)$$

where the Reynolds number is:

$$Re_x = \frac{\rho_0 U x}{\mu}, \quad (4.2)$$

x ($=0.508\text{m}$) is the distance from the leading edge of the fore airfoil to the center of the flexible plate, and μ ($=1.8 \times 10^{-5} \text{Ns/m}^2$) is the dynamic viscosity. The fluid density and flow speed are calculated using the compressibility tables for air and assuming an ideal gas. At $M=0.6$, when the static pressure is 14.7 psi and the stagnation temperature is 50°F, then the fluid density, ρ_0 , is 1.34kg/m^3 and the flow speed, U , is 195m/s . These parameters result in $Re_x=7.37 \times 10^6$, giving a boundary layer thickness, δ , of 0.00794m . The boundary layer thickness to plate chord ratio, δ/a , is 0.0794 . Since this ratio is less than 0.1 then the boundary layer affects on acoustic radiation damping may be neglected. If this ratio had been much greater than 0.1, then the boundary layer would need to be included in the analysis.

4.2.2 PZT excitation

The PZT excitation may be approximated using the following analysis for a semi-infinite strip, see ref. [6]. The boundary conditions assumed in ref. [6] have been modified to accommodate pinned-clamped conditions. Assuming harmonic motion, the isotropic semi-infinite equation of motion is:

$$D \frac{d^4 W}{dx^4} - \rho h \omega^2 W = \frac{d^2 M_x}{dx^2}, \quad (4.3)$$

where the moment induced by a PZT pair excited for bending motion is given by:

$$M_x = c_1 \epsilon_{pe} [u(x - a_0) - u(x - a_1)] W_{pe} / W_b. \quad (4.4)$$

The PZT parameters are: $c_1 = -\frac{E_b}{3} \left(\frac{2P}{1-P} \right) \frac{h^2}{4}$, $\epsilon_{pe} = \frac{d_{31}V}{t}$ and $P = \frac{-E_{pe}}{E_b} \left[\frac{3}{2} h t (h + t) / \left\{ 2 \left[(h/8)^3 + t^3 \right] + \frac{3}{2} h t^2 \right\} \right]$. E_{pe} and E_b are the PZT and plate bending stiffnesses, respectively, h is the plate thickness, t is the PZT thickness, d_{31} is the PZT charge constant, and V is the input voltage.

Eq. (4.3) is solved for the plate displacement by assuming a single mode expansion of W as given by Eq. (2.12) and applying Galerkins' method as given by Eq. (2.15). Substituting the beam function for a clamped-pinned plate (i.e., $W_n(x) = \cosh(\beta_n x) - \cos(\beta_n x) - \alpha_n [\sinh(\beta_n x) - \sin(\beta_n x)]$) into the modal expansion and solving for the plate modal amplitude, then:

$$|A_n| = c_1 \epsilon_{pe} \frac{W_{pe}}{W_b} \frac{F_0 - F_1}{\rho h a (\omega_n^2 - \omega^2 (1 + j 2 \zeta_n))}, \quad (4.6)$$

where $F_0 = \beta_n [\sinh(\beta_n a_0) + \sin(\beta_n a_0) - \alpha_n (\cosh(\beta_n a_0) - \cos(\beta_n a_0))]$ and $F_1 = \beta_n [\sinh(\beta_n a_1) + \sin(\beta_n a_1) - \alpha_n (\cosh(\beta_n a_1) - \cos(\beta_n a_1))]$. Utilizing the material properties given in Table 2.1 and the plate and piezo dimensions given in Figure 4.8, then the magnitude at the first mode is $A_1 = 1.75 \times 10^{-4}$ using three PZT pairs. This estimation is based on a maximum PZT input voltage of 80 volts with a charge constant of $d_{31} = 150 \times 10^{-12}$ m/V. The equivalent viscous damping, ζ_1 , is assumed to be 0.01. Since, the plate displacement to thickness ratio, $A_1/h = 0.175$, is less than 1, then the plate is vibrating in the linear range.

4.2.3 Flow induced vibrations

Although the estimated mean flow boundary layer characteristics should not significantly affect the acoustic radiation damping, the boundary layer pressure fluctuations can cause plate vibrations. These vibrations levels were estimated here to make sure that the PZT patches could drive the plate to response levels at least an order of magnitude greater than the forced response due to the boundary layer. The boundary layer pressure fluctuations on the plate were assumed to be fully correlated in space which results in an overestimation of response. The pressure spectral density is [17]:

$$\Phi^2(\omega) = \frac{p_{rms}^2}{\omega_0 \left[1 + (\omega/\omega_0)^2 \right]^{3/2}} \quad (4.7)$$

where

$$\omega_0 = \frac{8U}{\delta},$$

$$p_{rms} = \frac{0.006q}{1 + 0.14M^2},$$

and

$$q = \frac{1}{2}\rho_0 U^2.$$

Using the flow conditions calculated in section 4.2.1, then the modal magnitude for a single mode approximation is given by:

$$A_n = \frac{\sqrt{\Phi(\omega)\omega_n\zeta_n\pi} \left\{ \frac{1}{\beta_n} \left[(-1)^{n+1} \sqrt{\alpha_n^2 + 1} - \sqrt{\alpha_n^2 - 1} + 2\alpha_n \right] \right\}}{\rho h a \omega_n^2 2\zeta_n}. \quad (4.8)$$

Evaluating Eq. (4.8) for the first mode at its resonance frequency, then $A_1|_{\omega=\omega_1} = 2.44 \times 10^{-6} \text{m}$ for $\zeta_I=0.01$. This response is much less than that estimated due to the PZT excitation ($A_I=1.75 \times 10^{-4} \text{m}$) calculated in section 4.2.2. Thus the PZTs should drive the plate above the boundary layer ‘noise’.

4.3 Ground vibration tests

Extensive no-flow ground vibration tests were done prior to testing the elastic plate with flow. These test results are summarized in the following sections. Two plates were tested during the ground vibration test phase.

4.3.1 Test Plate 1

The first test plate provided much information concerning repeatability and modal frequencies, mode shapes and structural damping values. Tests were conducted with impact excitation, acoustic excitation as well as with PZT excitation.

A sample transfer function between the impact hammer (PCB No. 086C80) and an accelerometer (Endevco #2250–A10, 0.4gm) is given in Figure 4.9. The modal peaks are sharp and distinct. The scatter of modal frequency and damping values acquired over a 2 month period during which time the plate was removed and reinstalled in the model many times are plotted in Figure 4.10 along with analytical clamped-free-pinned-free (CFPF) and pinned-free-pinned-free (CFCF) values [4]. The data were acquired using both impact hammer and sine-dwell acoustic speaker excitation. The response was measured with 1 or 2 accelerometers attached to the plate at various locations. The damping was calculated from a bode plot within the spectrum analyzer (GenRad 2515) or from the transfer function by using the

half-power technique. The results show very little change in modal frequency, but a larger scatter in the damping values for each mode. Note that the damping is equal to or less than 0.021 for all modes. Also modes 2,1 and higher are closely spaced in frequency or the mode shapes more difficult to identify. For these reasons only the first three modes were considered in future tests. Since the 2nd and 3rd modes are not included in the semi-infinite strip analysis, then only the first mode experimental flow results will be compared to analysis.

Unfortunately, this plate was damaged such that the fundamental frequency peak was no longer sharp and distinct. Thus a new test plate was constructed and used in the remaining tests.

4.3.2 Test Plate 2

Test Plate 2 was placed in the model and the modal frequencies and damping values calculated from an impact hammer test with the response measured by an accelerometer. The results are also plotted in Figure 4.10. Plate 1 and 2 modal frequencies agree very well. The damping value for the Plate 2 first mode lies well within the scatter of the Plate 1 data, while the 2nd and 3rd mode damping values are less than those measured for Plate 1.

Bare (described in the preceding paragraph), instrumented and in-situ case modal frequencies and damping results are presented in Tables 4.1 and 4.2, respectively. The instrumented and in-situ results have the PZT patches and strain gages bonded to the plate. The instrumented results were acquired with the plate installed in the model, but the model was not in the flow test chamber. The in-situ results were acquired with the model installed in the flow test chamber. The plate was removed

from the model between the bare and instrumented cases to allow for the installation of the PZT patches and strain gages. However, the plate remained in the model between the instrumented and in-situ cases.

The analytical natural frequencies for plates with ideal CFPF and PFPF boundaries have been included with the bare, instrumented and in-situ measured values in Table 4.1. Note that based on frequencies alone, the bare case is closer to CFPF while the instrumented plate is closer to PFPF. The instrumented plate frequencies are lower in part due to the added PZT masses. The PZTs were estimated to decrease the modal frequency of the first mode about 10%, while the accelerometer mass would reduce the fundamental modal frequency less than 2%. This mass partially accounts for the decreases in frequency between the bare and instrumented cases. In addition, the non-uniform distribution of the mass will also affect the modal response. These mass changes would most affect the lower modes, particularly the first mode.

Most of the damping results presented in Table 4.2 (see also Figure 4.11) were acquired using an impact hammer or sine-dwell acoustic speaker test with accelerometers or strain gages measuring the response. For these cases, the damping was calculated from the bode plot or by the half-power technique (\square in Figure 4.11). A log-decrement technique [18] using the PZT patches or a speaker as excitation was used for the damping calculations in column 4 or \diamond in Figure 4.11 (with the raw unscaled data in Appendix B). These were the only decay measurements to have a distinct decay. These values in column 4 are significantly larger than those in columns 2, 3 and 5. A beating pattern was evident in the decay data. The last three values in column 4 were acquired simultaneously and agree to within 12% for the

two strain gages and the accelerometer. The decay calculation with a speaker input and accelerometer output was not as clean.

The PZT excited decay responses may be significantly influenced by the PZT patches. PZT patches act like capacitive devices that may thus continue to affect the plate vibrations (e.g. additional damping) after the signal to them has been stopped. The PZT effect on the decay has not been quantified. Although the PZT patches might affect absolute damping values, the change in damping may still be correct, depending on the magnitude of this effect. Sine-dwell PZT with strain gage response results were not calculated due to the interaction between the PZTs and the strain gages. The strain gages can be affected by the 100 volts supplied to each PZT patch. This was evident in the sine-dwell PZT test where the strain gages showed essentially a flat response near the modal frequencies. In addition, the strain gage should be several characteristic lengths from the PZT patches to eliminate the effect of the PZT nearfield on the strain gage response. The in-situ damping values acquired with the impact hammer agree with the previous impact tests. However the data acquired using the sine-dwell PZT technique with accelerometer response are significantly higher as was evident with the decay measurements. The in-situ modal data was acquired following the flow tests to be described in the next section. In general, the results from the PZT excitation are not thought to be reliable. In future tests, the PZT patches and strain gages should be well separated on the test plate.

4.4 Flow Tests

Following the ground vibration tests outside the flow test chamber, the response of the plate with flow was measured. The static pressure differential across the fore and aft airfoils was monitored during the tests with Datametrix (no. 570D) pressure transducers. The variation with Mach number is plotted in Figure 4.12 with the accelerometer installed. The pressure differentials were also measured at $M=0.6$ without the accelerometer installed. These results are denoted as a 'square' for the fore airfoil and a 'plus' for the aft airfoil. The solid line is the minimum pressure differential that would cause buckling, and thus changing the plate stiffness [27]. The fore and aft airfoil pressure differentials lie well below this line. The pressure differential increases with Mach number up to $M=0.7$ as expected. The decrease at $M=0.8$ has not been explained. The accelerometer lead was blown off during the $M=0.7$ run and was gone during the entire $M=0.8$ run, which may partially explain this trend. The accelerometer itself remained attached to the plate. Since Δp is not exactly equal to 0, then the airfoils are not perfectly aligned with the flow. The difference in Δp between the fore and aft airfoils could be caused by a misalignment between the two airfoils. In addition, the instrumentation on the plate, particularly the accelerometer, could cause a static pressure difference. An accelerometer was bonded to one side of the plate once the strain gage outputs were questioned. The accelerometer will significantly affect the flow, as is evident in the strain gage response with and without the accelerometer at $M=0.6$, see Figure 4.13. However, these accelerometer measurements did provide significant insight and confidence in the results.

The pressure, temperature, and humidity in the chamber were monitored during the test runs. The chamber pressure remained relatively constant (± 0.1 psi) over the three weeks in which flow data was acquired. The chamber temperature decreased as much as 10°F during the course of a single blow down. If the plate were firmly fixed (no expansion or contraction allowed) then this change in temperature could cause the plate to buckle and become stiffer. The additional stiffness would cause the modal frequencies to increase. However, the fundamental frequency was nearly constant during a single blow-down which implies that the plate properties were not changing. The repeatability of the accelerometer data at $M=0.6$ is shown in Figure 4.14. Between these two data acquisitions the accelerometer had been removed and reinstalled. The relative humidity decreased from $30\% \sim 40\%$ to nearly 5% . The effect of relative humidity is thought to be negligible.

The PZT patches were not sufficient to excite the plate greater than that induced by the flow. This was evident in the sine-dwell PZT tests with the response measured by an accelerometer. The peak at the PZT driving frequency was not discernible above the flow 'noise'. This might have been overcome if a much longer data acquisition time was available so that the random excitation components due to the flow could be eliminated by appropriate signal processing.

For the data cases presented with flow, the flow alone excited the plate. In addition, the accelerometer remained attached to the plate center. The flow excitation pressure field could not be measured with the existing test model. Thus, the fluid to structure transfer function was assumed to have the same shape as a function of frequency as the square root of the response power spectral density (PSD). This

assumes that the flow excitation is nearly uniform as a function of frequency near the modal frequencies. The modal frequency was the peak of the PSD while the half-power points required for the half-power technique were located at one-half the maximum PSD amplitude.

Sample PSD responses near the first modal frequency for the strain gage and accelerometer are shown in Figure 4.15. The response at $M=0.4$ is small when compared to the higher Mach numbers. However, a peak exists at the first mode. Note that although the frequency increases with increasing Mach number, the response amplitude decreases and broadens for $M=0.5 - 0.7$. This amplitude trend is expected since as the Mach number increases, then the damping increases resulting in a broadening of the peaks. If the excitation is assumed to increase with increasing Mach number, then the decrease in peak modal response also indicates an increased damping.

The modal frequency and damping results are shown in Figures 4.16–4.18 for modes 1,1 and 1,2. Data for both the accelerometer and a strain gage have been included. As for the analytical results, the frequencies are presented as ratios, with the frequency at $M=0$ (240 Hz) as reference. The analytical results for clamped-pinned and pinned-pinned semi-infinite strips and for a fully clamped plate where $a=0.1\text{m}$, $b=0.15\text{m}$, and $h=0.001\text{m}$ have been included. The clamped plate damping values were taken from the design chart Figure 3.20, since the flow would have a small effect on the clamped plate fundamental frequency (see Figure 3.8a). As previously stated, only the first mode is compared to analysis. The clamped-pinned and pinned-pinned curves provide a lower frequency bound and upper damping bound while the fully

clamped provides a lower damping bound. As expected from earlier analytical results, the clamped-pinned and pinned-pinned cases have nearly the same damping ratio but the pinned-pinned frequency ratio is significantly lower than the clamped-pinned results. The measured first mode frequency ratios do not continue to decrease as Mach number increases as expected from theory. In fact, there is little change with Mach number or a slight increase. However, the results at $M=0.4$ show fair agreement between the experimental and numerical values.

Looking at the damping ratio and the change in damping ratio relative to the damping at $M=0$, in Figures 4.16b and 4.17, respectively, the analytical values are for acoustic radiation damping only, while the measured values include all damping components. However, the change in damping ratio as a function of Mach number, see Figure 4.17, should only result in the acoustic radiation damping for both the experimental and analytical cases. Note that the analytical acoustic radiation damping value at $M=0$ (0.015) lies below the measured value (0.018). The damping values for $M=0.5$ and higher lie below the analytical clamped plate values. Two damping values for the accelerometer at $M=0.6$ corresponding to the two runs in Figure 4.14 are included. This indicates the repeatability of the damping values is good. In addition, the damping for the strain gage at $M=0.6$ when the accelerometer was not on the plate is indicated by the 'x'. The reason for the disagreement between analysis and experiment has not been determined.

The second mode modal frequency and damping values are included in Figure 4.18. Since the second mode is not theoretically modeled, no comparison with theory is available. The occurrence of the second mode is not possible analytically for a

uniform flow due to symmetry . In addition, the effect of the horizontal baffles on the plate response was not modelled. Since, this mode is apparent in the experimental data, then either the plate is non-uniformly clamped in the fixture or else the flow is not uniform across the plate span.

The experimental results show good repeatability for modal frequencies with fair repeatability for modal damping ratios. Part of the scatter in damping values may be due to measurement techniques. In addition, the measured damping values have traditionally been less precise or repeatable than the frequencies. However, the test results with flow show good repeatability.

The theory and experiment are definitely not in close agreement, especially for damping. The following paragraph presents some possible reasons for these differences.

The flow core radius at the plate is about the same as the plate chord. Thus a mean flow discontinuity exists near the plate although the plate itself is well within the flow core. The flow discontinuity can cause reflection of acoustic waves back to the plate. The plate is assumed in the analysis to create flow disturbances that radiate to infinity through a uniform mean flow field. This discontinuity in the flow could be significant and it might be accounted for in the analysis by using a fluid model that varies with distance from the plate. An alternative approach to improving the analytical/experimental agreement is to perform the test in a low turbulence wind tunnel. This would more accurately replicate the analytical model presented here. In addition, better modelling or understanding of the effects of PZT material would improve the experimental design.

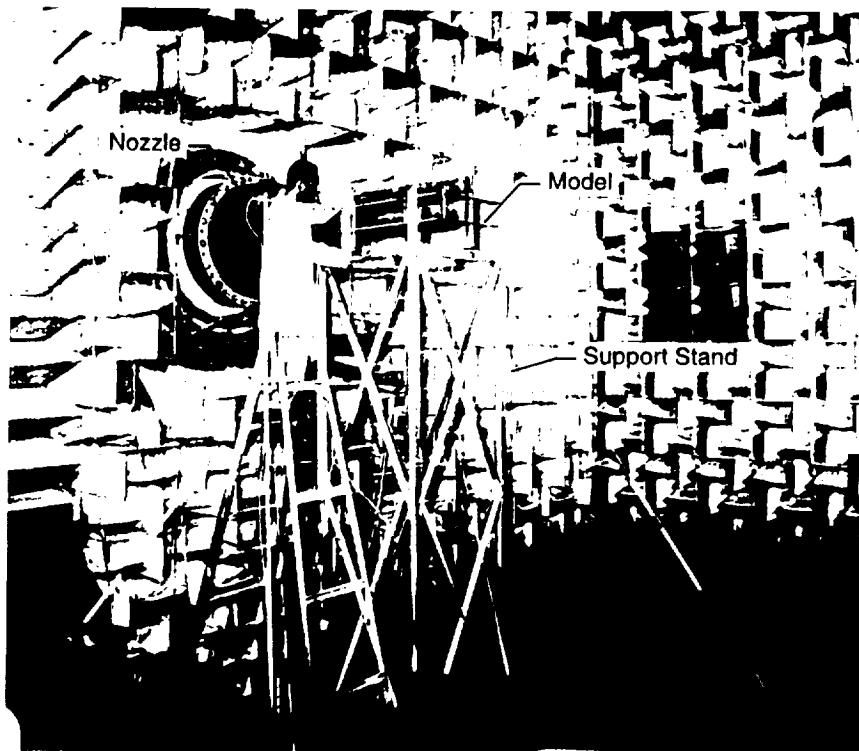
Table 4.1 Plate modal frequencies

Mode	Analytical frequencies (Hz)		Measured frequencies(Hz)		
	CFPF	PFPF	Bare	Instrumented	In-situ
1,1	378(1.00)	204(1.00)	315(1.00)	246(1.00)	240(1.00)
1,2	440(1.17)	267(1.31)	372(1.18)	355(1.44)	295(1.23)
1,3	657(1.74)	522(2.56)	562(1.78)	538(2.18)	475(1.98)
1,4	1066(2.82)	849(4.16)	—	—	—
2,1	1229(3.25)	818(4.03)	930(2.95)	923(3.87)	—
2,2	1304(3.45)	898(4.40)	962(3.45)	—	—

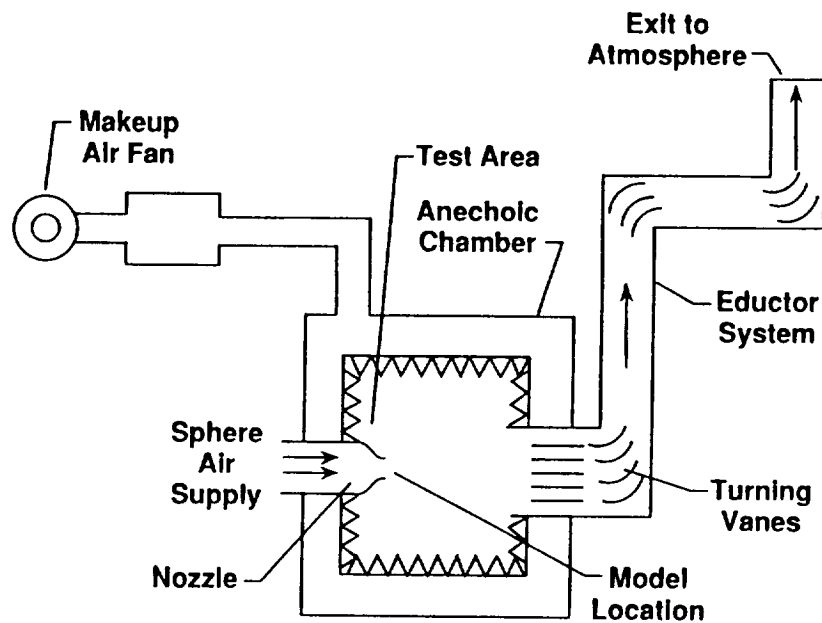
Table 4.2 No-flow measured damping values

Mode	Bare ¹	Instrumented ²	Instrumented ³	Instrumented ⁴	In-situ ⁵
1,1	.0146(.016)	.0256 (.0398)	.0313-.0397	.058	.018 (.085)
1,2	.0056	.0206 (.0272)	—	.0963	— (.0574)
1,3	.0047	.0158 (.0225)	—	.0798 ^a .0531 ^b .0532 ^c .0473 ^d	.0248 (—)

Superscript	Force method	Response type
1	impact hammer bode (speaker sine-dwell 1/2-power)	accelerometer (accelerometer)
2	impact hammer bode (impact hammer 1/2-power)	accelerometer accelerometer
3	speaker sine-dwell 1/2-power	strain gage
4	PZT decay	accelerometer
a	speaker decay	accelerometer
b	PZT decay	strain gage
c	PZT decay	strain gage
d	PZT decay	accelerometer
5	impulse hammer 1/2-power (PZT sine dwell 1/2-power)	accelerometer accelerometer



(a)



(b)

Figure 4.1. (a) Photograph and (b) schematic of Quiet Flow Facility.

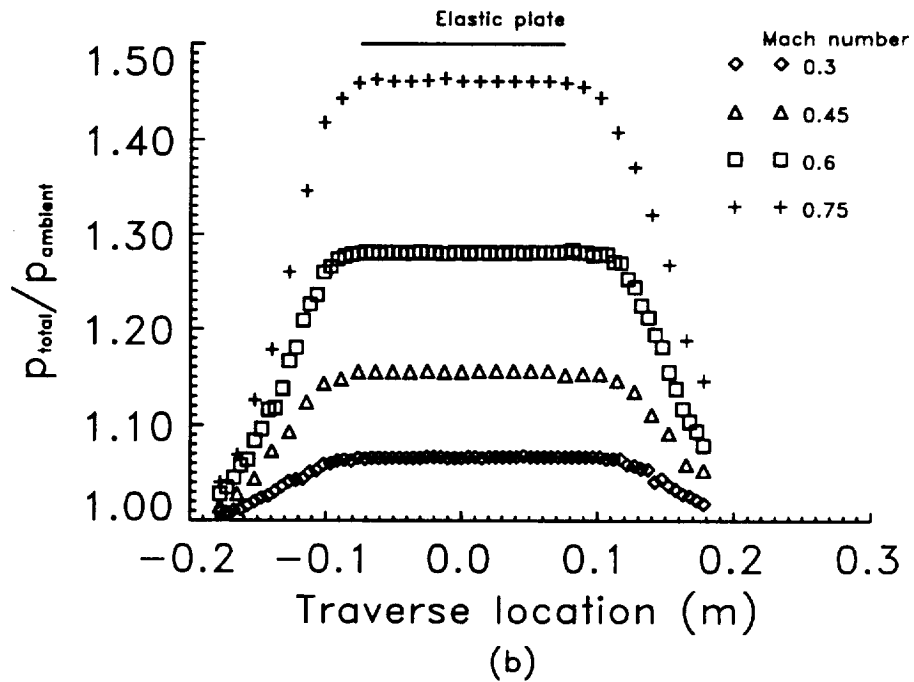
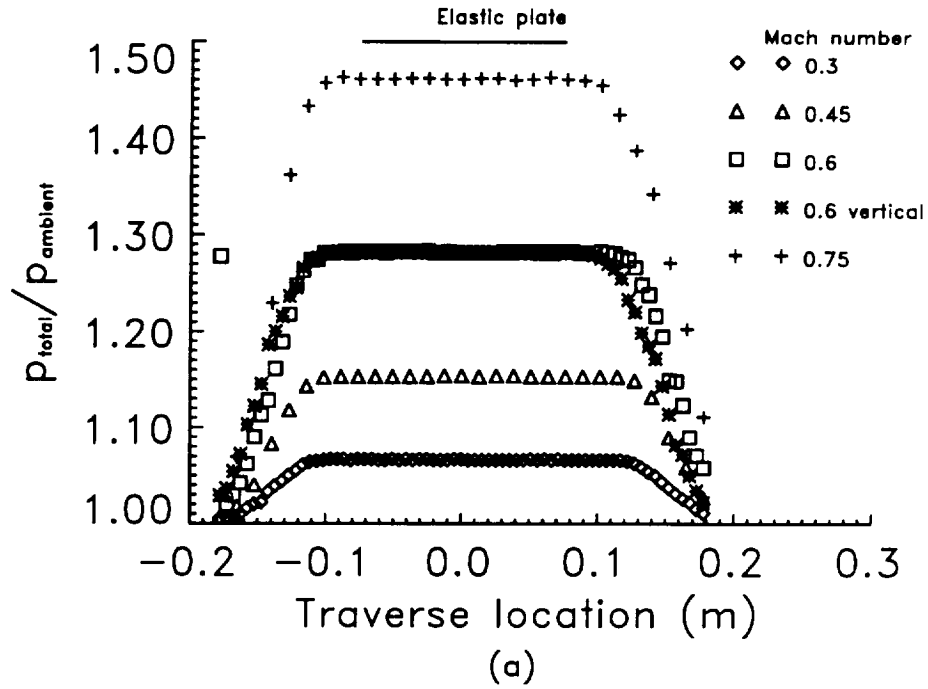


Figure 4.2. Variation of total pressure ratio at (a) 0.508m and (b) 0.762m from nozzle.

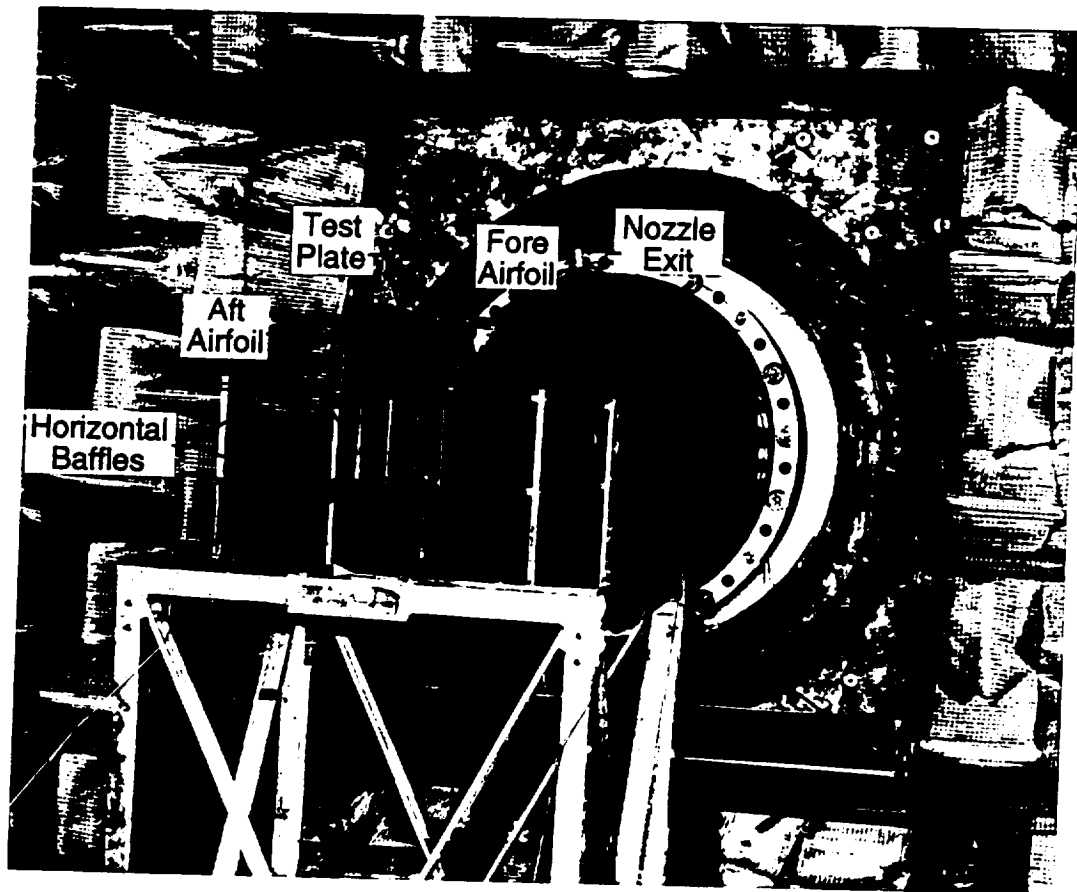
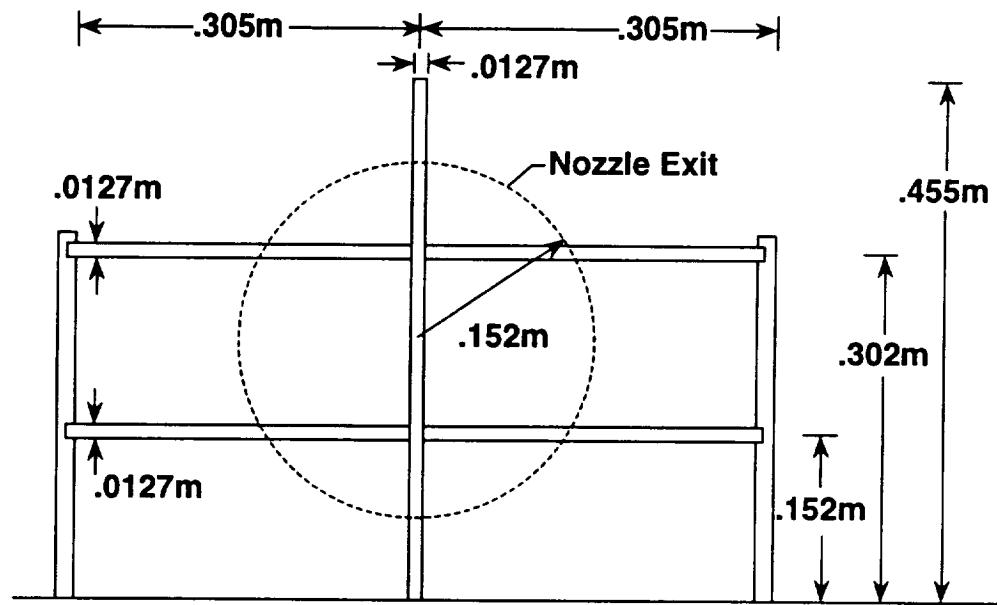
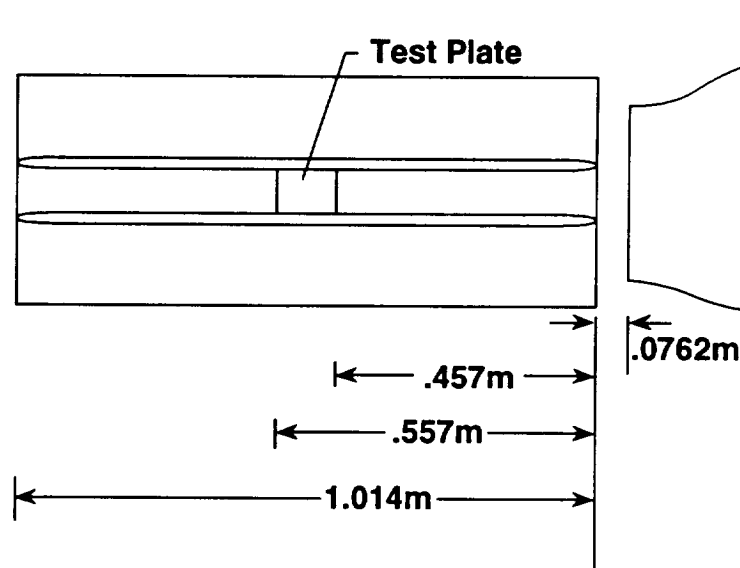


Figure 4.3. Photograph of model in-situ.



(a) Front View



(b) Side View

Figure 4.4. Sketch of model.

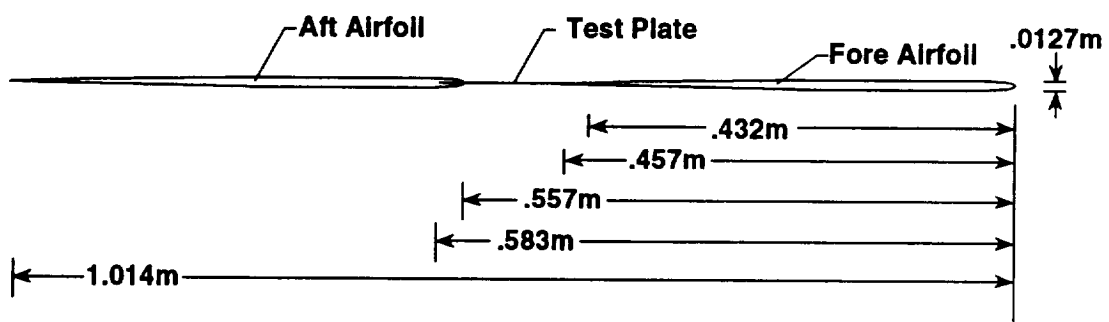
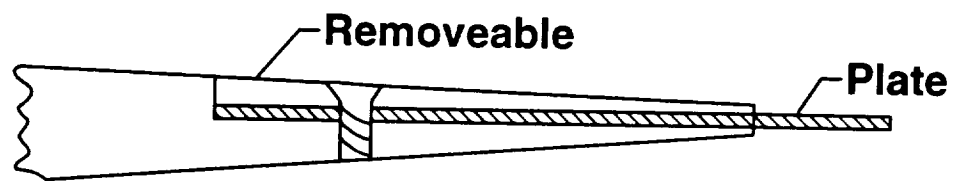
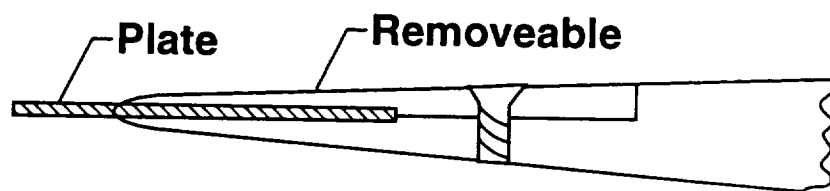


Figure 4.5. Drawing of test plate in fore and aft airfoils.



(a)



(b)

Figure 4.6. Detailed drawing of clamping mechanism: (a) fore airfoil; and (b) aft airfoil.

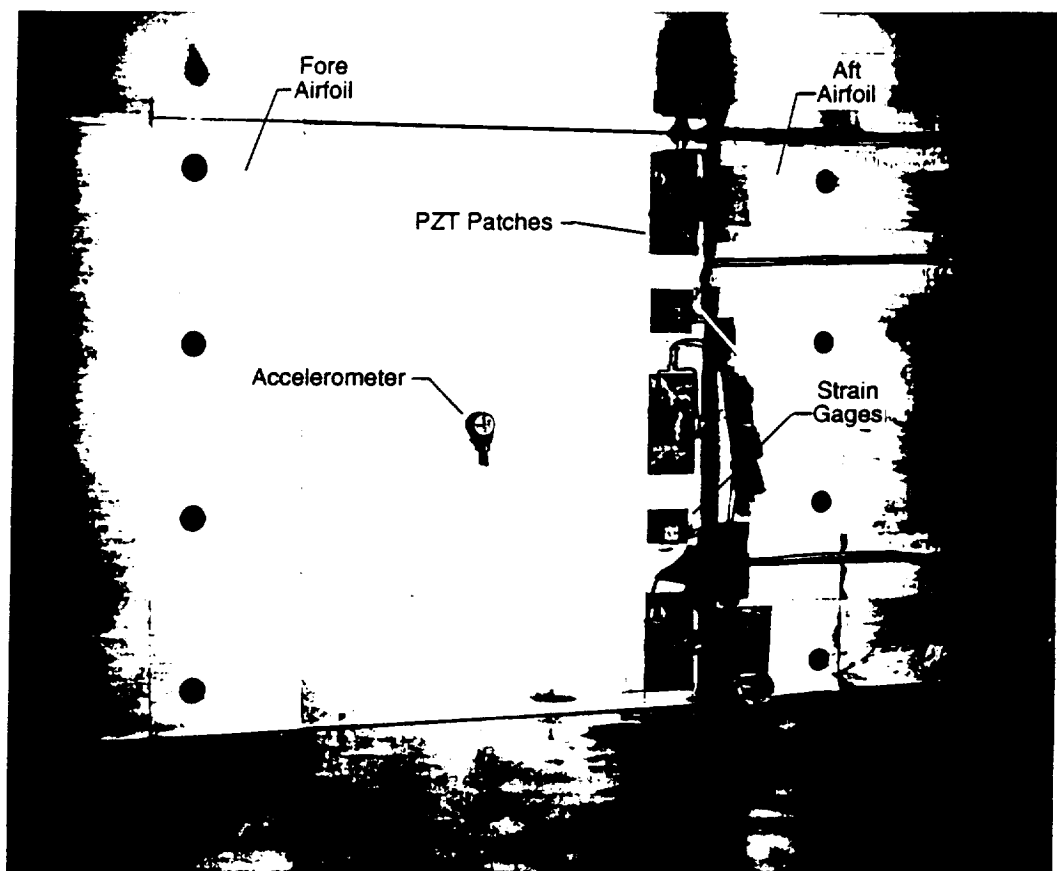


Figure 4.7. Photograph of plate in-situ.

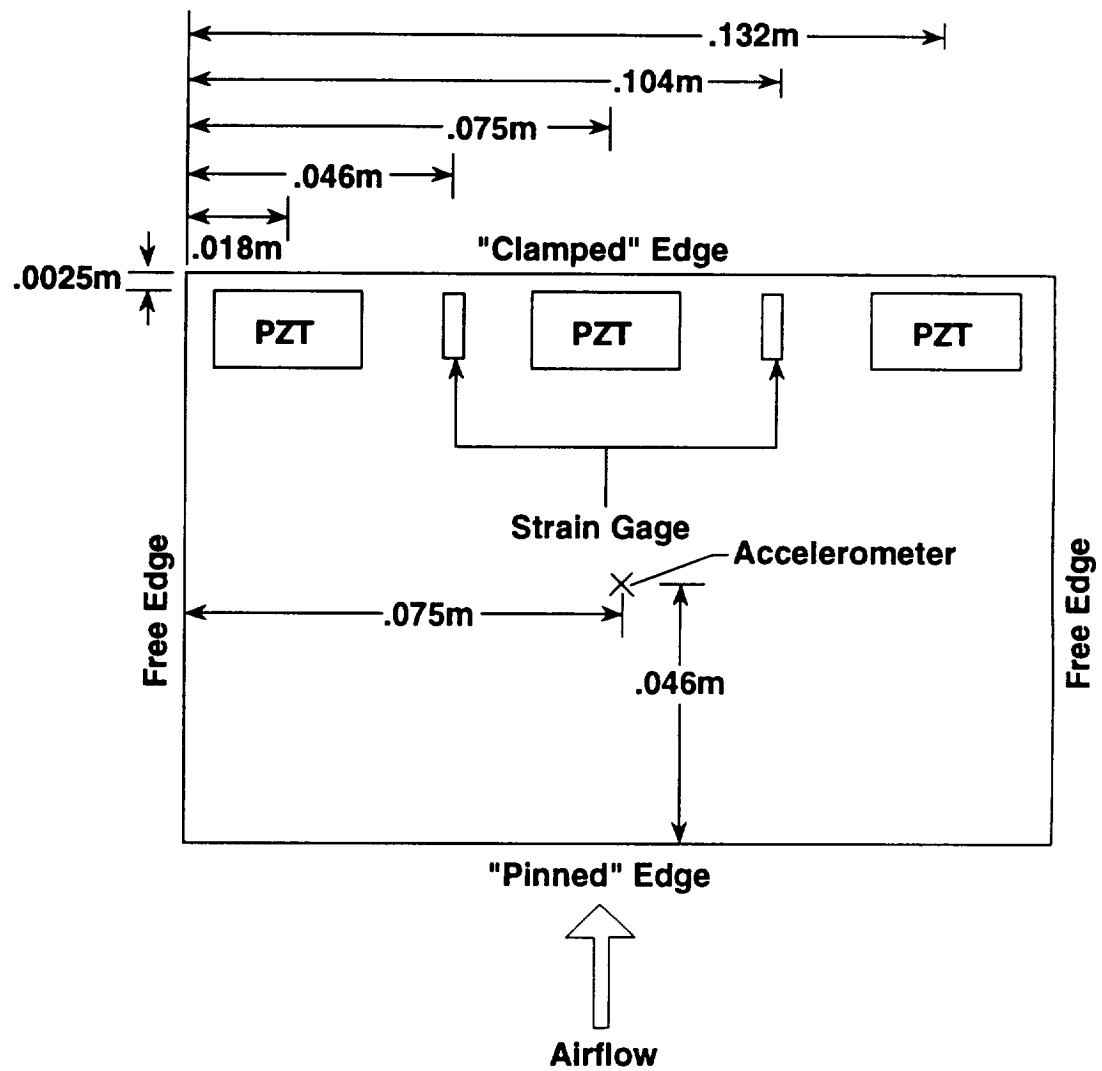


Figure 4.8. Transducer locations.

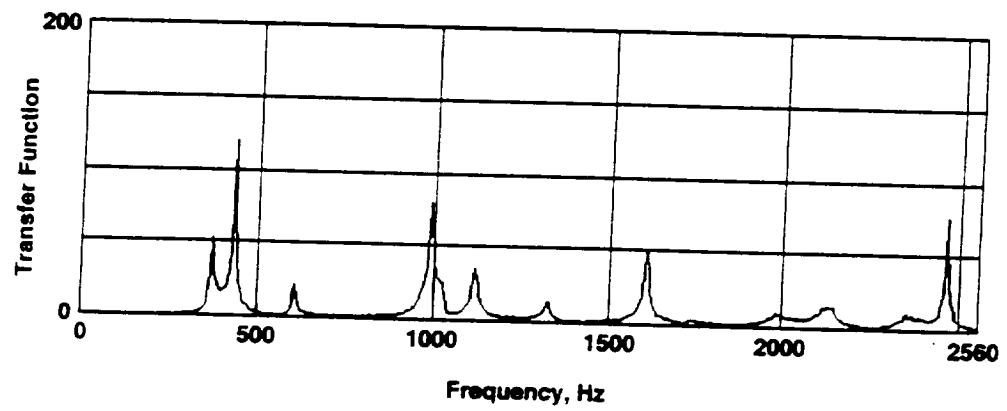


Figure 4.9. Sample transfer function for Plate 1 calculated from accelerometer response due an impact hammer excitation.

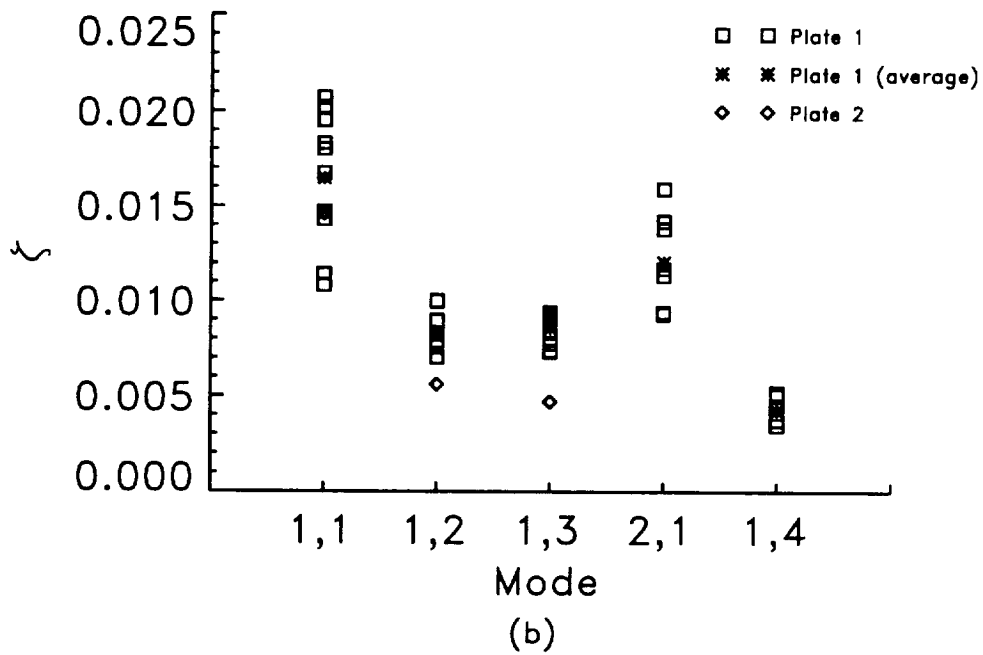
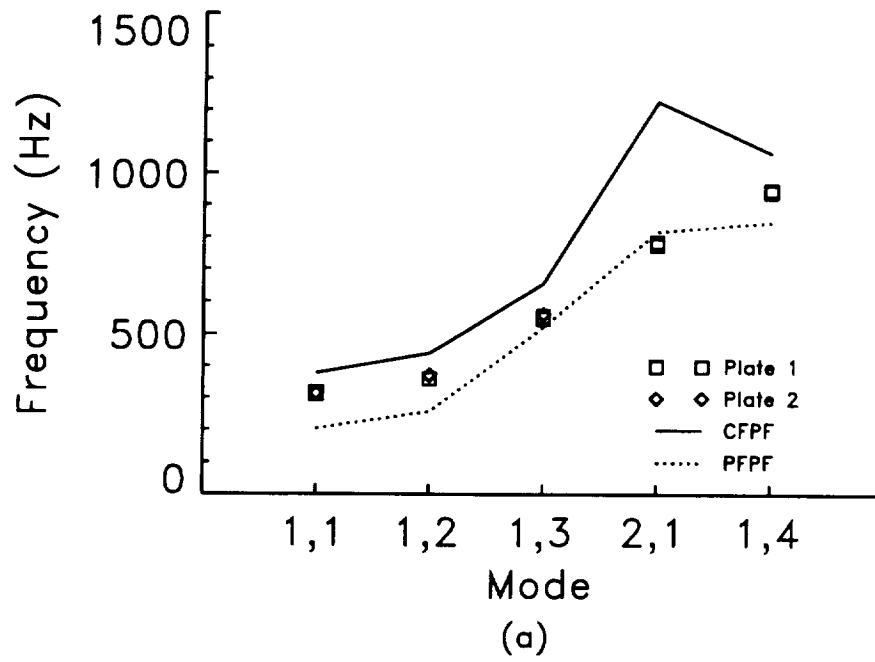


Figure 4.10. Scatter of (a) modal frequencies and (b) damping ratios for Test Plates 1 and 2 without PZTs or strain gages installed.

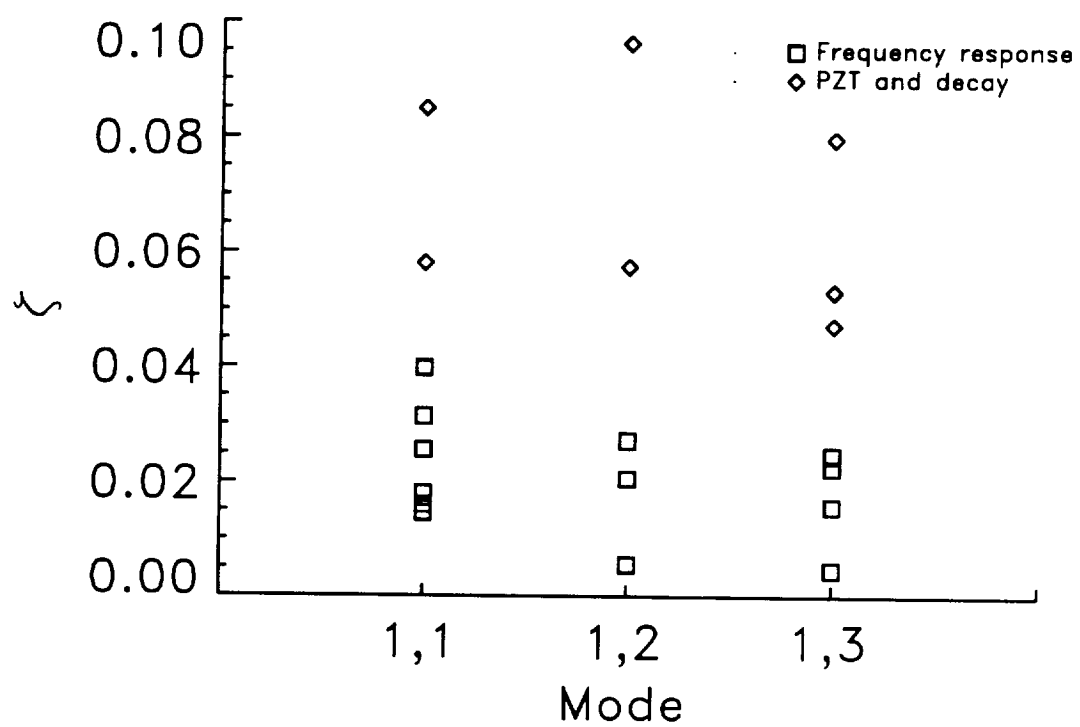


Figure 4.11. Scatter of Plate 2 no-flow damping ratios with PZTs and strain gages installed.

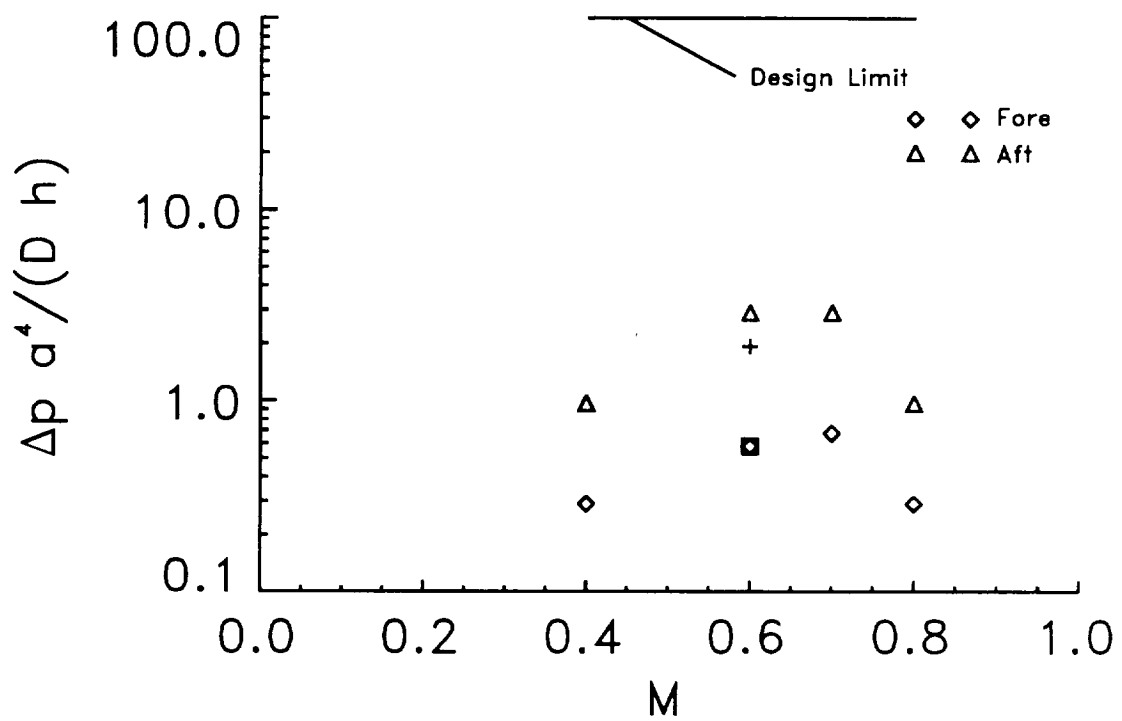


Figure 4.12. Variation of fore and aft airfoil pressure differential as a function of Mach number.

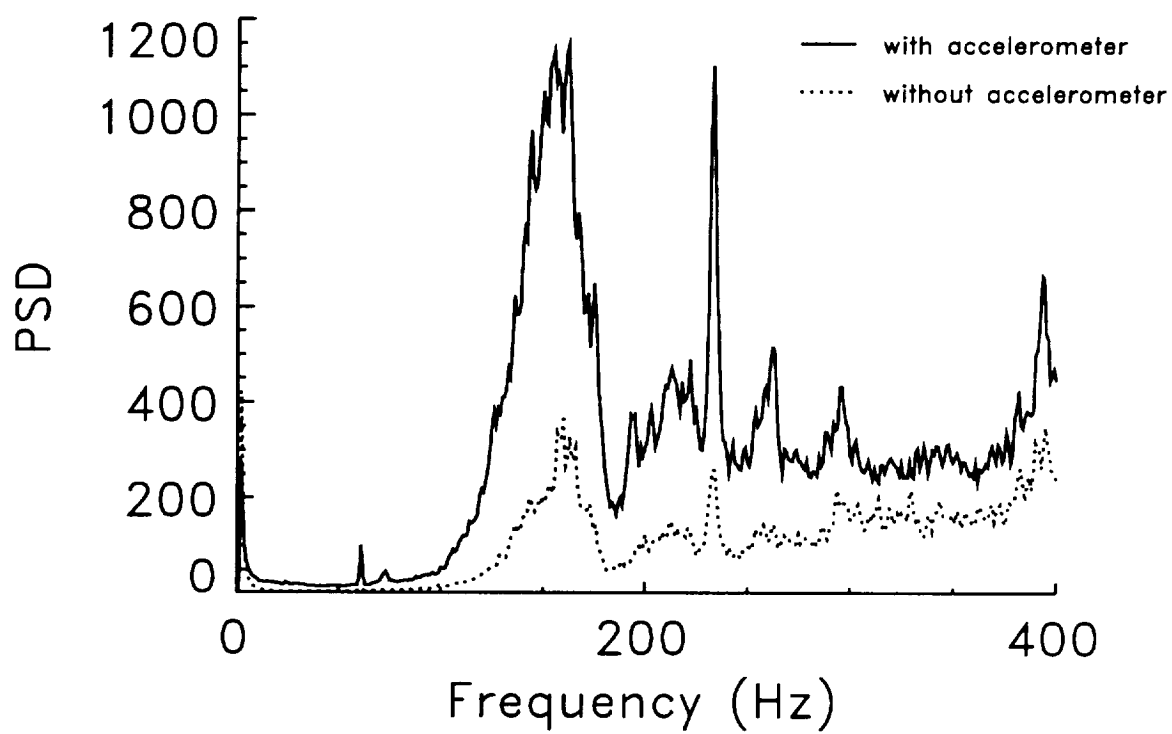


Figure 4.13. Power spectral density of strain gage at $M=0.6$ with and without the accelerometer installed.

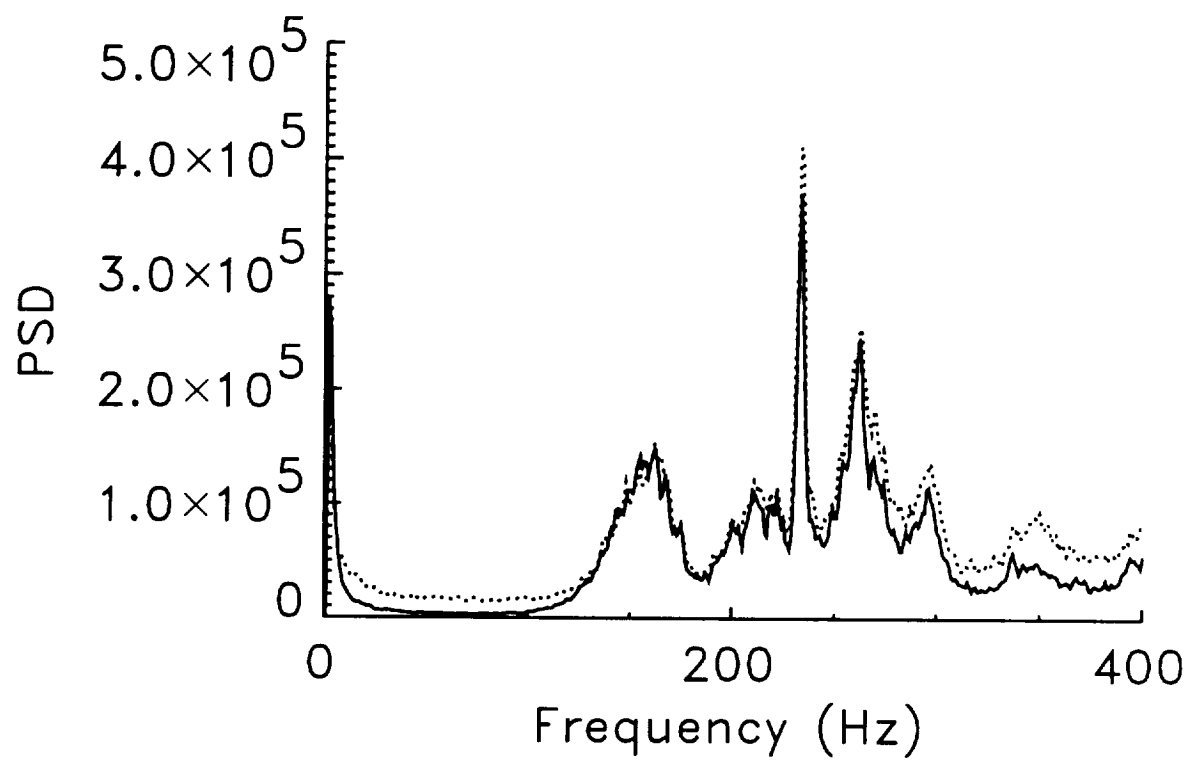


Figure 4.14. Repeatability of the accelerometer power spectral density at $M=0.6$.

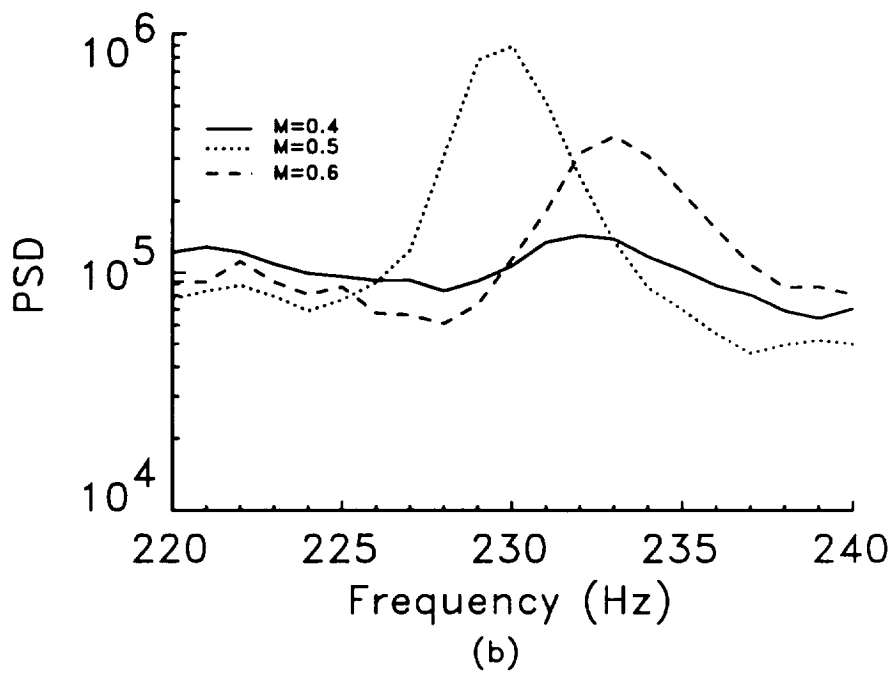
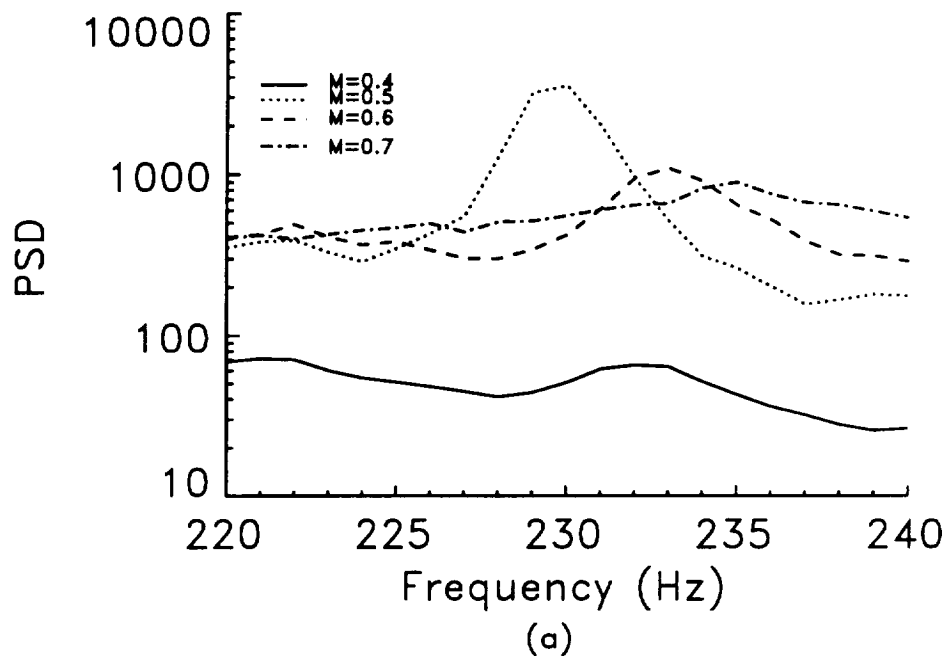


Figure 4.15. First mode power spectral density for (a) strain gage and (b) accelerometer.

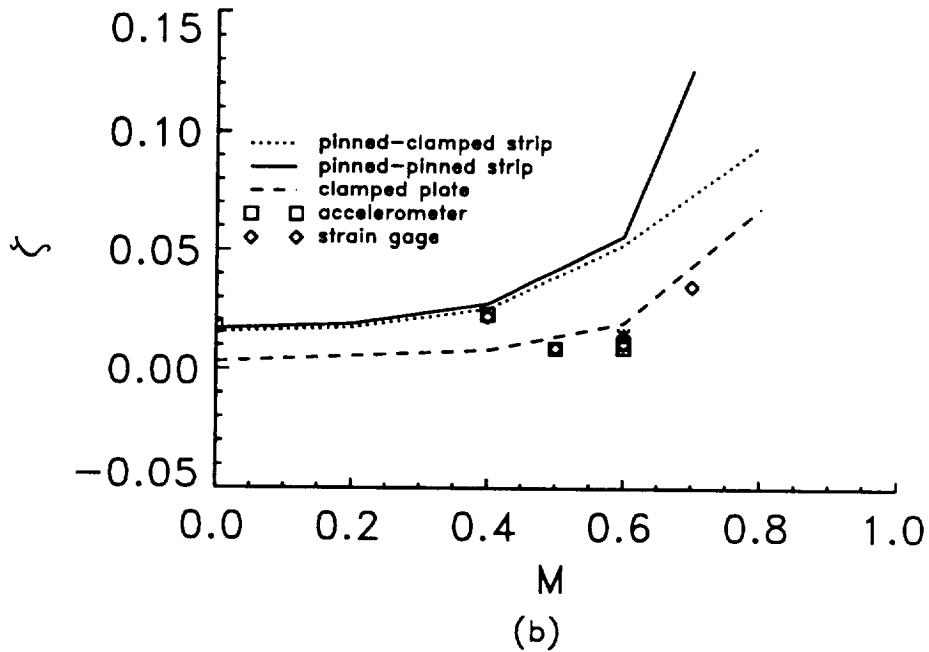
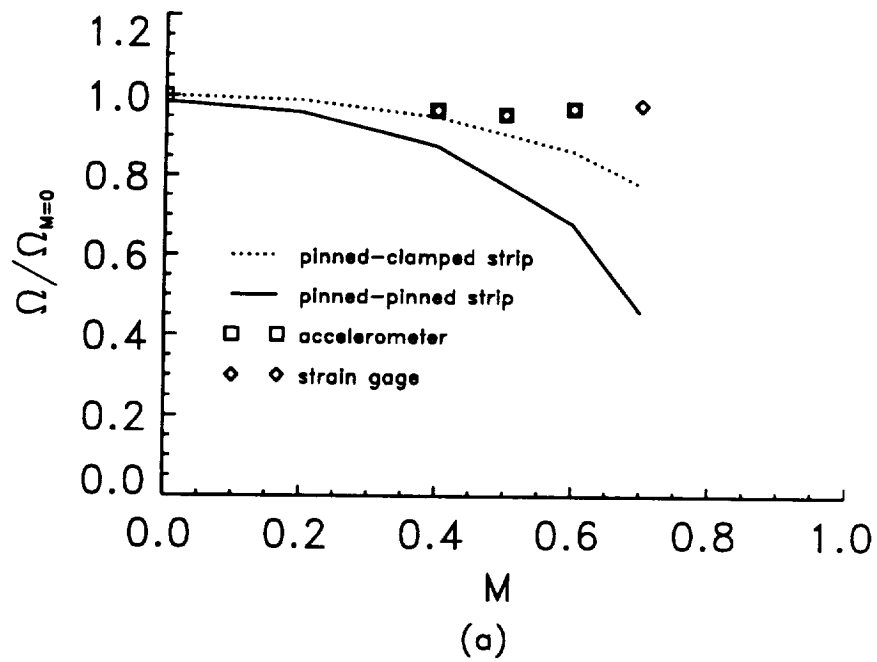


Figure 4.16. Variation of mode 1 (a) frequency ratio and (b) damping ratio as a function of Mach number for various analytical and experimental cases.

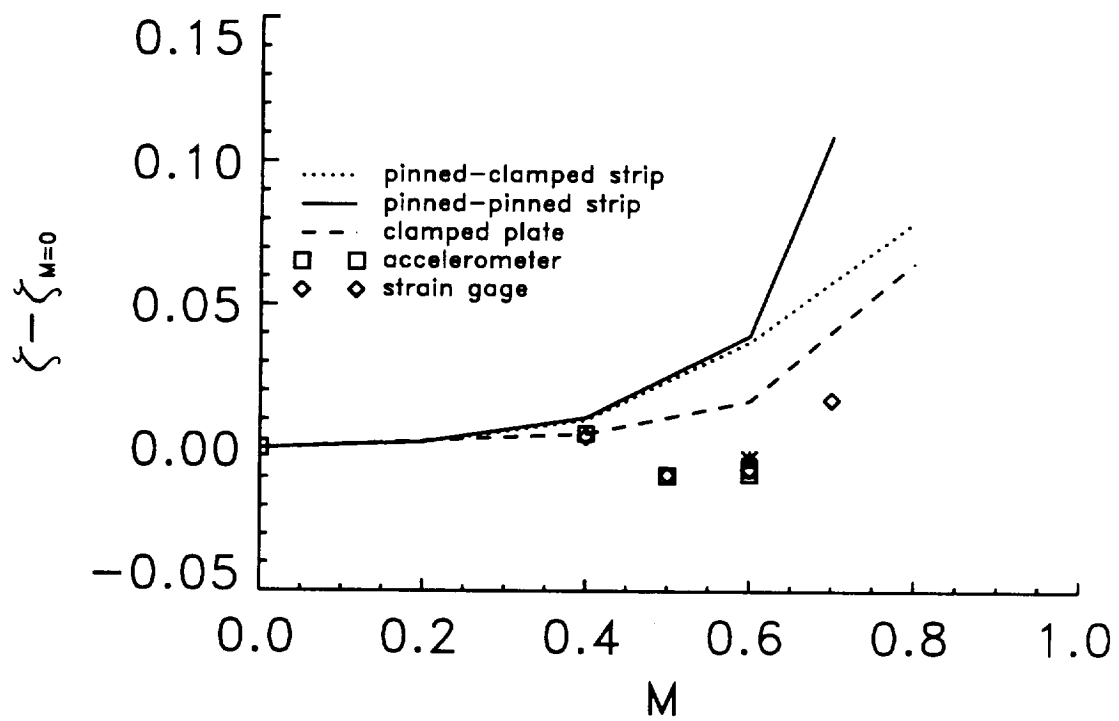


Figure 4.17. First mode damping ratio relative to the damping at Mach 0.

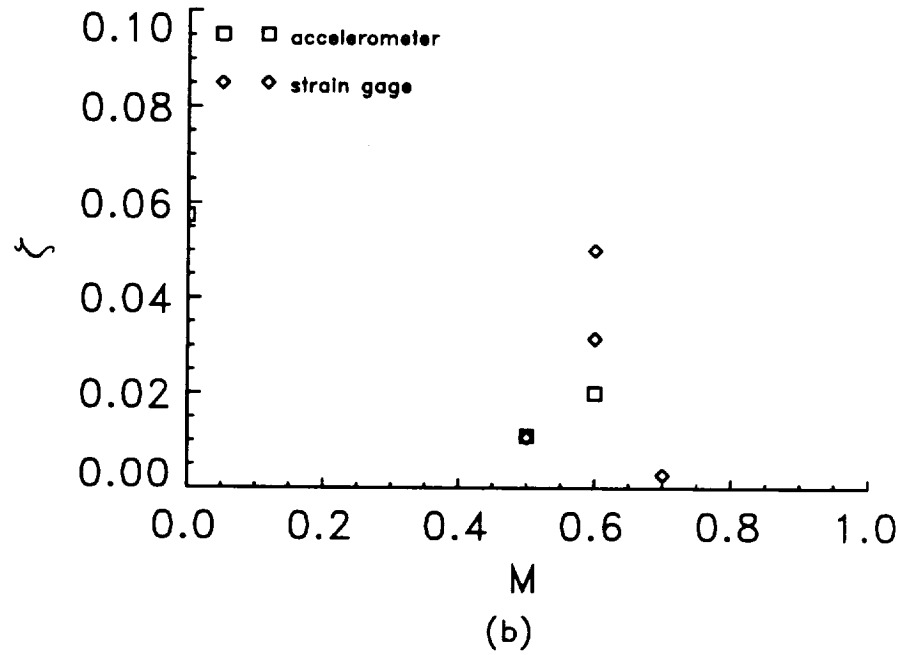
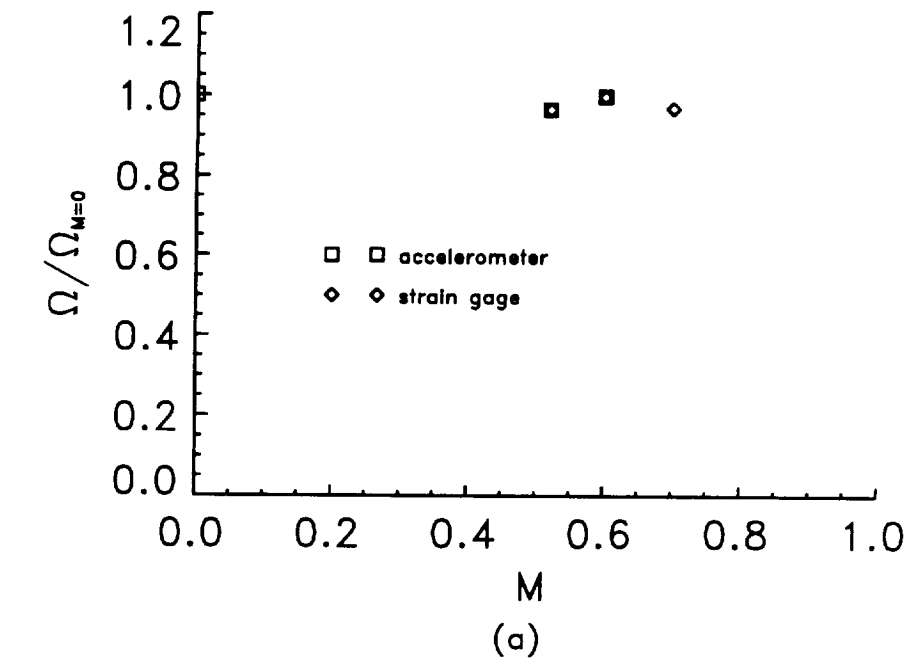


Figure 4.18. Variation of mode 2 (a) frequency ratio and (b) damping ratio as a function of Mach number for various analytical and experimental cases.

CHAPTER 5 CONCLUDING REMARKS

The primary objective of the dissertation was to evaluate systematically the acoustic radiation damping for comparison with typical values of structure damping. Analyses and numerical techniques to predict the acoustic radiation damping for isotropic and laminated composite finite plates and semi-infinite strips have been presented. The predictions are based on the classical linear differential equation for a flat plate or semi-infinite strip. The perturbation pressure derived from the linearized Bernoulli and continuity equations characterizes the fluid loading. Parameters varied in the analyses include Mach number, structural mode number, plate or strip dimensions, edge conditions, material properties and ply lay-up. In addition, the results were compared to various limiting cases and previously published results.

The perturbation approximation for small fluid to plate mass ratio gives an initial estimate of acoustic radiation damping with a minimum of computation. The perturbation method was based on a multimode approach; however, the resulting expression requires only a single mode computation. The approximation does not account for changes in the effective mass or stiffness. Thus when the flow significantly affects the modal frequency, the perturbation approximation results are not valid. In addition, the perturbation approximation results in large errors near plate divergence where there is a substantial loss of plate stiffness due to aeroelastic effects from the interaction of the elastic plate with the aerodynamic flow.

An alternative method for computing the change in modal frequency and acoustic damping due to the flow is to use the resonant response and half-power method.

However care must be used here as well, for example, in computing the fluid loading term. In fact, for large damping values the effective damping (C_1) and effective mass or stiffness (C_2) terms must be calculated at each frequency in order to calculate accurately the resonant peaks rather than using a simple linear relationship between the two half-power points.

The semi-infinite strip results showed that the chord length and plate thickness (and thus frequency) as well as Mach number significantly affect the acoustic radiation damping. The plate mass affects the acoustic radiation damping ratio, but has little effect on changing the modal frequency from the in-vacuo value since changing the plate mass does not change the plate stiffness. Changing the plate boundary condition can significantly affect the modal frequency, but has little effect on acoustic radiation damping up to the divergence Mach number of the least stiff plate. Generally, the higher modes have acoustic radiation damping ratios an order of magnitude less than the first mode. In addition, the fluid flow has much less effect on the modal frequencies of the higher modes. The first mode for clamped-clamped plates was found to be well approximated by a single product of beam functions.

Changing the aspect ratio can have a significant effect on the damping ratio. For the first mode, the effect of increasing Mach number increases the acoustic radiation damping up to where the curves collapse at high a/b to piston theory.

The acoustic radiation damping and modal frequencies for symmetrically laminated composite plates were found to depend strongly on ply lay-up, particularly the outside fiber direction. This dependence implies that the ply lay-up can be tailored to maximize the acoustic radiation damping while delaying or preventing divergence.

Additionally, the composite material acoustic radiation damping ratio is significantly greater than an 'equivalent' aluminum plate. This is true whether the equivalence is in terms of plate thickness or stiffness.

A set of universal curves was developed where the damping ratio normalized by the mass ratio was given as a linear function of a reduced frequency factor. These curves were valid for a constant aspect ratio and a Mach number. However, the plate material properties, area, and thickness could vary along each curve. If the plate was not near divergence, then the reduced frequency factor could be further approximated such that the effect of the fluid on the plate stiffness (an integral evaluation) was not required. Since most aircraft sidewall panels are not designed to operate near divergence, the simpler approximation may be useful in predicting acoustic radiation damping in aerospace applications.

Finally, the acoustic radiation damping may be equal to or greater than the assumed structural damping over a range of realistic panel sizes. Thus, for higher subsonic Mach numbers the acoustic radiation damping of the first mode can be the dominant damping source.

An experiment was designed and experimental modal frequency and damping values measured for comparison with the theory. PZT patches (piezo electric devices) were installed on the plate along with strain gages and an accelerometer. Unfortunately, the PZT patches interacted electrically and/or mechanically with the strain gage signals. In addition, the PZT patches were unable to drive the plate above the vibrations induced by the flow. For these reasons, the flow alone was used to excite the plate in the present experiments. The plate response was measured by

strain gages and accelerometers with the modal frequencies and damping calculated from the measured power spectral density. The repeatability of the flow data was good. The agreement between measured and theoretical values was at best fair with an erratic (compared with theory) experimental trend with higher Mach number.

Two general approaches are suggested to improve the experimental-theoretical correlation. Analytically, a more complex flow may be modeled which includes the variation in the mean flow speed due to the finite core radius. Experimentally, performing the test in a low turbulence wind tunnel would more accurately replicate the analysis presented here. Finally, a better understanding of the effect of PZT material on the plate response would allow better placement of the instrumentation.

BIBLIOGRAPHY

1. I. D. Abrahams. Scattering of sound by an elastic plate with flow. *Journal of Sound and Vibration*, 89:213–231, 1983.
2. J. D. Anderson. *Fundamentals of Aerodynamics*. McGraw-Hill Book Company, New York, N.Y., 1984.
3. R. L. Bisplinghoff and H. Ashley. *Principles of Aeroelasticity*. Dover Publications, Inc., New York, 1962.
4. R. D. Blevins. *Formulas for natural frequency and mode shape*. Robert E. Krieger Publishing Company, Inc., Malabar, FL, 1979.
5. W. J. Chyu and M. K. Au-Yang. Response of panels to turbulence-induced, surface-pressure fluctuations and resulting acoustic radiation to the flow field. In *Aero-Acoustics Conference*, number AIAA Paper 73–993, Seattle, Washington, October 1973. AIAA.
6. R. L. Clark *et al.* Characterization of multiple piezoelectric actuators for structural excitation. *Journal of the Acoustical Society of America*, 90:346–357, 1991.
7. D. G. Crighton. The 1988 Rayleigh Medal Lecture: Fluid loading - the interaction between sound and vibration. *Journal of Sound and Vibration*, 133(1):1–27, 1989.

8. E. H. Dowell. Transmission of noise from a turbulent boundary layer through a flexible plate into a closed cavity. *Journal of the Acoustical Society of America*, 46(1):238–252, 1969.
9. E. H. Dowell. *Aeroelasticity of Plates and Shells*. Noordhoff International Publishing, The Netherlands, 1975.
10. E. H. Dowell. On asymptotic approximations to beam model shapes. *Journal of Applied Mechanics*, 51:439, 1984.
11. R. Haberman. *Elementary Applied Partial Differential Equations*. Prentice-Hall, Inc., New Jersey, 1987.
12. IMSL, Inc., Houston, Texas. *MATH LIBRARY:FORTRAN Subroutines for Mathematical Applications— User's Manual*, 1.0 edition, 1987.
13. R. M. Jones. *Mechanics of Composite Materials*. Scripta Book Company, Washington, D.C., 1975.
14. G.A. Kriegsmann and M. A. Scandrett. Assessment of a new radiation damping model for structural acoustic interactions. *Journal of the Acoustical Society of America*, 86:788–794, 1989.
15. B. Laulagnet and J. L. Guyader. Modal analysis of a shell's acoustic radiation in light and heavy fluids. *Journal of Sound and Vibration*, 131:397–415, 1989.
16. R. A. Mangiarotty. Acoustic radiation damping of vibrating structures. *Journal of the Acoustical Society of America*, 35(3):369–377, 1963.
17. G. P. Mathur and B. K. Gardner. Interior noise prediction methodology: ATDAC theory and validation. Technical Report CR-187626, NASA, April 1992.

18. L. Meirovitch. *Elements of vibration analysis*. McGraw Hill, Inc., New York, NY, 1975.
19. J. S. Mixson and L. R. Koval. On the interaction of a vibrating plate with an acoustic medium. New York, New York, April 1974. Presented at 87th Meeting of Acoustical Society of America.
20. L. Muhlstein, Jr. Experimental evaluations of the aerodynamic damping of skin panels at low supersonic mach numbers. In *13th Structures, Structural Dynamics, and Materials Conference*, number AIAA Paper 72-402, San Antonio, Texas, April 1972. AIAA/ASME/SAE.
21. A. D. Nashif, *et al.* *Vibration Damping*. John Wiley and Sons, New York, 1985.
22. C. A. Powell, Jr. and D. G. Stephens. Vibrational characteristics of sandwich panels in a reduced-pressure environment. Technical Note D-3549, National Aeronautics and Space Administration, 1966.
23. B. E. Sandman. Numerical fluid loading coefficients for the modal velocities of a cylindrical shell. *Computers and Structures*, 6:467-473, 1976.
24. D. G. Stephens and M. A. Scavullo. Investigation of air damping of circular and rectangular plates, a cylinder and a sphere. Technical Note D-1865, National Aeronautics and Space Administration, 1965.
25. W. A. Strawderman and R. A. Christman. Turbulence induced plate vibrations: Some effects of fluid loading on finite and infinite plates. *Journal of the Acoustical Society of America*, 52:1537-1551, 1972.

26. W. J. Tuovila and R. W. Hess. Aerodynamic damping at mach numbers of 1.3 and 1.6 of a control surface on a two-dimensional wing by the free-oscillation method. Technical Note D-116, National Aeronautics and Space Administration, 1960.
27. C. S. Ventres and E. H. Dowell. Comparison of theory and experiment for nonlinear flutter of loaded plates. *AIAA Journal*, 8(11):2022–2030, 1970.
28. C. E. Wallace. The acoustic radiation damping of the modes of a rectangular panel. *Journal of the Acoustical Society of America*, 81:1787–1794, 1987.
29. J. H. Wilby. Technical Report AFFDL-TR-67–70, Air Force Flight Dynamics Laboratory, 1967.

Appendix A BEAM FUNCTION APPROXIMATION

The beam functions were approximated using the following analysis to simplify the integral evaluations in Eqs. (2.17) and (2.17s). For a clamped-clamped beam the exact expressions for the normalized beam function (for $0 < x < 1$) is given by

$$W_r(x) = \frac{\cos\beta_r - \cosh\beta_r}{\sinh\beta_r - \sin\beta_r} (\sinh\beta_r x - \sin\beta_r x) + \cosh\beta_r x - \cos\beta_r x. \quad (\text{A1})$$

As $r \rightarrow \infty$ then $\beta_r \rightarrow \frac{(2r+1)\pi}{2}$. Thus Eq. (A1) can be approximated by [10]

$$W_r(x) = \sin\beta_r x - \cos\beta_r x - (-1)^r e^{\beta_r(x-1)} + e^{-\beta_r x}. \quad (\text{A2})$$

For the clamped-clamped beam the approximation, is very close to the exact function, even for the first few modes, see Figure A1. The approximation eliminates the computation errors at the higher modes caused by inaccurate calculation of the hyperbolic functions.

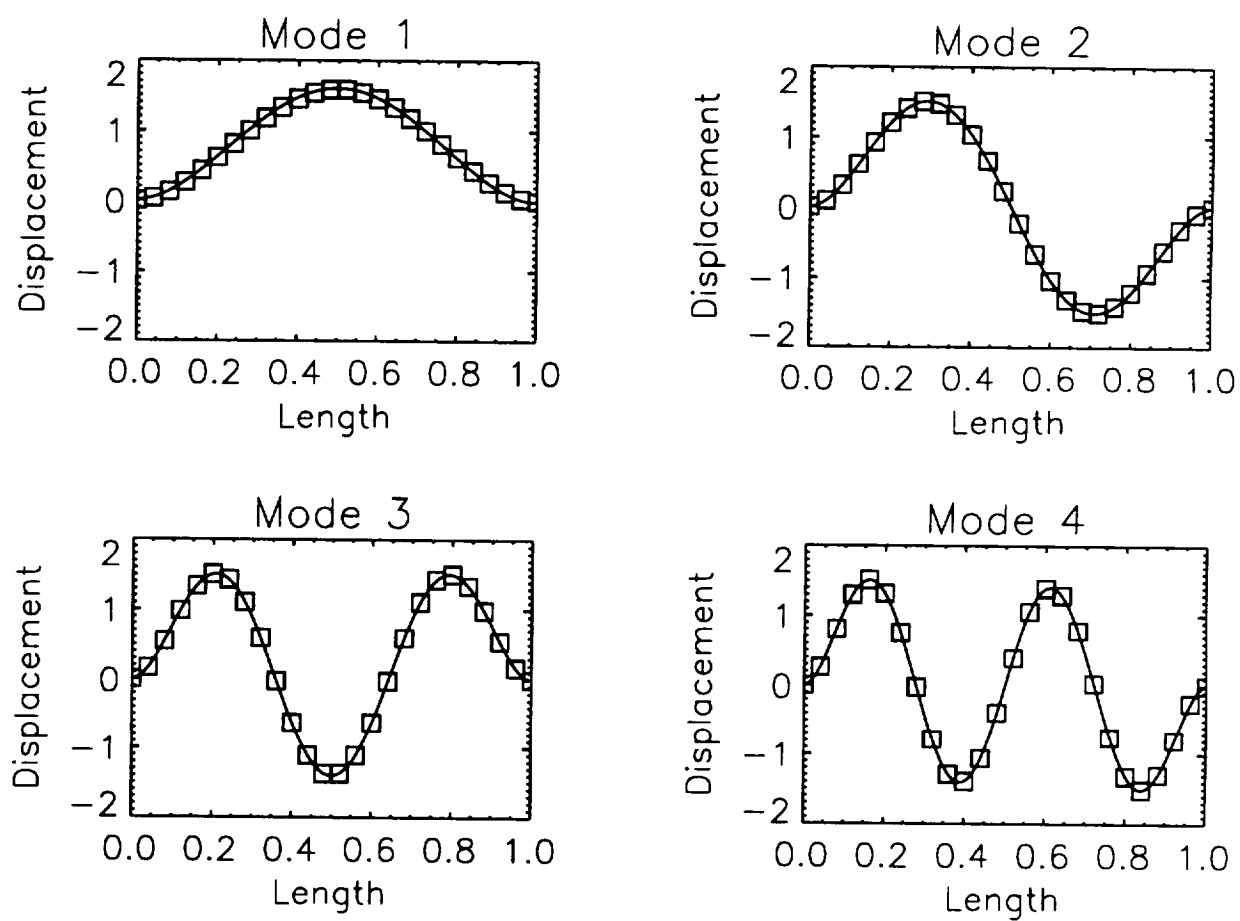


Figure A1. Comparison of exact (—) and approximate (\square) mode shapes

Appendix B EXPERIMENTAL DECAY PLOTS

The following figures contain the raw decay data which was presented in Table 4.2 and Figure 4.11.

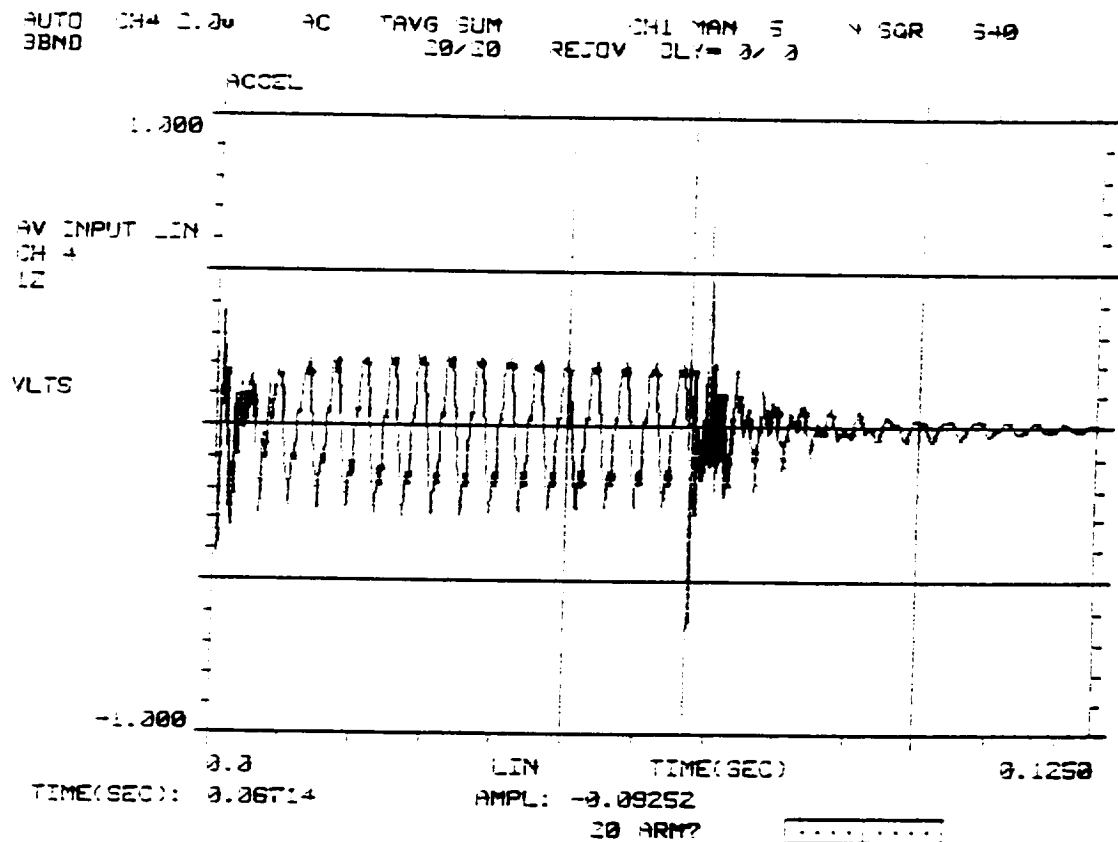


Figure B1. Accelerometer response for PZT excitation at the 1,1 mode.

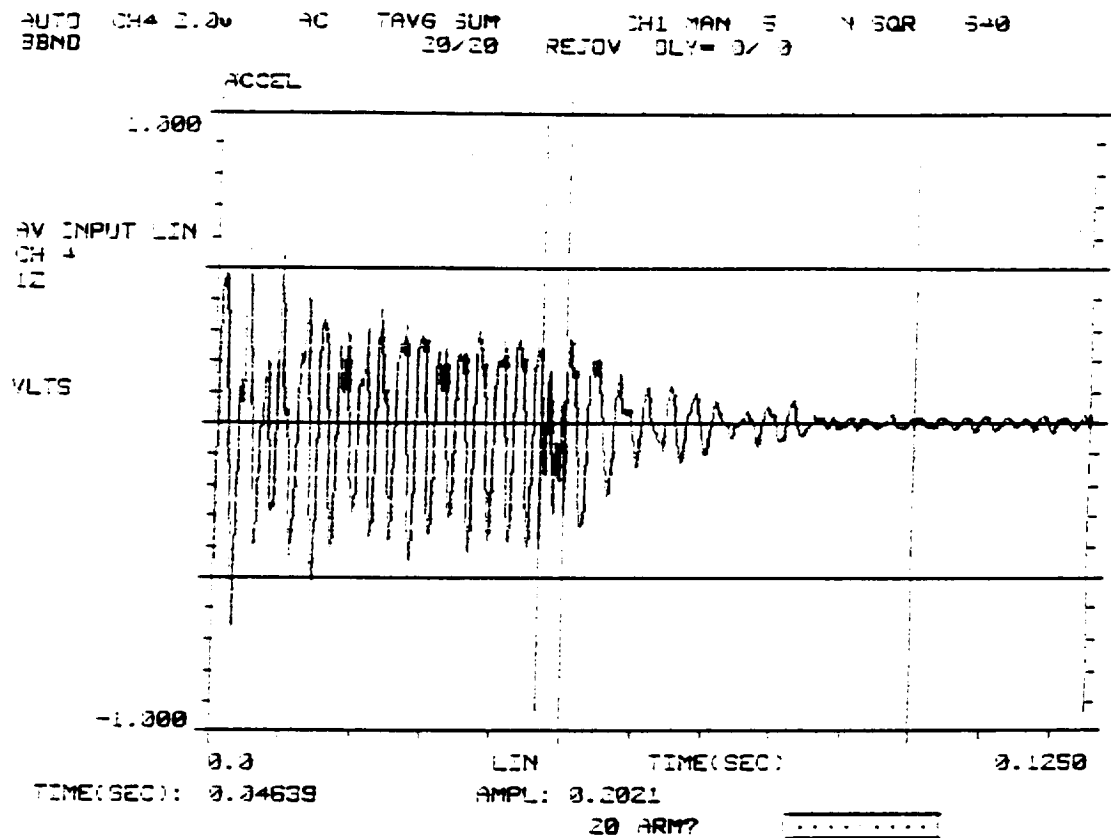


Figure B2. Accelerometer response for acoustic speaker excitation at the 1,2 mode.

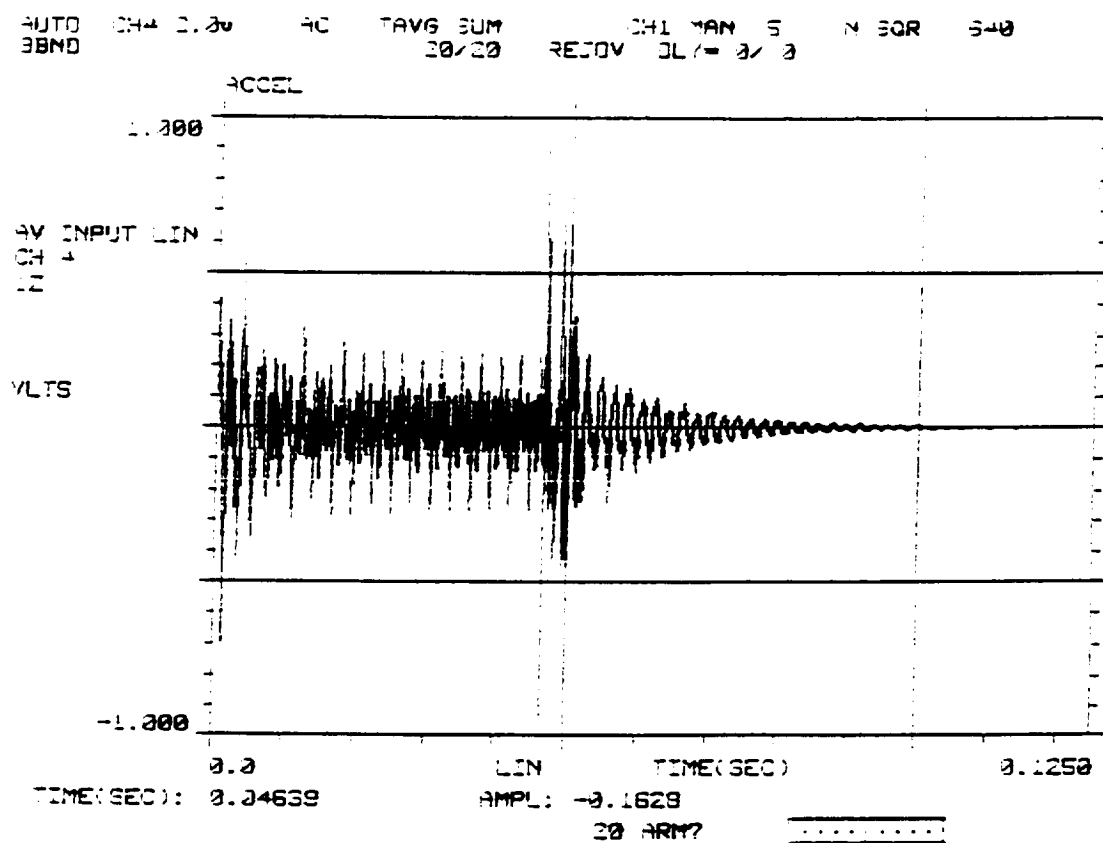


Figure B3. Accelerometer response for PZT excitation at the 1,2 mode.

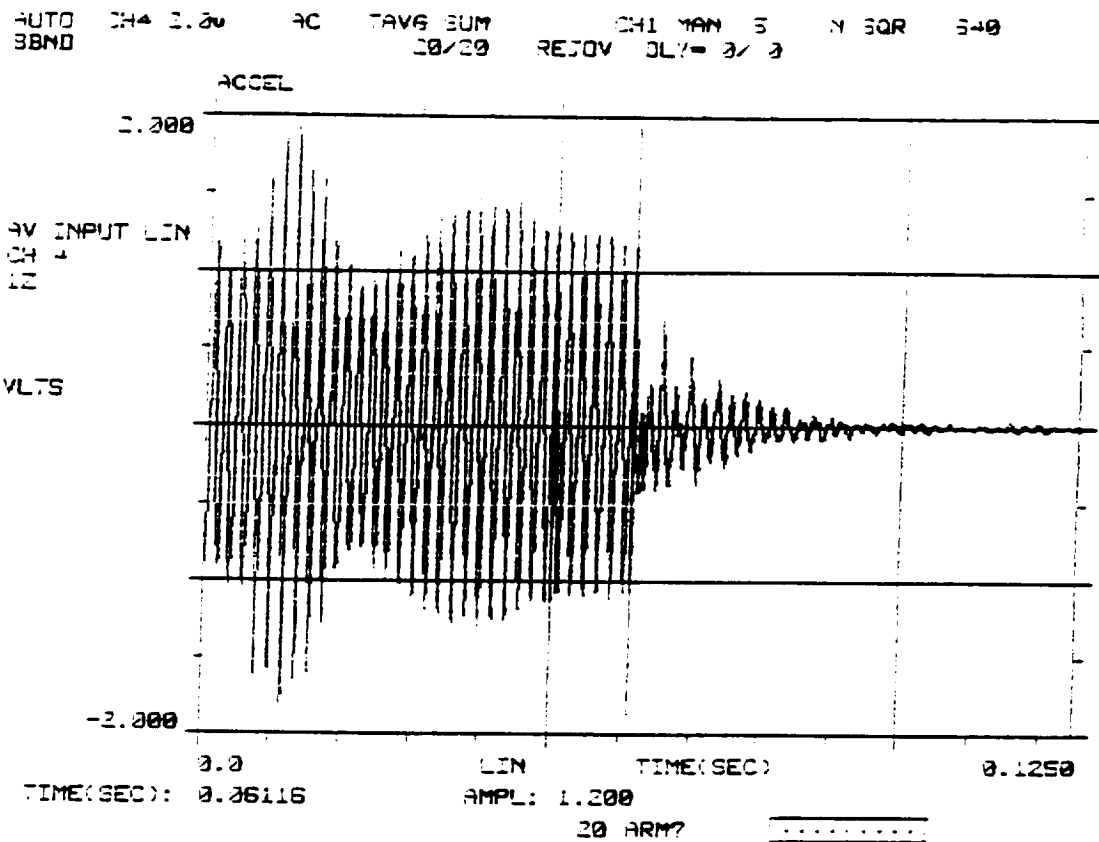


Figure B4. Accelerometer response for acoustic speaker excitation at the 1,3 mode.

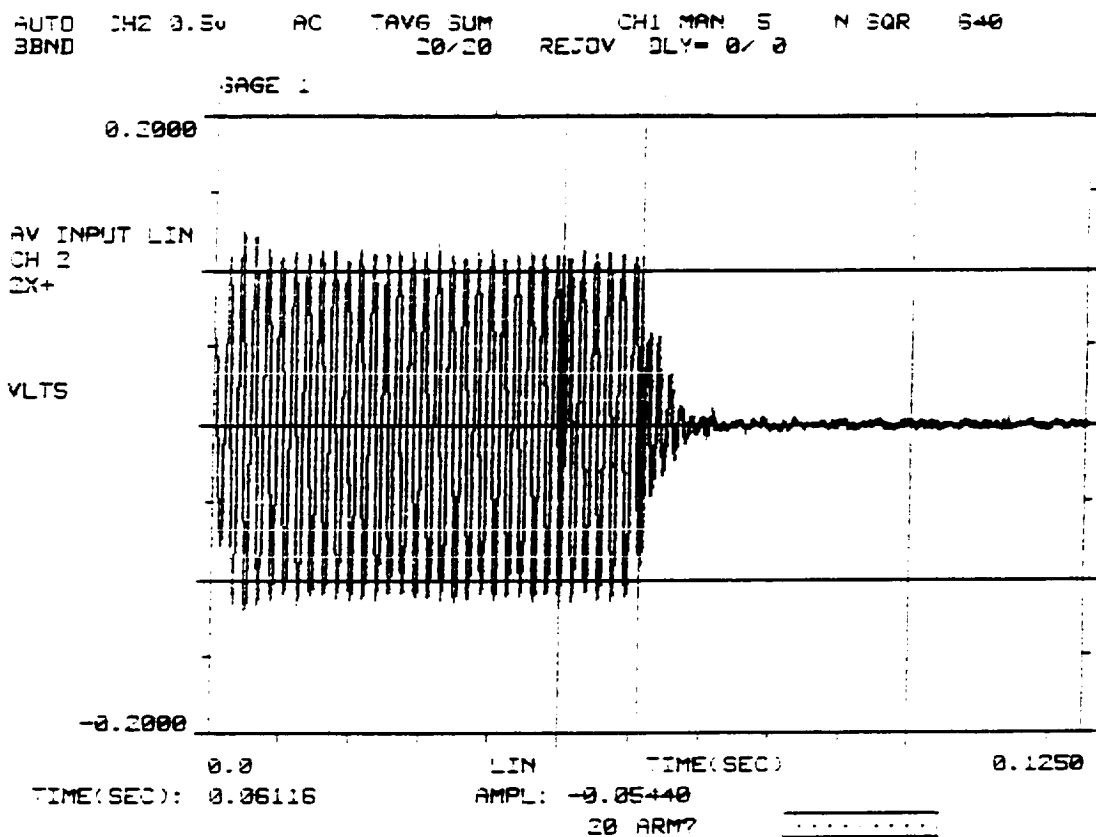


Figure B5. Strain gage response for PZT excitation at the 1,3 mode.

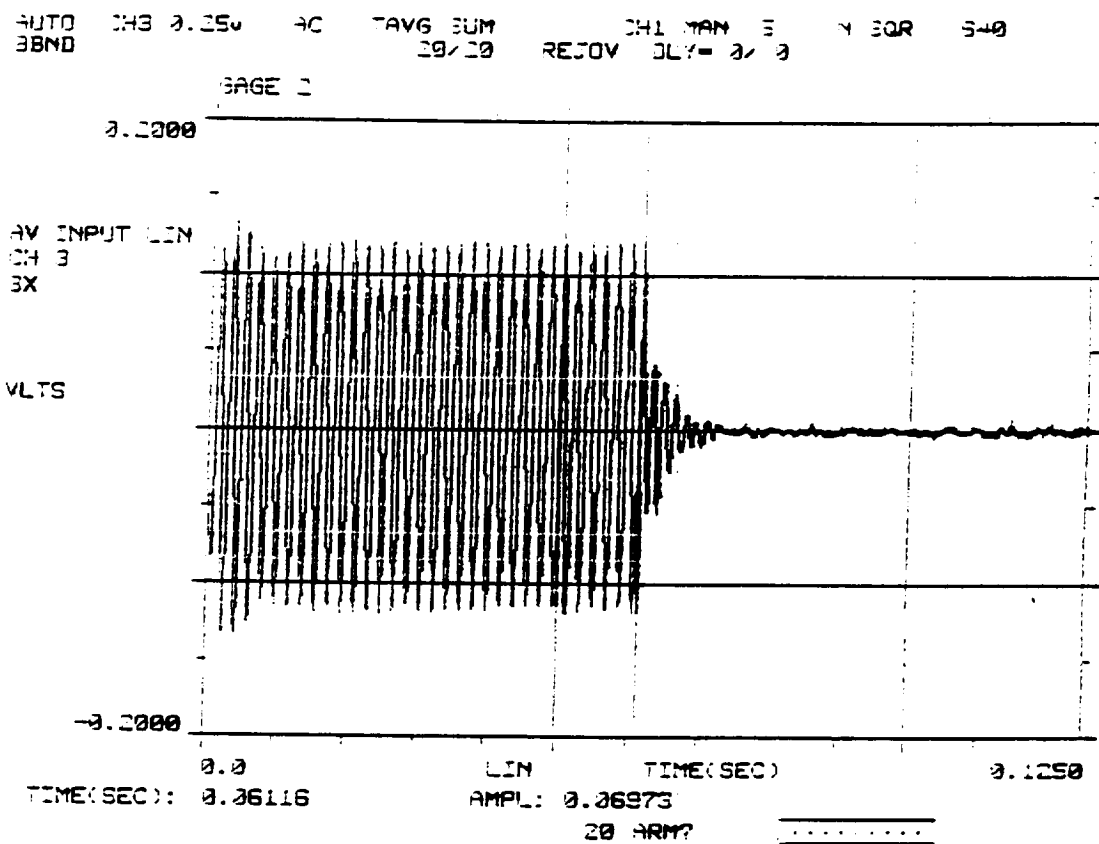


Figure B6. Strain gage response for PZT excitation at the 1,3 mode.

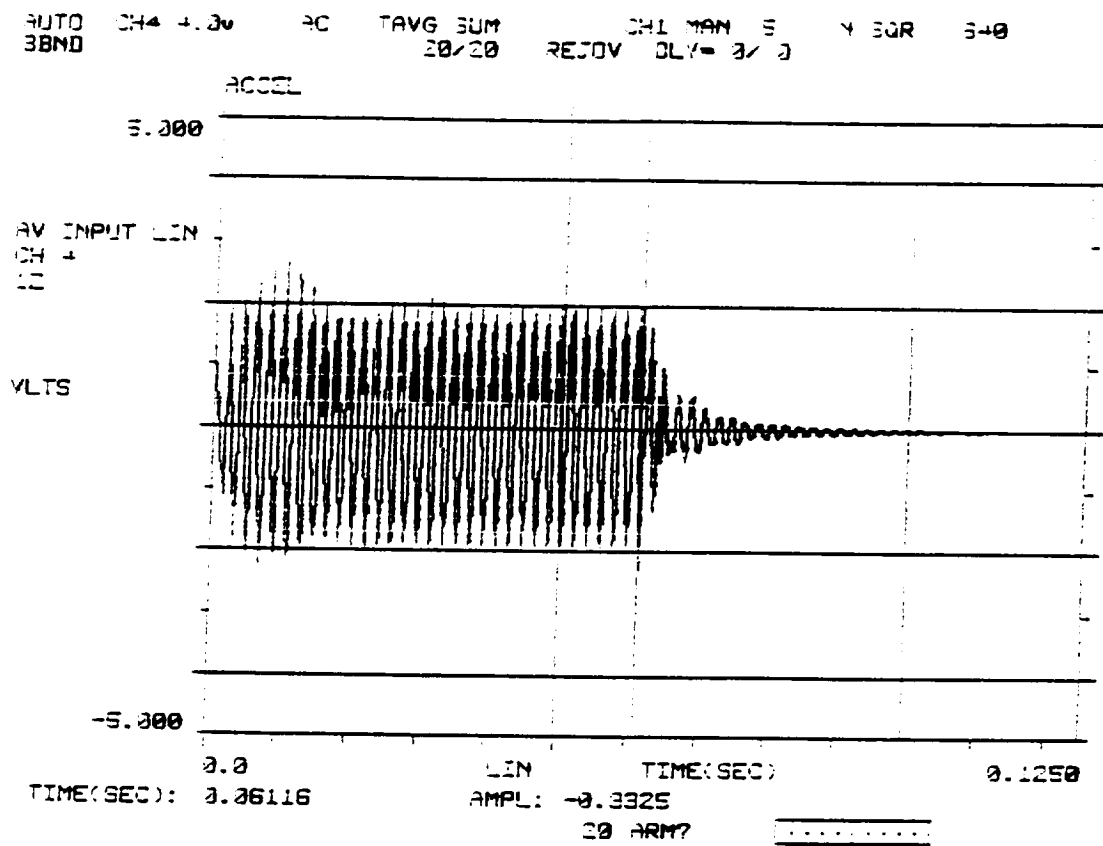


Figure B7. Accelerometer response for PZT excitation at the 1,3 mode.

Appendix C BIOGRAPHY

Karen Heitman Lyle was born March 12, 1959 in Indianapolis, Indiana. She received a Bachelor of Science in Mechanical Engineering degree (with distinction) in December 1981 from Purdue University and a Master of Science in Mechanical Engineering degree in December 1983 also from Purdue University. She authored or co-authored the following papers:

1. Heitman, K E. and Mixson, J. S.: Laboratory study of cabin acoustic treatments installed in an aircraft fuselage. *Journal of Aircraft*, Vol. 23 no. 1, January 1986, pp. 32–38.
2. Atwal, M. S., Heitman, K. E. and Crocker, M. J.: Light aircraft sound transmission studies: Noise reduction model. *Journal of the Acoustical Society of America*. Vol, 82 no. 4, October 1987, pp. 1342–1348.
3. Heitman, K. E. and Mixson, J. S.: Laboratory study of sidewall noise transmission and treatment for a light aircraft fuselage. *Journal of Aircraft*, Vol. 24 no. 9, September 1987, pp. 660–665.
4. Lyle, K. H. , Leatherwood, J. D. and Daniels, E. F.: Predicted and measured strain responses of isotropic panels to base excitation. NASA TM-4054/ AVSCOM TM-88-B-013, August 1988.
5. Lyle, K. H. , Atwal, M. S. and Crocker, M. J.: Light aircraft sound transmission studies: The use of the two-microphone sound intensity technique. *Noise Control Engineering Journal*, Vol. 31 no. 3, November 1988, pp. 145–153.

6. Lyle, K. H. and Dowell, E. H.: Acoustic radiation damping of flat rectangular plates subjected to subsonic flows. accepted by *Journal of Fluids and Structures*.
7. Lyle, K. H. and Dowell, E. H.: Acoustic radiation damping of rectangular composite plates subjected to subsonic flows. accepted by *Journal of Fluids and Structures*.